RICE UNIVERSITY

Nanoscale Electronic Transport Studies of Novel Strongly Correlated Materials

by

Will J. Hardy

A THESIS SUBMITTED
IN PARTIAL FULFILLMENT OF THE
REQUIREMENTS FOR THE DEGREE

Doctor of Philosophy

APPROVED, THESIS COMMITTEE:

Douglas Natelson, *Chair*
Professor of Physics and Astronomy,
Electrical and Computer Engineering, and
Materials Science and Nanoengineering

Rui-Rui Du
Professor of Physics and Astronomy

Sibani Lisa Biswal
Associate Professor of Chemical and
Biomolecular Engineering, and Materials
Science and Nanoengineering

HOUSTON, TEXAS
APRIL 11, 2017

ABSTRACT

Nanoscale Electronic Transport Studies
of Novel Strongly Correlated Materials

by

Will J. Hardy

Strongly correlated materials are those in which the electron-electron and electron-lattice interactions play pivotal roles in determining many aspects of observable physical behavior, including the electronic and magnetic properties. In this thesis, I describe electronic transport studies of novel strongly correlated materials at the nanoscale. After introducing basic concepts, briefly reviewing historical development of the field, and discussing the process of making measurements on small length scales, I detail experimental results from studies of four specific materials: two transition metal oxide systems, and two layered transition metal dichalcogenides with intercalated magnetic moments. The first system is a modified version of a classic strongly correlated material, **vanadium dioxide ($\mathbf{VO_2}$)**, which here is doped with hydrogen to suppress its metal-insulator transition and stabilize a poorly metallic phase down to liquid helium temperatures. Doped VO_2 nanowires, micron flakes, and thin films display magnetoresistance (MR) consistent with weak localization physics, along with mesoscopic resistance fluctuations over short distances, raising questions about how to model transport in bad-metal correlated systems. A second transition metal oxide system is considered next: **Quantum wells**

in $SrTiO_3$ sandwiched between layers of $SmTiO_3$, in which anomalous voltage fluctuation behavior is observed in etched nanostructures at low temperatures. After well-understood alternative origins are ruled out, an explanation is proposed involving a time-varying thermopower due to two-level fluctuations of etching-induced defects. Next, I shift to the topic of layered itinerant magnetic materials with intercalated moments, starting with **$Fe_{0.28}TaS_2$**, a hard ferromagnet (FM) with strong spin-orbit coupling. Here, a surprisingly large MR of nearly 70% is observed, an especially striking feature given that the closely related compounds at Fe intercalation fractions of 1/4 or 1/3 have MR nearly two orders of magnitude smaller. In the latter compounds, the Fe atoms are arranged in ordered superlattices, whereas for the 0.28 case, a portion of the Fe moments deviate from ordered arrangement and are relatively easily flipped by an external magnetic field to become anti-aligned with neighboring ordered Fe moments. This situation, combined with strong spin-orbit coupling, results in enhanced charge carrier scattering and greatly increased resistance. The thesis concludes with a study of a second layered magnetic material, **V_5S_8** (structurally equivalent to $V_{0.25}VS_2$), which is found to have a magnetic field driven phase transition at low temperatures, believed to be from antiferromagnetic ordering to a paramagnetic phase. This transition is first order in thick crystals, but becomes second order as the crystal thickness decreases toward 10 nm. Together, the experiments described in this thesis highlight the complexity and diversity of strongly correlated materials, while showcasing the power of nanoscale electronic transport in delivering an improved understanding of these systems.

ACKNOWLEDGEMENTS

I couldn't ask for a better advisor than Doug Natelson. In both the classroom and the lab, Doug uses nanoscience as a platform to engage and educate the next generation of scientists in condensed matter physics. He is always at the ready to patiently explain a physical concept, offer advice on setting up a measurement, go over freshly acquired data, or revise written work. His exemplary guidance has prepared me for my next scientific adventure.

Many thanks to the other members of my thesis committee, Prof. Rui-Rui Du and Prof. Sibani Lisa Biswal, for their support of my graduate study and for taking time to evaluate my thesis.

I am grateful to all the members of the Natelson research group, past and present, for their good company and shared learning and teaching. In particular, I am indebted to Heng Ji and Jiang Wei for the training and guidance they offered me when I joined the lab – they taught me a great deal about the hands-on aspects of nanofabrication and transport measurements. Pavlo Zolotavin was always up for a team effort to fix the e-beam evaporator, or for a stimulating discussion about science or current events over a cup of coffee. Panpan Zhou has been a quick learner in preparing to take over our corner of the lab, and I know the PPMS will be in good hands under his watch.

I couldn't have done any of this work without constant support and excellent material samples from collaborators at Rice and beyond. Thanks

to Dr. Chih-Wei Chen, Dr. Andrea Marcinkova, Binod Rai, and Justin Chen, along with their advisor, Prof. Emilia Morosan, of Rice University; Jiangtan Yuan and his advisor, Prof. Jun Lou, of Rice University; Dr. Nam Dong Kim; Dr. Evgeny Mikheev, Brandon Isaac, and Patrick Marshall, and their advisor, Prof. Susanne Stemmer, at UC Santa Barbara.

My graduate career has been much enriched by an ever-changing lunch group spanning several years and disciplines. Even though we may not work on the same research topics, there's always something in common to talk about on the Brockman patio. To name just a few: Eteri, Chloe, Jesse, Chih-Wei, Jacob, Miriam, Charlotte, Jim, Binod, Vaideesh, Melissa, Jana, and others – thanks for the frequent reminders that grad school is about more than just research.

Finally, I am grateful for the support of my family. Mom and Dad – it wouldn't have happened without the foundations you laid. Last and *most* of all, Natalie – thank you for ignoring the warnings about marrying a physics grad student and helping me push through to the finish line. Here's to the next chapter!

Contents

List of Figures

Chapter 1

Introductory Concepts and Motivation

A good puzzle is the perfect match for innate human curiosity. Nature's puzzles, the most nuanced and complex ones available, inspire scientists to seek explanations consistent with empirical observations. In condensed matter physics, the intriguing and often mysterious 'strongly correlated materials' have provided robust challenges to theorists and experimentalists alike, spurring investigations over the better part of a century. In such materials, the electron-electron and electron-lattice interactions ('correlations') play a large or even dominant role in determining overall properties. Strong correlations often lead to a fragile balance among competing ground states of spin, charge, and orbital order, giving rise to such phenomena as metal-insulator transitions, competing magnetic orderings, and superconductivity. The low energy electronic excitations of such materials are not necessarily well described as nearly free electron-like quasiparticles, which makes accurate predictions of behavior especially difficult.

As P.W. Anderson succinctly summarized, "More is different." [20] That is, a complex system can display phenomena that are not well understood in terms of just a collection of the system's individual components, a concept upon which R. Laughlin further elaborates in his excellent book *A Different Universe.* [21] In the study of strongly correlated materials, the central question is: How do electronic correlations affect the properties of solid state materials? Because this is such a broad question, here we have selected for study just a few specific examples of SCMs, which exemplify some of the great variety of correlation-induced effects in solids.

1.1 Goals of this Work

Recently, it has become clear that examining strongly correlated systems on small length scales can be very revealing. To that end, this thesis focuses on applying the experimental technique of nano/mesoscale electronic transport measurements to four systems, each belonging to one of the following classifications: (1) strongly correlated transition metal oxide systems or (2) two-dimensional layered transition metal dichalcogenide materials with intercalated magnetic moments. The phase diagrams of these systems reveal competitions between various physical orders, spanning the range of antiferromagnetic insulators, non-Fermi liquid metals, bad metals, conventional metals, and itinerant ferromagnets and antiferromagnets. Such competitions are alluring from a basic physics perspective as well as from a technological standpoint, with the hope that gaining an understanding of the underlying science of various phase transitions will allow engineers to harness them for practical devices such as memories, sensors, actuators, and energy-harvesting systems. In this chapter, we will briefly review the history of strongly correlated materials as they fit into the overall development of condensed matter physics, introduce the materials studied in this thesis, and lead into the discussion of electronic transport experimental techniques covered in Chapter 2.

1.1.1 Strongly correlated transition metal oxides

Transition metal oxides have featured centrally in the storyline of strongly correlated materials since the field's early days, displaying exciting phenomena from metal-insulator transitions to high-T_C superconductivity. Here we expand on two oxide-focused topics.

Chapter 3 covers the implementation of a new strategy to control and study the bad-metal phase of vanadium dioxide at low temperatures. The 'bad-metal' phase contrasts with conventional good metals, where $k_F\ell >> 1$ (k_F is the Fermi wavelength and ℓ is the carrier mean free path) describes a situation in which charge carriers can propagate many wavelengths before losing their phase coherence through inelastic scattering. In bad metals, an anomalously large resistivity can correspond to the case where $k_F\ell < 1$, a situation approximately equivalent to resistivity exceeding the Mott-Ioffe-Regel limit [22, 23], where quasiparticles may not be well defined, and quantum corrections to transport have not been well explored. Doping VO_2 with atomic hydrogen suppresses the metal-insulator transition and stabilizes a relatively conducting (though poorly metallic) phase down to cryogenic temperatures, making it possible to conduct low-temperature transport studies of a material very similar to the pristine compound's high-T bad metal phase. Using magnetoresistance measurements of epitaxial thin films, nanowires, and micron-scale flake-like crystals, we find evidence of both localization effects and, on short length scales, conductance fluctuations. This raises important questions about how to understand quantum interference effects in bad metal systems.

In Chapter 4, we report on unexpected potential fluctuation behavior found at low temperatures in etched nanostructures of the quantum well formed in a thin layer of $SrTiO_3$ sandwiched between $SmTiO_3$ layers. Using etched micron-scale mesas of epitaxially-grown quantum well material, we measure the resistance of the mesa along the direction of current flow using large current leads and narrow ($\sim$ 250 nm) voltage probe electrodes. Although the current is very stable, the potential as measured with these electrodes begins fluctuating significantly as we cool below $\sim$ 20 K, well in excess of the high-temperature noise level, and the amplitude of fluctuations *ramps up* as the temperature decreases. Strikingly, the potential fluctuations persist even when the current is turned off. The phenomenon is visible as a function of temperature, time, or magnetic field, and is not observed in contacts with lateral dimensions of several microns or larger. We attribute this behavior to a fluctuating local Seebeck coefficient, with etching-induced defects serving as two-level fluctuators, the effects of which are averaged out over length scales longer than a few hundred nm. This could have significant implications as interest grows in oxide heterostructure device design.

1.1.2 Layered materials with intercalated magnetic moments

Magnetic materials have found widespread interest and applications for centuries. Traditionally, naturally occurring magnetic materials such as lodestone (also called magnetite, Fe_3O_4) were employed for purposes such as training compass needles to point north, followed by progress in simple magnets (Fe, Co, Ni, alloys such as CoFeB and Al-Ni-Co, and ceramic compounds such as the ferrites). Recently, much stronger permanent magnets have become available, particularly the rare earth compounds such as $SmCo_5$ and $Nd_2Fe_{14}B$, replacing the traditional materials in many applications. Immense resources have been expended to commercialize magnetic films and multilayers for information storage applications, from magnetic tape to hard disk drives (the storage media in various formats, as well as the read-heads which make use of giant magnetoresistance, GMR). Despite recent advances in flash memory technology, magnetic storage devices still have important cost and performance benefits, and are pervasive in modern computing infrastructure. Furthermore, new implementations of electronically-controlled magnetic memories, such as spin-transfer-torque magnetic random access memory (STT-MRAM) promise long-lasting, fast, non-volatile replacements for flash memory that do not require strong magnets to read or write information (see, *e.g.*, Ref. [24]). These new technologies do still require nanoscale magnets to serve as the storage components.

Magnetic materials with layered crystal structure constitute an emerging focus topic in condensed matter science, with intrinsic 2d geometries that could endow unique characteristics and potentially be extremely useful. Layered materials in general have captured the imagination of many researchers, starting with the discovery of graphene, a single atomic layer of carbon atoms arranged in a hexagonal lattice with a host of exotic electronic properties (such as linear band dispersion and relativistic massless Dirac fermions). An entirely new field was born, with the focus on graphene expanding to a resurgence of interest in the transition metal dichalcogenides (which are typically semiconductors or metals, and can be prepared as one unit cell thick sheets), as well as hexagonal boron nitride, a graphene analog and excellent 2d insulator. These 2d layers can be stacked into heterostructures, enabling, *e.g.*, extremely thin $p-n$ junctions with gate-tunable graphene contacts. In the quest for integrated planar devices of 2d materials, magnetic materials would be essential for many next-generation information storage goals featuring magnetoresistive bits (as in MRAM). Yet, relatively little progress has been made on this topic so far due to lack of 2d crystalline magnetic materials. Here we study both the layered ferromagnet $Fe_{0.28}TaS_2$ (Chapter 5) and the layered antiferromagnet V_5S_8 (Chapter 6). These materials are magnetic by way of intercalation, a procedure in which magnetic moments are inserted between the 2d layers of TMD materials during synthesis. An example of the crystal structure of such a material, $Fe_{0.25}TaS_2$, is shown in Fig. 1.1. This route to layered magnetic materials appears quite promising, and there is much room for scientific progress in the area.

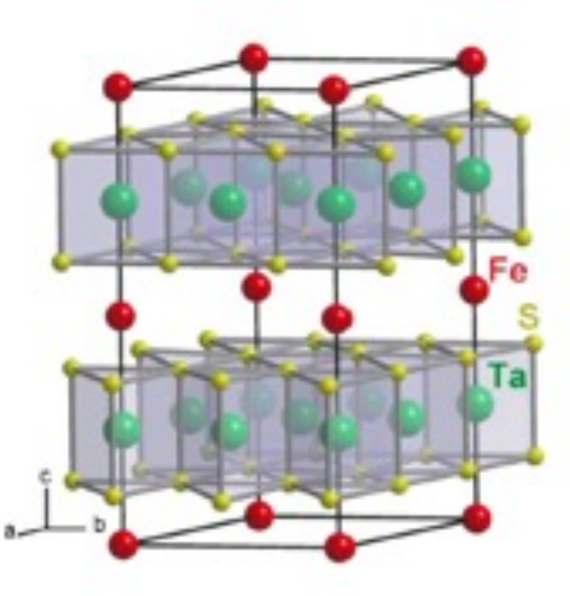

Figure 1.1: **Crystal structure of the layered ferromagnet $\mathbf{Fe_{0.25}TaS_2}$.** Fe atoms, red, are intercalated in a superlattice arrangement between planes of TaS_2 (Ta = green, S = yellow). Figure reproduced with permission from [1]. © 2007 American Physical Society.

1.2 The Basics of Strongly Correlated Materials

Now that the main topics of this thesis have been introduced, let's step back and consider the features that set strongly correlated materials apart from others. We learn in elementary electricity and magnetism theory that opposite charges attract and like charges repel each other, so we might expect that in solids, the extraordinarily large number of electrons packed close together would feel both strong attraction to the positive nuclei and strong mutual repulsion from each other, and thus position themselves as far apart – spatially and energetically – as possible. Both Pauli's exclusion principle and Hund's rules for orbital filling reflect this expectation (though for reasons beyond classical electrostatic repulsion of point particles). From this picture, we might imagine that there are only electrical insulators, but of course we also have metals, semiconductors, and semimetals, as well as magnetic materials with long-range order of electronic spins (*e.g.*, ferromagnets, antiferromagnets). It is clear that the electronic properties of solids are vastly more complex than those of isolated charged particles or neutral atoms. How should we go about mathematically describing the electronic properties of condensed matter?

Suppose we want to calculate the electronic structure of a solid exactly: To be quantum mechanically correct, we then need to write the (time-independent, non-relativistic) three-dimensional N-electron Schrödinger equation (SE), accounting for the interactions between all N of the valence electrons as well as the lattice potential, or equivalently, one equation per electron (which must take into account all the others). Taking Au as an example, with its density of 19.3 g/cc, atomic mass ≈ 197 g/mol, and one conduction electron per atom, the number of conduction electrons in a cubic centimeter would be $N \approx 5.9 \times 10^{22}$, requiring a stupendously large number of equations, well beyond our computational capacity. The situation is not hopeless, however: A viable path forward lies in the fact that we *do* know how to solve the one-electron SE, and we can make some simplifying approximations to try solving the multi-electron problem.

The question of how best to model conduction in a solid has found many answers, ranging from the very simple (and not always very accurate) to the quite sophisticated.[25] Early efforts began with the Drude model, which views metallic conductivity via a classical gas of electrons, with a characteristic mean scattering time τ, so that the conductivity is given by $\sigma = ne^2\tau/m$, where n is the carrier density, e the electron charge, and m the carrier mass. Sommerfeld improved on Drude's picture by adding in the quantum-mechanically correct Fermi-Dirac distribution for electron energies– this gave results that were not too bad for metals. The nearly free electron model made use of the (then) newly discovered SE as well as Bloch's formalism, which treats electronic states as Bloch waves moving in the periodic potential of a lattice, yielding simple band structure. The tight-binding model takes the opposite approach to the nearly-free electron picture, starting with just isolated atomic orbitals, and adding in conduction by the overlap of orbitals of neighboring atoms (as in linear combinations of atomic orbitals, LCAO). The Hartree-Fock method, a mean-field technique, uses LCAO to obtain the one-electron wavefunction, and also takes exchange into account, so that the wavefunction reflects the necessary sign change upon switching two opposite-spin particles. In the techniques mentioned so far, the treatment of electron-electron correlations has been mediocre at most, yet these electronic structure calculations are sufficient to model many materials of scientific and technological interest, including typical nonmagnetic metals, semiconductors, and insulators. Specifically, the questions of why metals conduct electricity well, and why (band) insulators do not, can be answered.

Pictorially, in a band structure diagram of energy E as a function of wavevector k, if the valence and conduction bands directly overlap at the Fermi level, the material is a metal; if there is no such overlap, it's a semiconductor (if the distance between bands, the 'bandgap,' is fairly small) or an insulator (if it's instead rather large, typically more than a few eV); and if the bands overlap indirectly, with an offset in k-space, it's termed a semimetal. Fig. 1.2 shows band structure diagrams for two common semiconductors, Si and GaAs, demonstrating an indirect and direct band gap, respectively. In this approximation, a simple exercise of counting electrons per unit cell can be performed to predict metallic or insulating behavior, giving correct results in many cases. Note that here, only partially filled bands participate in conduction – completely filled bands are 'inert' in this aspect.

Sometimes, however, this simple picture breaks down, as Mott pointed out for the case of NiO,[26] for which band theory predicted a metal, while the real material is an

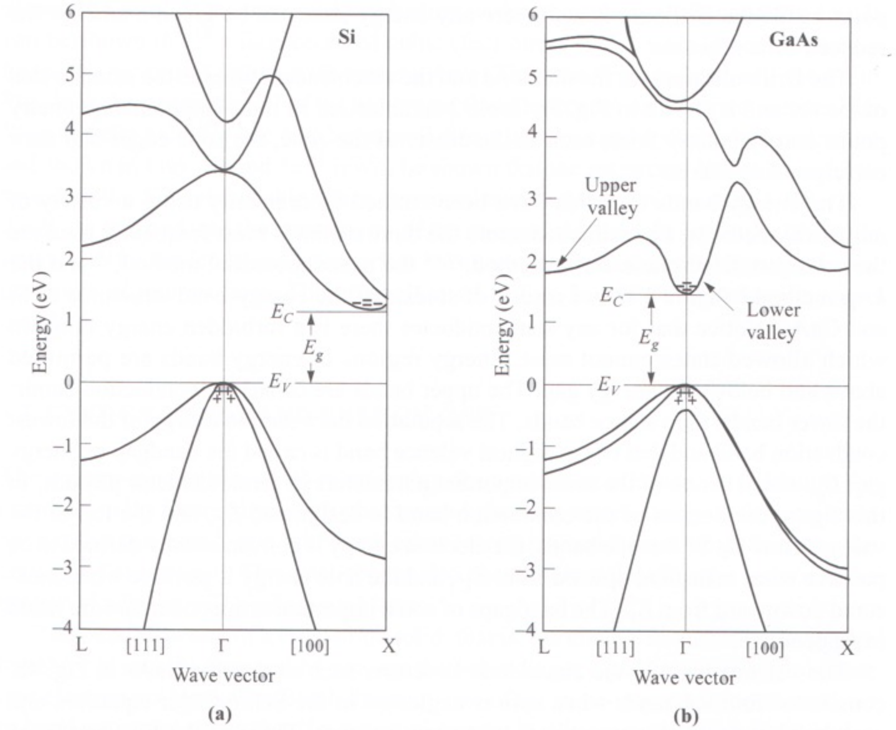

Figure 1.2: **Band structure diagrams of (a) Si and (b) GaAs.** E_V represents the valence band maximum in energy; E_C represents the conduction band minimum in energy; E_g is the bandgap (closest vertical distance between valence and conduction bands). Si is an indirect bandgap material (the valence band maximum and conduction band minimum are offset in k-space), while GaAs is direct-gap. The + signs represent holes in the valence band, and - signs represent electrons in the conduction band. Figure reproduced with permission from [2]. © 2006 John Wiley and Sons, Inc.

insulator. (Simply put, the size of the unit cell taken into account should have been doubled to reflect the antiferromagnetic ordering, which would make the uppermost band completely filled, rather than half filled. However, the calculations do not predict NiO's AFM state.) Such failures are the result of the (relative) importance of $e-e$ and electron-phonon *correlations* compared with the electrons' kinetic energy (particularly for valence electrons in partially filled $3d$ orbitals of transition metals), and materials for which these interactions are significant are thus called *strongly correlated materials.* These correlations give rise to competitions between ground states and the resulting macroscopic behaviors, resulting in phenomena such as colossal magnetoresistance

(CMR) [27], which is observed at the boundary of paramagnetism and ferromagnetism in $LaMnO_3$ substituted with Sr or Ca; and metal-insulator transitions, such as are found in vanadium dioxide (VO_2) [28, 29, 30], Fe_3O_4,[31, 32] and most rare earth nickelates $RNiO_3$ (R = rare earth) [33]. As an example, VO_2's competing orders are demonstrated in its phase diagram (Fig. 1.3), which we will discuss in further detail in Chapter 3. Interest in such phase transitions is both fundamental and technological, as anytime a material can be tuned between two very distinct states, it may be useful in such applications as switches or sensors. As the competitions in correlated materials can be tuned by myriad external parameters, such as temperature, pressure, strain, magnetic and electric fields, and chemical doping, there is hope that these materials could find a great many uses beyond the laboratory.

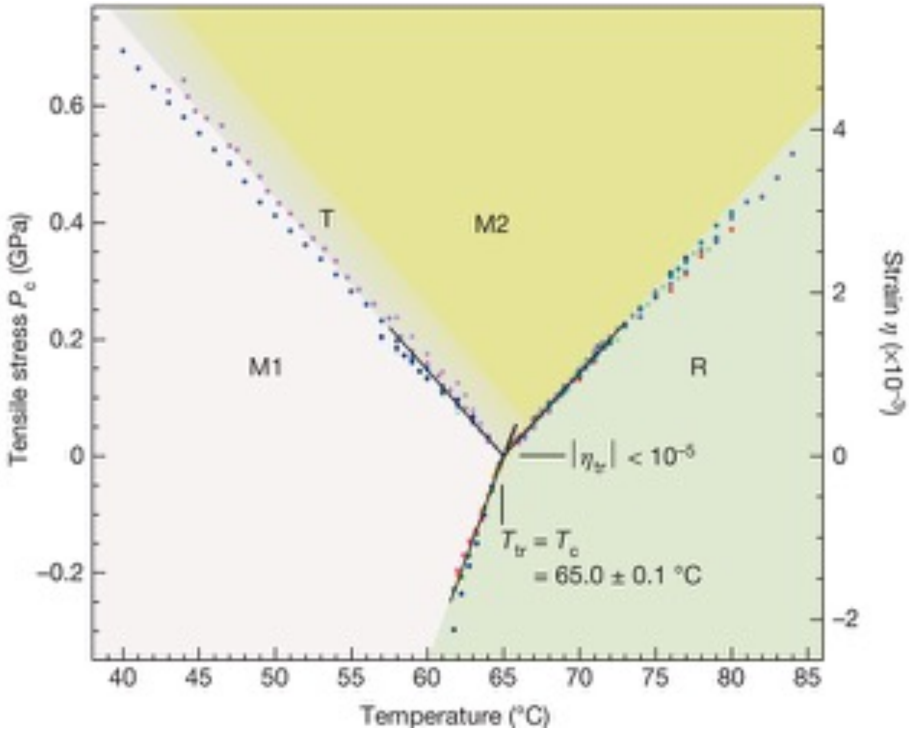

Figure 1.3: **Phase diagram of vanadium dioxide** The tensile stress–strain–temperature phase diagram of VO_2, showing a "solid-state triple point" at 65.0°C. A high temperature metallic rutile phase (R) competes with three insulating phases, two of which have monoclinic crystal structure (M1 and M2) while another is tetragonal (T). Figure reproduced with permission from [3]. © 2013 Macmillan Publishers Ltd.

The 1960s saw the introduction of the Hubbard model [34] as a simple way of taking on-site Coulomb repulsion into account, and it was applied to materials like NiO and VO_2, capturing more of their real features than any previous model (though still not quite perfect). Just two terms are needed to construct the Hamiltonian: a hopping term parameterized by t to describe kinetic energy, and an interaction term parameterized by U to describe on-site repulsion. This allows interactions to be slowly 'turned up,' and in the limit of large U/t, the model correctly predicts a Mott insulator via splitting of the conduction band into upper and lower Hubbard bands, with the Fermi level in between.

1.3 Recent Challenges

In the last 30 years or so, the problems that had been considered 'solved' in condensed matter physics have seen new challenges arise, setting the stage for important developments in correlated materials. As an example of one such upset, we take the BCS theory of superconductivity [35], a tour de force that earned the 1972 Nobel Prize in Physics for Bardeen, Cooper, and Schrieffer. They successfully explained the principles of type-I superconductivity, describing how pairs of electrons of opposite spin,mediated by phonons, team up to form bosonic quasiparticles called 'Cooper pairs' that condense into a superconducting ground state. However, BCS theory failed to adequately describe an exciting new class of superconductors, the high-T_C cuprate compounds announced in the late 1980s, and also the so-called 'heavy-fermion' superconductors that followed, with charge carriers that behave as if they had 1000× or more the mass of a bare electron. These two types of systems brought correlated materials again to the forefront of condensed matter physics. [36]

In 1986, at a time when experts expected a maximum achievable superconducting transition temperature of ~ 30 K, the announcement of the first high-T_C cuprate,

$La_{2-x}Ba_xCuO_4$,[37] stunned the world with superconductivity at around 30 K. This was quickly followed by additional cuprate examples with ever-increasing T_C values, surpassing the boiling point of liquid nitrogen, all the way up to 165 K in a mercury-based copper oxide under pressure. [36] It was an astounding revelation that the materials with highest transition temperatures were rooted in parent antiferromagnetic insulator compounds, and even when optimally doped for superconductivity, they still had bad-metal (high resistivity) or strange metal (not in agreement with Fermi liquid theory) high-temperature properties. As more became understood about the unconventional superconducting state in these materials (*e.g.*, d-wave pairing symmetry, vortices), people realized that it was also necessary to really grasp the normal state, including the effects of strong correlations, dimensionality (the key role of the CuO_2 planes), and bad metallicity. As shown in Fig. 1.4, the cuprates have quite complicated phase diagrams, beyond just superconductor vs. normal metal.

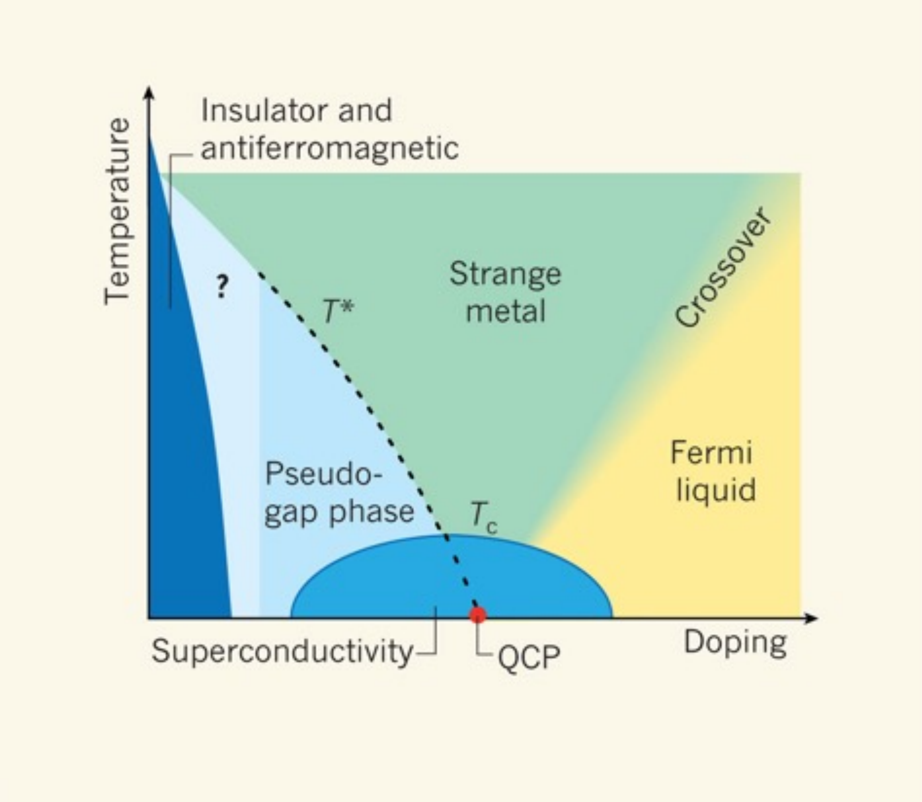

Figure 1.4: **Generic temperature–doping phase diagram of copper oxide superconductors.** Details vary for different specific materials, but the overall scheme is fairly consistent. Figure reproduced with permission from [4]. © 2010 Macmillan Publishers Ltd.

On the computational side, significant progress has been made to develop methods that work for correlated materials. Computational techniques of the mean-field variety for finding ground-state solutions have evolved from the Thomas-Fermi method of the 1920s[38, 39] and Hartree-Fock, to the now widely used and successful density functional theory (DFT). This method simplifies the problem of N interacting electrons by mapping it onto N problems of non-interacting electrons. The main principle is that there exists an energy-minimizing functional of the electron density $F[n(r)]$ which contains *all* the information about the potential $v(r)$, and in turn, the ground state many-body wavefunction.[40] The functional is not known exactly (particularly, its exchange-correlation portion) but can be approximated. The success of this approach in calculating properties of molecules and solids has been so vast as to merit the 1998 Nobel Prize in Chemistry for W. Kohn and J.A. Pople. Implementation of DFT uses the method of Kohn and Sham,[41] coupled with various approximations (such as the local density approximation, LDA, or the generalized gradient approximation, GGA). The simplest implementation specifically for strongly correlated materials, DFT+U, utilizes the Hubbard U to capture the correlation behavior, and is the starting point for many calculations. Additional accuracy comes at the cost of more computational intensity, as in the methods of DFT+VCA (virtual crystal approximation) or DMFT (dynamical mean field theory). After specifying the lattice, the calculation can be iterated to find the proper value of U that best replicates experimental results for magnetic moment values, band gaps, and ferro- or antiferromagnetic ordering. The relative contributions of individual orbitals can also be calculated.[42] It is also possible to take dynamic response into account through DMFT [43, 44, 45]), which has yielded many excellent advantages in handling strong correlations, though the system size that can be calculated is still small ($\sim$100 atoms).[42]

The latest advances in theoretical and computational approaches are best applied in concert with experiments, forming a feedback loop that allows computations to take advantage of realistic physical parameters, which in turn helps experimentalists design more efficient studies and explain new results. The wide array of available techniques in experimental condensed matter physics includes electronic transport (the primary method of choice for this thesis); thermal transport; optical spectroscopies; scattering experiments with X-rays, electrons, and neutrons; magnetometry; photoemission; and imaging (*e.g.*, optical, electron, ion, and scan probe). New tools can push the limits of traditional techniques: Bright synchrotron-based light sources, intense magnetic fields, and ultrafast lasers have all facilitated discoveries through access to new extremes. Similarly, progressively smaller length scales have become experimentally accessible and have proven invaluable in tackling open questions. In the next chapter, we will cover the experimental details of nano- and micro-scale electronic transport investigations of SCMs.

To sum up: Modern tools and approaches have changed how we study correlated electron phenomena, but despite steady progress, the underlying mysteries remain as vivid and alluring as ever, with much remaining yet to be discovered. Motivations to continue work in this field stem both from a perspective of fundamental scientific interest, as well as from the hope that these new, distinct materials and states of matter could be technologically valuable if well understood and controlled.

Chapter 2

Experimental Methods for Nanoscale Transport

Let's now consider how the power and simplicity of electronic transport measurements are implemented to study strongly correlated materials on small length scales. There are two essential ingredients of our experimental technique: ***nano*** and ***transport***.

Nano. Richard Feynman's famous 1959 speech, "There's Plenty of Room at the Bottom," [46] called for development of advanced techniques to encode information in small structures, in particular using the resolution of electron microscopy to perform nanoscale 'writing.' Indeed, Feynman presaged the widespread use of electron beam lithography as a route to fabrication of nanoscale samples, a technique that features prominently in this thesis. The general idea of making things small has matured into the broad field of "nanoscience," which now encompasses a great variety of work shared among the traditional fields of physics, materials science, chemistry, biology, and engineering. A generally accepted rough definition for something to be called "nanoscale" is for at least one dimension to measure $\sim$ 1–100 nm. Objects of this size ("nanostructures") can now be deterministically made using a variety of techniques (many variations of light- and particle-based lithographies, scanned probe techniques, templating, and bottom-up chemical synthesis, to name a few), incorporating both additive processes (such as deposition and growth) and subtractive approaches (such as etching and nanoscale milling). Of course, many naturally-occurring objects also fall into this size range, such as small molecules and DNA, but we do not consider these classes of materials here.

The list of ways in which nanoscale measurements can offer advantages is both long and continually growing; below are three brief examples:

(1) In general, nanoscale measurement techniques allow the ability to probe systems over distances comparable to physically relevant length scales (*e.g.*, a charge carrier's phase coherence length, a polycrystalline material's grain size, or a magnetic domain size). Over these short length scales, some quantum corrections to transport behavior, like universal conductance fluctuations, can be visualized that would otherwise be smeared out by ensemble averaging, a characteristic feature of macroscopic measurements.

(2) Material properties and charge transport can be altered when confinement is imposed in one or more dimensions. A few examples: When reduced to the single layer thickness (two-dimensional) limit, semiconducting MoS_2's bulk bandgap of 1.2 eV increases to $\sim$1.8 eV, while also changing from indirect to direct alignment of valence band maximum and conduction band minimum.[47] In the one-dimensional limit, ballistic transport can be observed in narrow wires of a variety of materials, including carbon nanotubes,[48] and gate-defined wires formed in two-dimensional electron gases hosted in semiconductor quantum wells [49]. At the zero-dimensional limit, semiconductor nanocrystals ("quantum dots") can be prepared with finely tuned size that in turn determines their electronic properties and utility in devices, *e.g.*, as light absorbers and emitters [50].

(3) Additional information can often be derived by driving systems far from equilibrium in a controllable fashion. One of Prof. Natelson's favorite examples of such a situation is the application of an electric field, where to reach a desired value of 10^6

V/m, one could apply 1V/1μm rather than 1kV/1mm, limiting the energy available to the charge carriers, which is particularly useful if one is interested in low-energy excitations.

Transport. An apt and pithy description of transport measurements comes from Dr. R. L. Willett of Bell Labs, who gave a seminar talk at Rice in which he described transport (his field of expertise) as "dirt simple." He went on to clarify, explaining that he uses this term because the typical setup of a transport measurement is very straightforward to understand: Apply a voltage and measure a current, or perhaps vice versa, using power supplies, voltmeters, and ammeters. Then, the trick is to turn some external knob (*e.g.*, vary the voltage, current, temperature, magnetic field, pressure, or carrier density) to see how the sample responds (*e.g.*, by measuring its electrical resistance). Proper interpretation of this type of study can serve as a window into the nature of the Fermi surface (*e.g.*, via Shubnikov-de Haas oscillations), visualize the results of quantum interference as electrons scatter off disorder through a lattice (*e.g.*, via weak localization effects), confirm the reality of the vector potential through the Aharanov-Bohm effect,[51] observe the integer and fractional quantum Hall effects, probe magnetic ordering and other phase transitions, and so much more. That such a conceptually simple measurement can yield so vast a wealth of useful information is precisely the great appeal of transport as a characterization technique! Finally, electronic transport also pairs well with other experimental techniques. By coupling it with a variety of complementary measurement approaches (bulk transport, magnetization, various microscopies and spectroscopies, magneto-optic measurements, diffraction studies, and so on), systems may be understood more fully than by any single technique in isolation.

2.1 Nanofabrication Techniques

For the measurements we wish to perform, we must first obtain the strongly correlated materials to be studied. The materials used here are not commercially available, and are instead grown at the research scale. Synthesis procedures depend upon the material to be grown, and may include techniques such as physical vapor deposition (PVD), chemical vapor deposition (CVD); growth of bulk crystals by vapor transport; and deposition of thin films using molecular beam epitaxy (MBE) or radio frequency (RF) magnetron sputtering. Each of these methods requires specialized equipment and substantial expertise to produce high quality materials. Rather than attempt to become material synthesis experts ourselves, our group frequently collaborates with other researchers who already possess the necessary skills and facilities, and are willing to share their materials for our work. One exception is the growth of VO_2 nanowires and micron-scale flakes, which we carry out in our lab using a physical vapor deposition technique. This procedure is well documented in published articles [52, 53], and in Dr. Heng Ji's Ph.D. thesis [54], and since this process has not been my primary work, I will not discuss it in detail here.

Frequently, we start with a prepared bulk material (large in one or more dimensions) and then process it into a nano- or mesoscale sample, using techniques such as Scotch tape exfoliation of layered materials [55], etching (which will be described in a subsequent section), and patterning of small and/or closely-spaced metal electrodes. This definition of a nanoscale region to be studied may be done as the first step of sample fabrication, or after other processing has taken place.

Once we have a SCM in hand, we must arrange a way of electrically addressing the sample in order to perform transport measurements. We want to couple in an (electrical) excitation and then measure the sample's response. Ideally, when we interface the test structure to the outside world, the intermediate "leads" have well-defined ("boring") properties that do not obscure or perturb the sample's intrinsic response; care is required to approximate these conditions in real experiments. In our work, this is typically accomplished by attaching metallic electrodes ("contacts") to the sample surface, which will be used either for applying an electrical excitation (voltage or current) or measuring the material's response to that excitation (*e.g.*, a voltage drop across the sample in response to an applied current). For bulk materials, this is often accomplished by attaching metal wires to the sample by soldering, spot welding, or adhering with electrically conductive epoxy, a tedious but straightforward process. For micro/nanoscale samples, this is more challenging as the wires cannot be placed accurately enough by hand.

We therefore turn to the toolkit of *nanofabrication*, which encompasses such techniques as various types of lithography, deposition of metals or insulators, selective etching of unwanted material to define small and isolated regions of study, and subsequent wiring up of the nanoscale material region to macroscopic leads for integration with a measurement system. The samples considered here are typically planar, including uniform films of nm-scale thickness that have been grown on flat substrates, mechanically exfoliated layered samples of thickness < 100 nm that are placed onto oxidized silicon wafers, or nanowires/micron flakes of thickness on the order of a few hundred nm, again placed on a flat substrate.

2.1.1 Nanolithography

Areas to be coated with metal and used as contact electrodes, or areas to be etched away by chemical or physical processes, can be defined using nanoscale 'stencils' through the processes of **lithography**. The basic idea is to leave some sample areas exposed for further processing, while protecting other regions so they are not affected. Below, I briefly describe our two most commonly used lithographic techniques, **photolithography** and **electron-beam lithography**. A more in-depth review of nanofabrication techniques (as applied to metal nanowires) can be found in Ref. [56], as well as instructive information in Ref. [57].

The general process starts with spreading a 'resist' material in solution onto the substrate using spin-coating. Resist materials are designed to chemically change when exposed to UV light, X-rays, or high-energy electron irradiation, and can either be *positive-tone* (the exposed area is easily dissolved in developer) or *negative-tone* (exposure makes the resist more difficult to remove, *e.g.*, by transforming it into glass or by crosslinking). A drop of the liquid resist is first placed on the substrate surface, which is then rotated at several thousand RPM in a spin-coater, spreading the resist into a uniform thin coating in intimate contact with the substrate, and of consistent thickness given fixed process parameters, all while throwing off any excess resist. The coated substrate is then baked on a hotplate (typically a few minutes, in the temperature range 100 - 200 °C) to drive off the solvent and in some cases to pass through the resist polymer's glass transition temperature. The proper exposure parameters are typically determined empirically on test samples (a process known as "dose testing").

In **photolithography**, the typical resist ('photoresist') is a commercial product such as positive-tone Shipley S1813, which is sensitive to UV light. Regions to be exposed, or else protected from exposure, are determined using a *photomask*, a glass or quartz plate coated in metal (usually Cr) that is pressed on top of the resist-coated substrate to be exposed. The photomask is pre-patterned so that certain areas of the Cr are removed, which will allow light to selectively pass through and expose the resist only in those areas. A special instrument (the mask aligner) is used for exposure, and its micromanipulator-controlled stage allows the sample to be aligned spatially with the pattern to be transferred from the photomask, and the proper mask–sample pressure to be applied.

After the substrate and photomask are aligned, light from a mercury arc lamp is allowed to pass through the mask and expose the sample for a controlled time. This technique allows quick exposures, < 10s for the time the light actually hits the sample, with all areas to be exposed illuminated simultaneously. The maximum resolution (minimum feature size or distance between features) is limited by the wavelength of UV light as well as other factors, such as the resist and mask properties. In principle, the minimum feature size would be equal to the Abbe diffraction limit according to $2dsin\theta = n\lambda$, so for UV light from a Hg lamp with $\lambda \approx 400$ nm, that would be around 200 nm. In practice, factors such as the quality of sample–mask contact and the focus achieved increase this number, and at Rice, the best available resolution is just under 1 μm.

Specialized photomasks are employed in the semiconductor industry that make use of the interference of light to reduce the minimum feature size to that needed for today's exceedingly small transistors, approaching 10 nm. These procedures are typically limited to large-scale industrial production and are not economically feasible at the research scale. Direct-write laser lithography systems are also available, removing the need for photomasks, although the minimum resolution is still limited by the illumination beam size.

Note that this whole procedure must be carried out without unwanted exposure to UV light, as that would pre-expose the entire substrate. This is avoided by working under UV-safe lighting conditions, and typically in a clean room to limit extraneous dust particle contamination.

Electron-beam lithography (EBL) is similar in spirit to photolithography, in the sense of preparing a resist-based stencil, but with several important differences. In order to improve the resolution, the resist is exposed using a focused electron beam (typically accelerated through up to 30 kV), which is raster-scanned over the sample to write shapes according to a design drawing. The electron wavelength at 30 kV is ~ 0.04 nm, and the beam after focusing can have spot size < 10 nm, so very high resolution writing is possible. No mask is required to protect the areas not to be exposed, as control of the beam allows area-selective exposure, although for writing separated area features, a fast electrostatic 'beam blanker' is useful to temporarily halt exposure of the sample without turning off the beam completely, for stability reasons. As in direct-write laser lithography, the price of higher accuracy comes in the form of reduced speed. The e-beam exposure process is serial, rather than parallel, making this technique significantly slower than photolithography (typical exposure times on the order of minutes to hours, depending on feature size and complexity, total area written, and beam current). Rather than photoresist, which is not sufficiently sensitive to e-beam exposure, other materials are preferred. Perhaps the most commonly used are the PMMA resist family, which are solutions of poly(methyl methacrylate) (PMMA) in the organic solvents anisole or chlorobenzene. Negative resists such as hydrogen silsesquioxane (HSQ) are also fairly common, though not used in the work described in this thesis. Extra requirements for EBL apply: The sample must sit in a high-vacuum chamber during exposure, so that the electron beam can propagate freely without excessive scattering off environmental gas molecules. Further, due to bombardment of high-energy electrons, the sample must be electrically conductive and grounded so that the impinging charge can be dissipated – if the sample is allowed to 'charge up,' distortions will occur in the final pattern. To accomodate insulating substrates (*e.g.*, glass, sapphire), a conductive layer such as thermally evaporated Au or Cr, or water-soluble ESpacer can be deposited on the PMMA surface and grounded during exposure, then removed before development. Regarding equipment, EBL is accomplished at Rice using specially modified scanning electron microscopes (SEMs) with beam blankers and lithography software/hardware interfaces (JEOL 6500F or FEI Quanta 400 with Nabity NPGS software), although dedicated EBL tools are also available elsewhere.

After the exposure step, and in excellent analogy with processing of conventional photographic film, the sample is 'developed' in the appropriate wet chemical solution (for photolithography, commercial MF-319 solution followed by water rinse; for EBL, a 1:3 solution of methyl isobutyl ketone (MIBK) in isopropanol (IPA), followed by IPA rinse), which removes resist from the exposed areas, leaving the bare substrate exposed. After rinsing and blowing dry with nitrogen, the sample can be inspected in an optical microscope (if the feature size is large enough) to verify that the finished pattern is acceptable.

2.1.2 Deposition and etching

The next step depends on the desired process – typically, this will be deposition of metals/oxides or etching of the sample, using the lithographically prepared resist template.

Prior to metal deposition, the patterned substrate often needs a final cleaning step to remove small amounts of resist residue. This is typically done with plasma cleaning (also called 'ashing'), in which the sample is placed in a vacuum chamber equipped with an RF coil (in our lab, a Harrick PDC 32G). The chamber is pumped out to rough vacuum, and a small amount of process gas (either oxygen or argon, depending on how delicate the sample is) is introduced into the chamber using a needle valve. The RF source is turned on, and the gas is ionized, forming a plasma of energetic particles that bombard the sample. Oxygen plasma consists of various species of ionized oxygen and ozone, which are especially effective at removing organic residues, whereas argon plasma uses the kinetic energy alone of Ar^+ to physically sputter away contaminants (without chemical reactions).

In the Natelson group, we typically deposit metals and oxides using an e-beam evaporator (Edwards Auto306 with EB3 3kW e-beam source at 5kV). The clean, patterned sample is mounted inside the chamber lid, about 0.6 m above the 4-pocket hearth where the deposition sources sit. The deposition material sources in their crucible liners are loaded in, and the chamber is pumped to $\lesssim 1 \times 10^{-6}$ mBar using a combination of an oil-sealed roughing pump, an oil diffusion pump, and a liquid nitrogen cooled baffle assembly. The e-gun source is then turned on; electrons are thermionically emitted from a hot W filament and accelerated through a $\sim$ 5 kV potential difference, then steered in a curved arc by permanent magnets until the beam hits the deposition material, which either melts or sublimes when heated by the impinging e-beam. The vapor rises up to coat the sample, simultaneously coating a calibrated quartz crystal monitor that can be used to measure the deposition rate and film thickness. The process is repeated for all desired layers of material to be deposited, up to four separate materials per process. Contacts are typically Au with an underlying adhesion layer of Ti (occasionally, V, Cr, Fe, or other adhesion layers are found to work better for certain applications; Ti is a good all-around choice). Au is a particularly nice electrode material due to its inertness and malleability; additionally, contiguous bonding pads made of Au can be readily wire bonded, or soldered with indium, to connect the sample to the outside measurement equipment.

E-beam deposition is often preferred for its smooth resulting films and near-normal (directional) incidence of atoms. Sometimes, a more isotropic deposition method is preferred; dc sputtering is a quick and convenient technique to augment e-beam deposition (for metals; not recommended for insulators). This combination of depositions is especially useful for nanoscale material samples that may be significantly taller than 50 nm above the substrate, a thickness beyond which metal deposition by e-beam becomes expensive. In that case, an initial stack of Ti/Au can be e-beam deposited, followed by a capping layer of Au by sputtering, which can coat sidewalls of the tall object and reliably connect the Au electrodes on top of the sample to those on the substrate leading out to large bonding pads. At Rice, sputtering has typically been accomplished using a small Denton sputter coater, though the cleanroom has recently added a new load-locked sputtering tool. This will likely provide much higher quality sputtered films, and additionally can deposit oxides using an RF source. Technical advice and appropriate ancillary hardware can be sought from many commercial suppliers of deposition materials and equipment; a useful chart for choosing deposition methods and crucibles is shown in Ref. [58].

Since deposition coats the entire top surface of the sample (in some areas directly on the substrate or material to be studied, in other areas on top of the resist), it is then necessary to remove the unwanted material by 'liftoff.' The sample is placed in a solvent that can remove the resist (usually acetone for the resists used here) until the unwanted material has dissolved or floated away (sometimes waiting overnight, sometimes with assistance of a directed spray of acetone or an ultrasonic bath). The sample is then rinsed in IPA and blown dry with nitrogen, and is ready for inspection and subsequent processing steps or measurement.

Alternatively, it is sometimes desirable to etch away material after lithographically defining areas to be removed. Etching is typically done by one of two methods: wet chemical etching, with acid or base solutions, or dry etching with plasma. Wet etching has the advantage of convenience (only a fume hood and dishes are required, no special instruments), but at the expense of a large potential undercut and sometimes unpredictable results from one run to another (especially in materials that are not yet well-characterized; it is usually reliable for things like GaAs, Si, or Al that have well-documented process parameters). A more controlled process using plasma etching, especially reactive ion etching (RIE), is often preferred. Although it requires a specialized machine, this technique is extremely versatile, offers many available chemistries to match particular materials, and can be tuned for isotropic or anisotropic (directional) etching. Rice's clean room has recently acquired an Oxford Plasmalab 100, which has several gases and a wide range of process temperatures available.

2.1.3 Wiring up

After all fabrication steps, the sample must be mounted on an appropriate sample holder specific to the measurement apparatus, and its electrodes connected to the holder's contacts, usually by ultrasonic wire bonding (specifically, wedge bonding). This technique uses moderate pressure and ultrasonic vibration to 'weld' an Au wire connecting the Au pads of the sample to those of the sample holder. The holder can then be mounted in the measurement system, typically by plugging into a matching socket. After wire bonding the sample, extreme care must be taken to avoid electrostatic discharge damage to the sample, especially due to handling the sample holder while the user is not grounded.

2.1.4 An example recipe

Below is an example recipe for processing SmTO/STO/SmTO quantum well samples:

1. Define pads and large leads by photolithography. I use soft contact mode; S1813 resist spun at 2500 RPM for 1 min (sample fixed ~1 cm off-axis due to typical small chip size ~3×3 mm), baked at 115 °C setpoint on hotplate for 2 min. Dose 100 mJ/cm^2. Develop 1 min in MF-319 and rinse in DI water, then blow dry.
2. 1 min Ar plasma cleaning at medium power in our lab's Harrick plasma cleaner.
3. Deposit 5 nm Ti/50 nm Au by e-beam evaporation.

4. Liftoff with ultrasonication in acetone, rinse in IPA, blow dry.

5. Define small contacts and leads by EBL. To avoid damage to QW transport properties (change of crystal structure to insulating pyrochlore), only bake PMMA 495 A4 to 115°C on hotplate (using setpoint 140°C, use IR thermometer to check real temperature). Can avoid high temperature baking and still achieve smallest contact lines $\sim$ 200 nm wide, separations down to 80 nm. After e-beam exposure, do 20 s Ar plasma cleaning before depositing 5 nm Ti/25 nm Au/35 nm Al_2O_3 (etch mask) by e-beam.

6. Define rest of etch mask using photolithography to protect the narrow bar to be used as the channel region of the device as well as protecting the large Au bonding pads. The other gold traces are protected by Al_2O_3 (don't want it on top of QW channel due to strain and charge trap issues).

7. Etch in RIE. T = 20 °C, P = 10 mTorr, helium backside cooling = 10 SCCM. Strike step: duration 3 s, flow 30 SCCM Ar at 30W directional power. Maintain RF power on by linking to next step. Switch gas to 50 SCCM Cl_2 and simultaneously increase directional RF power to 100 W. Etch 12 min.

8. Soak in acetone overnight, then sonicate and rinse in IPA.

2.2 Transport Measurements

Next, I describe the basic concepts of the electronic transport measurements we typically perform to study SCMs. They typical parameter measured is electrical resistance, defined through Ohm's law as $R = V/I$. Particularly for relatively low-to-moderate-resistance samples (say, < 1 MΩ), measurement of (longitudinal) R can be accomplished by passing a constant current through the sample while measuring the voltage drop between two electrodes along the direction of current flow. The response of R can then be determined as a function of some external parameter, which can be tuned either through the instrumental controls (*e.g.*, temperature, magnetic field, bias current or voltage), or by making a series of samples with incrementally varying properties (*e.g.*, chemical composition, electrode spacing distance, sample thickness). The inverse of R, the conductance G, can be experimentally measured by applying a constant voltage and measuring the current, and is more useful for samples with large resistance, due to limitations of voltage amplifier input impedance.

While just two contacts are needed for a minimal transport setup, there are often significant advantages to choosing a four-probe measurement. Here, conventionally the current is sourced and sunk using the outer two contacts, and the voltage drop is measured across two inner contacts. Assuming a voltmeter with input impedance large compared to the sample resistance, the voltage measurement draws essentially no current. This allows contact resistance effects to be avoided, giving a measurement of just the sample material itself, and permits more accurate values of resistivity to be extracted. Example wiring schematics for four-terminal and two-terminal resistance measurements are shown in Fig. 2.1.

Other useful and closely related measurements can be made. The Hall resistance, measured along a direction perpendicular to both the current flow and to an external magnetic field, can provide information about the material's carrier density and mobility. The carrier density is estimated using the relation $R_H = 1/ned$, where R_H is the slope of the Hall resistance vs. magnetic field plot, n is the carrier density, e the electron charge, and d the material thickness. Once the resistivity ρ is known (from separate measurements), the Hall mobility can be calculated as $\mu = 1/en\rho$.

The field effect transistor geometry is often employed to study semiconductors and insulators, featuring source, drain, and gate terminals (for different variations of three-terminal measurements). In analogy to a water valve, the gate tunes the amount of current allowed to pass between the source and drain contacts. The metallic

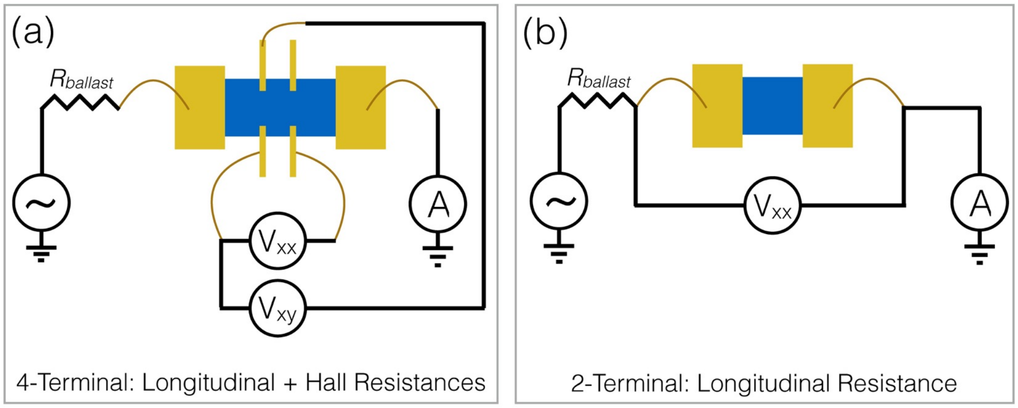

Figure 2.1: **Comparison of four-terminal and two-terminal resistance measurements** (a) A typical circuit for simultaneous measurement of four-terminal longitudinal resistance $R_{xx} = V_{xx}/I$ and Hall resistance $R_{xy} = V_{xy}/I$ using a constant-current ac source. The blue rectangle represents the material under study, with gold contacts wired to the measurement apparatus. One voltage probe contact is not used; the test structure is designed so that comparisons of measured resistances can be made using different sets of contacts. (b) A typical two-terminal resistance measurement circuit.

gate electrode is used to apply an electric field, capacitively coupled to the channel through an insulating layer, to electrostatically tune the charge carrier density in the transistor's channel via accumulation or depletion of charge. In the language of semiconductor device analysis, the current-voltage (source-drain current I_{sd} vs. source-drain voltage V_{sd} at fixed gate voltage V_g) and transfer characteristics (I_{sd} vs. V_g at fixed V_{sd}), particularly in the case of a semiconductor or insulator, can contain a large amount of information, which is extremely useful if proper interpretations can be made with mathematical models of conduction. As a simple counterexample, for good metals, I vs. V_{sd} should be a linear relationship, consistent with Ohmic behavior. In tunnel junction devices, where conduction is limited by the tunneling of carriers from states on one side of the barrier to states on the other side, the $I - V$ curve is proportional to the density of states as a function of energy.

When measuring micro/nanoscale samples, it is often desirable to limit the measurement current to small values (1 μA or less) in order to minimize Joule heating effects. This means that the corresponding longitudinal voltage drop across a small length of material may also be quite small. Conventional dc resistance measurement equipment (voltmeters, ammeters), even if sensitive enough to measure small voltages and currents, may do a poor job of resolving signals in the presence of extraneous noise detected along with the desired signal. One way to circumvent this involves the use of ac phase-sensitive lock-in detection. By modulating the signal at a known frequency and phase, the effects of noise can be greatly suppressed. The basic idea is to compare the (modulated) raw measured signal to a reference frequency and phase, strongly rejecting components of the total measured signal that are not synchronous with the reference. This results in an extremely sensitive detection scheme that is robust against many sources of noise, one that is well suited for nanoscale transport measurements, and which is used in most of the work in this thesis.

To implement this, a lock-in amplifier is used to source an ac voltage at a certain frequency (for these measurements, typically a frequency near dc that is not a multiple or even fraction of 60 Hz, to avoid line frequency interference from the power supply). For constant-current measurements (usually of low-to-moderate resistance samples, below $\sim$ 1 MΩ), a large series resistance (a 'ballast resistor') is used, effectively forming a voltage divider in combination with the sample resistance. As long as $R_{ballast} >> R_{sample}$, most of the voltage is dropped across the ballast resistor, resulting in a nearly constant current. The same lock-in amplifier's measurement input can then be used to detect, *e.g.*, the longitudinal voltage drop V_{xx} with high precision. A second lock-in unit can be used to simultaneously measure, *e.g.*, the Hall voltage V_{xy} or the current I. The lock-in amplifiers (here, a Signal Recovery 7265 and 7270) are augmented with external voltage or current preamplifiers (Stanford Research Systems SR 560 or 570) to boost the maximum input impedance or further improve sensitivity. The measured signals can then be recorded *via* a data acquisition system (National

Instruments BNC ADC) and NI LabVIEW programs to import and save the data on a PC.

2.3 Measurement Environment: The PPMS

For the transport measurements we want to perform, it is essential to control as many aspects of the sample environment as possible, usually varying one parameter while holding all others fixed. Environmental parameters we can directly control include temperature, pressure, surrounding gas, and magnetic field (both strength and direction). In order to achieve stringent control of these parameters, an appropriate measurement platform is required.

The measurements presented here are almost entirely performed using a Quantum Design Physical Property Measurement System (PPMS), a commercial ^{4}He variable-temperature cryostat (range 1.8 – 400 K), with an integrated 9 T superconducting solenoid magnet. The main portion of the system is the 'probe,' which consists of a sample chamber, surrounding cooling annulus, and temperature control hardware. This probe is mounted inside a dewar containing liquid helium. A schematic diagram of the system is shown in Fig. 2.2. For transport measurements, it includes 12 dc wires (*i.e.*, for low-frequencies, not RF coax) in twisted pairs for electrical connections to the sample, which is mounted on a "puck." This consists of a copper base (for thermal connection to the cold finger of the cryostat), a circuit board with bonding pads for wire bonding to the sample, and permanently wired connections to a 12-pin plug that mates with an internal socket in the sample space of the cryostat. Thus, the puck serves to interface the sample both electrically and thermally with the measurement system. An alternative "horizontal rotator" puck is also available that allows the sample to mount on a rotation stage, for changing the orientation of the plane of the sample substrate relative to the z-direction magnetic field. In order to mechanically and thermally anchor samples to the puck, they are mounted either with a small dab of special thermal grease (Apiezon N-grease, which is vacuum and low-temperature compatible) or silver paint (particularly for very small chips that slide around on grease during wire bonding). In the case of an electrically conductive substrate that needs to be isolated from the grounded copper stage (*e.g.*, when using a doped Si wafer as a back gate), an intermediate insulating layer of Kapton tape or a sapphire wafer piece can be placed between the sample and the puck.

After sample installation, the chamber is alternately pumped to rough vacuum and purged with helium gas several times, then backfilled with a few Torr of helium gas as a thermal exchange medium. The sample chamber of the PPMS is insulated from the nearby liquid helium bath by layers of vacuum jacket and metallized plastic superinsulating material, so the sample can be held at any temperature within the system's range without warming the nearby helium bath reservoir. Integrated heaters, gas flow control hardware, and an electronic PID temperature control system allow accurate temperature control (both fixed T and sweeps). Temperatures below the boiling point of liquid helium, 4.2 K, are achieved by pumping on the cooling annulus to reduce the pressure; the pumping rate limits the minimum temperature to 1.8 K.

A magnetic field strength up to 9 T can be applied using the built-in superconducting solenoid magnet. The sample is positioned as close as possible to the middle of the solenoid, vertically and radially, where the field is most uniform. The current in the magnet (and thus the field strength) can be controllably ramped up or down by the high-current magnet power supply that is interfaced through a heated switch. By turning off the heater, a small section of the wire will return to its superconducting state, thus disconnecting the power supply and allowing a persistent current (the supercurrent) to flow in the solenoid. The direction of the magnetic field (up or down) can be switched by reversing the direction of current flow.

Now that we are familiar with the basic experimental techniques and equipment used in nanoscale transport studies, we can proceed to discussion of the main experiments and their results. The following four chapters will consider the material systems studied one by one.

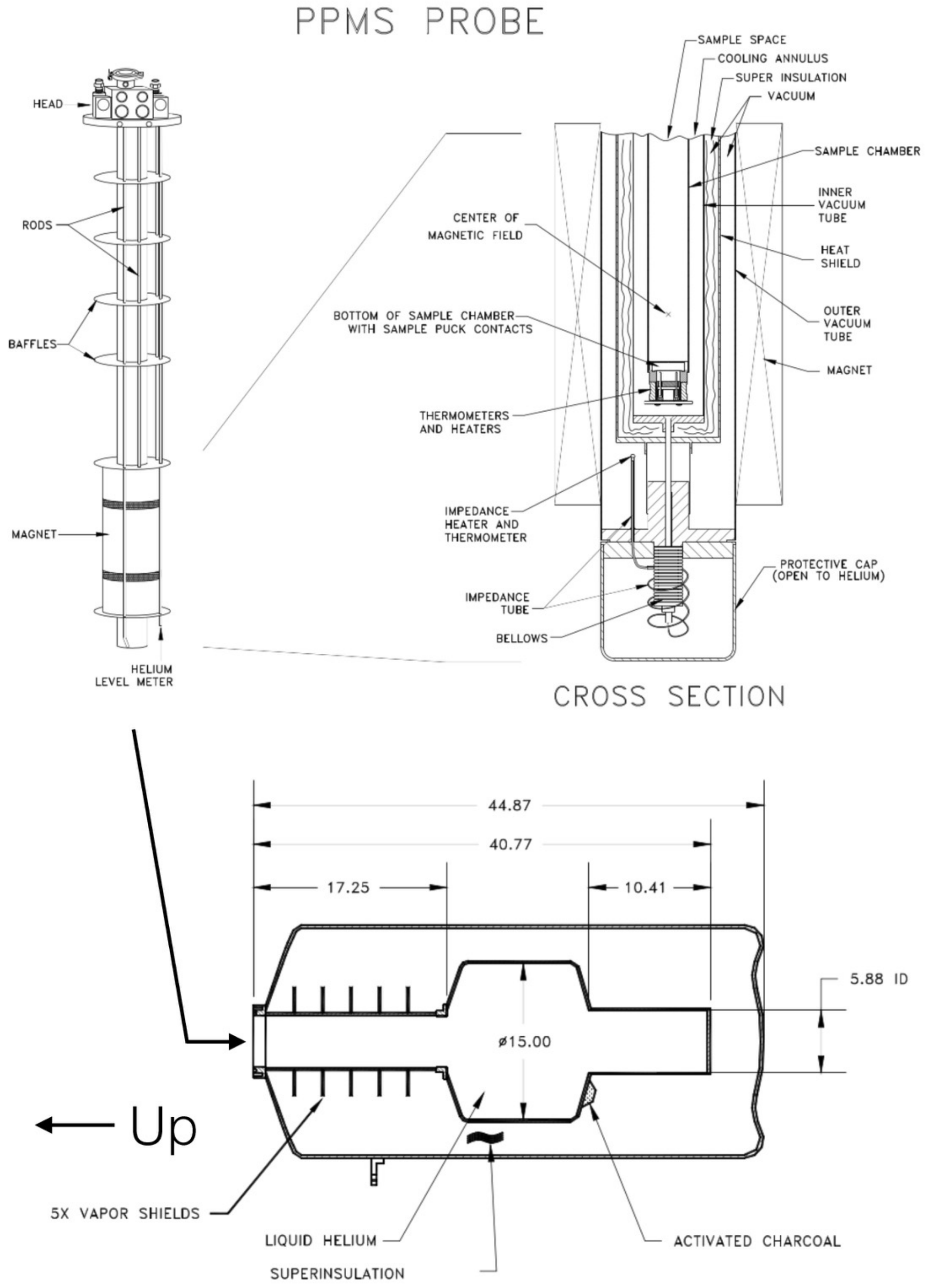

Figure 2.2: **PPMS Probe and Dewar Design Schematics** Upper left: PPMS probe including sample chamber (center tube) and superconducting magnet. Upper right: Close cross section view of sample chamber and helium flow impedance area. Lower image: Helium dewar in which the PPMS probe is installed. The dewar is shown sideways; in normal operation, the left side flange faces up. The large central cavity is designed to maximize liquid helium volume around the magnet. Figure reproduced with permission from [5]. Copyright © 2017 Quantum Design Inc.

Chapter 3

Mesoscopic Quantum Effects in a Bad Metal, Hydrogen-Doped Vanadium Dioxide

---

Part of this chapter is adapted from the published work [8] :

Mesoscopic Quantum Effects in a Bad Metal, Hydrogen-Doped Vanadium Dioxide

by Will J. Hardy, Heng Ji, Hanjong Paik, Darrell G. Schlom, and Douglas Natelson

J. Phys.: Condens. Matter **29**, 185601 (2017)

DOI: https://doi.org/10.1088/1361-648X/aa674d

In this chapter, we expand upon the story of vanadium dioxide, VO_2, a widely-studied SCM that, despite decades of research, remains not well understood in certain aspects. Fundamental aspects such as the exact band structure and relative populations of n-type and p-type carriers remain murky. The most obvious correlation-driven feature of VO_2 is its metal-insulator transition, from a high-temperature rutile poor metal state to a low-temperature monoclinic insulating state. In the bulk, this transition occurs near 340 K and is first order, though the details of the transition can change in response to external parameters such as strain (see Fig. 3.1, as well as the phase diagram in Fig. 1.3). The precise origin of this transition has been debated for decades. It is generally believed to be either Mott-like, driven by electron-electron interactions with a subsequent structural transition, or Peierls-like, with the structural distortion of V-V dimerization instead driving the electronic transition to the insulator (see Ref. [45] for a clear discussion on the matter, in which an argument is made for a combination of the two physical pictures). Modern ultrafast techniques have been employed to help resolve the issue [59], and indeed, both mechanisms are observed, though the Mott order disappears first upon photoexcitation. A more recent study confirms this using X-ray absorption spectroscopy (XAS) measurements of thin films, finding evidence for softening of electronic correlations starting 7 K below the transition to the metallic phase [60]. This transition has been a particularly attractive candidate for both fundamental research as well as proposals for practical devices that rely on the sensitivity and speed of the phase transition, along with its magnitude in terms of the change in electronic and optical properties.

The Natelson group's work on strongly correlated material systems over the last several years has focused extensively on VO_2, with the intent of better understanding this 'prototypical' SCM, through the particular viewpoint of nanoscale transport measurements. [61, 62] These studies began when Dr. Jiang Wei joined our group as a postdoctoral scholar and brought expertise in growing VO_2 nanowires, a process which is now readily available in our lab. Much of our group's measurement effort has followed in the wake of the discovery of Wei et al. that atomic hydrogen can diffuse into pristine VO_2 along a preferred crystallographic axis (rutile c-axis of the metallic phase), which stabilizes its relatively conducting but badly metallic phase down to low temperatures, effectively suppressing the metal-insulator transition (see Fig. 3.2). Several studies were conducted by our group to understand this hydrogen doping process. [7, 63, 64, 65] More recent efforts, which are the focus of this chapter, have further centered on understanding the low-temperature magnetotransport be-

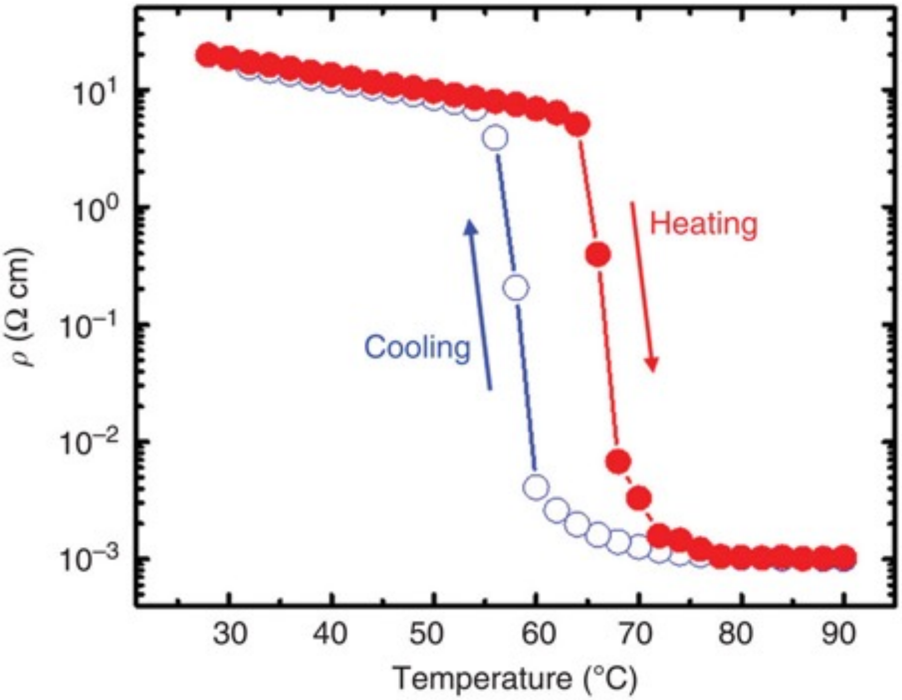

Figure 3.1: **Insulator-metal phase transition in vanadium dioxide.** Here, the transition is visualized through a dramatic, hysteretic change of resistivity as a function of temperature. The resistivity falls by approximately four orders of magnitude over a narrow temperature range of a few Kelvin, yet the metallic state's resistivity is still large – on the order of 1 mΩ cm. Figure reproduced from [6] under a Creative Commons license.

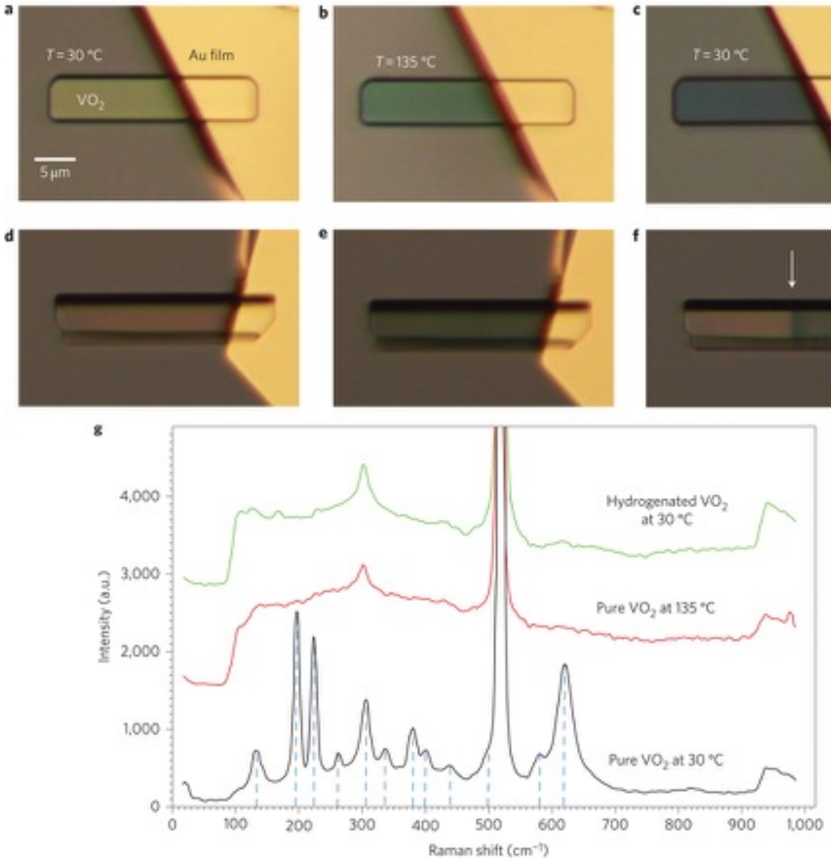

Figure 3.2: **Hydrogenation of VO_2.** Optical images of two gold-contacted VO_2 beams before catalytic hydrogenation at (a,d) 30°C in the insulating phase or (b,e) 135 °C in the metallic phase, and (c,f) at room temperature after hydrogenation. The change in crystal structure that occurs at the phase transition also modifies the material's optical properties, and the transition is readily visible via the color change. Note that panel (c) shows a fully hydrogenated beam, whereas (f) shows a partially hydrogenated beam with a clear color-contrast boundary marking the approximate extent of hydrogen diffusion from the gold-contacted end. Panel (g) shows the Raman spectra of pristine VO_2 in the insulating and metallic states, and hydrogenated VO_2 at room temperature, with its spectrum very similar to the pristine metallic (high-temperature) material. Figure reproduced with permission from [7]. © 2012 Macmillan Publishers Ltd.

havior of H_xVO_2, both of nanowires grown in-house, and of thin film samples provided by Prof. Darrell Schlom's group at Cornell.

From our perspective, the practical advantages of using VO_2 as a preferred candidate for correlated material studies include the ready availability of high-quality material samples in various geometries, as well as decades of relevant literature. The main downside, however, is the transition to the insulator, which prevents low-temperature transport studies of the pristine material. Hydrogenated VO_2 can partially overcome this challenge, as will be described below.

The work presented in this chapter was begun by my predecessor in the Natelson lab, Dr. Heng Ji, who performed some of the experiments described herein (work with which I assisted) and included those results in his in April 2015 Ph.D. thesis [54]. An initial manuscript was submitted for peer review shortly after his graduation, but referees suggested major revisions before publication. I have since continued to work on this project in order to complete needed measurements on newly received (and higher-quality) thin film samples, as well as significantly edit the original manuscript. The overall interpretation of the body of results has been revised in light of the new film data. The project is now at the manuscript submission stage as of February 2017, and Dr. Ji and I will be noted as equal contributors. A large part of the work was either performed jointly by both of us before Dr. Ji's graduation, or else is work I have done since then, but I will note sections in the following text where work was mainly done by Dr. Ji.

3.1 Low-Temperature Transport Studies of H_xVO_2

The standard treatment of quantum corrections to semiclassical electronic conduction assumes that charge carriers propagate many wavelengths between scattering events, and succeeds in explaining multiple phenomena (weak localization magnetoresistance (WLMR), universal conductance fluctuations, Aharonov-Bohm oscillations) observed in polycrystalline metals and doped semiconductors in various dimensionalities. We report apparent WLMR and conductance fluctuations in H_xVO_2, a poor metal (in violation of the Mott-Ioffe-Regel limit) stabilized by the suppression of the VO_2 metal-insulator transition through atomic hydrogen doping. Epitaxial thin films, single-crystal nanobeams, and nanosheets show similar phenomenology, though the details of the apparent WLMR seem to depend on the combined effects of the strain environment and presumed doping level. Self-consistent quantitative analysis of the WLMR is challenging given this and the high resistivity of the material, since the quantitative expressions for WLMR are derived assuming good metallicity. These observations raise the issue of how to assess and analyze mesoscopic quantum effects in poor metals.

Since the late 1970s, many insights have been gained into the effects of quantum coherence and quantum interference on electronic conduction in ordinary metals and semiconductors[66]. Conduction is influenced by the interference between trajectories as charge carriers scatter from static disorder, while inelastic scattering processes suppress coherence on the scale of the coherence length, L_ϕ. Magnetic flux alters relative phases of various trajectories *via* the Aharonov-Bohm phase. Magnetoresistive effects (*e.g.*, weak localization[67], universal conductance fluctuations[68]) are then experimental means of studying the evolution of quantum coherence as a function of control parameters such as temperature, dimensionality, disorder, and carrier density. The standard theoretical treatment of these effects is perturbative in $(1/k_{\mathrm{F}}\ell)$, where k_{F} is the Fermi wavelength and ℓ is the carrier mean free path, so that carriers propagate many wavelengths between scattering events, a hallmark of a "good metal."

In contrast, some materials are "bad metals," such that $k_{\mathrm{F}}\ell$ as inferred from the resistivity is < 1, or roughly equivalently, when the Mott-Ioffe-Regel limit is violated [22, 23]. This situation most commonly arises at high temperatures in correlated materials. Conventionally, when scattering is dominated by disorder, materials with small $k_{\mathrm{F}}\ell$ cross over into the strongly localized regime as T is lowered[69]. Quantum corrections to conduction in bad metals are comparatively unexplored.

As we have reviewed previously, VO_2 is a strongly correlated material with an insulator-to-metal phase transition at about 340 K. Its conductivity can increase by up to 5 orders of magnitude when the material is heated across the transition temperature and the material transforms from a low temperature, monoclinic, insulating phase to a high temperature, rutile, conducting phase[70]. This metallic state is a moderately correlated bad metal[71] that has not been studied previously at low temperatures due to the transition to the insulator. Atomic hydrogen can be doped into VO_2, either with[7, 64] or without catalyst[65], and this doping dramatically affects the properties of the material. Based on the neutron powder diffraction measurements, over a broad range of concentrations of the intercalated hydrogen atoms (x in H_xVO_2), new orthorhombic phases are stabilized, with crystal structures similar to the pristine tetragonal rutile structure except that a-axis lattice parameter is slightly different from that of the b-axis. These new phases possess electronic properties similar to the pristine rutile phase in terms of resistivity (and theory anticipates their metallic behavior), and can be cooled down to 2 K without any phase transition. Here, we find that in hydrogen-doped nanobeams and micron-scale flakes, the resistivity is only weakly dependent on the hydrogen concentration (as inferred from varying the hydrogen exposure time), consistent with the metallicity appearing as the result of thermodynamic phase stabilization[64] rather than traditional doping. A different situation is observed in thin films, however, where instead of reaching a stabilized conducting state that does not change appreciably with further hydrogenation, the films initially become more conducting upon hydrogen exposure, then trend more insulating with longer exposure times. This could presumably occur if the doping fraction $x \to 1$ (stoichiometric HVO_2, which is reported to have completely filled $3d$ orbitals, and thus no available states at the Fermi level), as was recently observed in a study on reversible hydrogen doping in thin VO_2 films[72]), or it may be a consequence of the different strain situation for films compared to bulk VO_2 or micro-crystals. No systematic experimental study has been done of the low-temperature electronic transport properties of hydrogen-doped VO_2, in the case of nanobeams, micro-crystals, or thin films.

In this chapter, we report the low temperature transport properties of hydrogenated VO_2. Three types of single-crystal samples have been used: epitaxial thin films on single-crystal TiO_2 substrates (the rutile polymorph), nanobeams, and micron-scale flake-like crystals. Hall measurements on the pristine metallic film samples at room temperature, as well as on the doped films at various temperatures, show a very small Hall signal, similar to that reported previously at room temperature and above on pristine, metallic VO_2[73, 74]. The very small Hall response in the doped material implies that multiple carrier types are likely present in the metallic state. After hydrogenation, we observe abundant magnetoresistance (MR) responses in these samples at low temperatures. For thin films of 10 nm thickness, an overall high-field positive MR is observed at low temperatures, while the low-field MR may have either a peak or dip at helium temperatures. The nanobeam and micron flakes also exhibit positive MR of increasing magnitude as T is reduced below 20 K, independent of field direction, qualitatively similar to a 3d weak anti-localization response. Mesoscale samples show conductance fluctuations as a function of magnetic field. Interpretation of these results is discussed.

3.2 Experimental Techniques

Three kinds of single-crystal VO_2 samples were used for hydrogen doping and transport measurements. Epitaxial VO_2 thin films were grown by Hanjong Paik, working under the supervision of Prof. Darrell Schlom at Cornell University. After the rutile (001) TiO_2 single-crystal substrates were cleaned using a 23% HF aqueous solution to reduce the metal impurity contamination on the surface, the films were grown by reactive molecular-beam epitaxy (MBE) in a Veeco GEN10 system. [75]. Initially, films of 30 nm thickness were grown, but were found to be extremely susceptible to microcracking during temperature cycling and cutting the as-grown samples into smaller pieces, as observed recently by Paik *et al.* [75] To avoid this issue, 10 nm thick films were grown in the same manner (three nominally identical samples denoted HP1703, HP1704, and HP1706), and shipped to Rice. The samples were measured after minimal processing (contact deposition only). I used e-beam evaporation to deposit six contacts (5 nm vanadium followed by 35 or 50 nm gold) through a shadow mask along the side of 1 cm × 1 cm VO_2 films to form Hall bar structures. Heng Ji prepared samples of two other types: VO_2 nanobeams and micron-scale flake-like single crystals, both grown by physical vapor deposition (PVD) on Si/SiO_2 substrates using methods reported previously,[76, 7] with wire or flake morphology determined by the position of the substrate within the growth furnace. The nanobeams could be up to 100 μm in length, and the widths and thicknesses ranged from 50 nm to 1 μm. For the flakes, the thickness was between 50 – 100 nm, and the dimensions were tens of μm by tens of μm. In a typical growth run, both wires and flakes could be achieved on one large substrate, improving the likelihood that the two sample types would have similar properties. Ji used electron-beam lithography to define the contact areas for 4-terminal transport measurements, and deposited 5 nm V / 35 nm Au contacts, using wires and flakes less than 200 nm thick in order to avoid difficulties in contact continuity at the edges of thick samples.

After an initial temperature-dependent resistivity measurement (in the range 200–400 K), all test structures were then treated by a catalyst-free atomic hydrogenation process, with help from Nam Dong Kim (Rice University).[65] In a dedicated tube furnace, hydrogen gas was flowed into the tube at rate 100 cc/min; a tungsten filament heated by a 45 W power supply was located in the middle of the tube, and samples to be hydrogenated sat 1 cm away from the filament on the downstream side. A valve on the pumping side was adjusted to stabilize the tube pressure at 10 Torr. During this process, the hot filament splits molecular hydrogen gas at some rate, and as observed previously the hydrogen atoms then diffuse into rutile VO_2 along its *c*-axis, without the need for any catalyst (diffusion in the rutile structure is much faster than in the monoclinic phase). Because the VO_2 film on the TiO_2 substrate has its metal-insulator phase transition shifted to below room temperature, due to its high strain from the lattice mismatch with the substrate, the atomic hydrogenation process can take place at room temperature. As the *c*-axis of the film is perpendicular to the substrate, the doping process took no more than 30 seconds to complete for the 10 nm thickness (2 min for the 30 nm thickness), with hydrogen entering the film evenly from the whole surface, resulting in apparently homogeneous doping (based on the uniform appearance and color of the treated films, although we later discuss evidence for local nonuniformity and time variation of uniformity of the doping). Accurate determination of the hydrogen concentration is challenging and requires specialized analytical techniques sensitive to light elements, such as annular brightfield scanning transmission electron microscopy (ABF-STEM), elastic recoil detection (ERD),[72] or highly destructive techniques involving chemical decomposition of the sample and analysis of the reaction products,[77] which are beyond the scope of this work. For the films, it is possible that there would be some modification of the strain at the interface between the VO_2 and TiO_2 after doping, as suggested by previous work that shows changes in the unit cell parameters with hydrogen incorporation[64]. This could in principle be assessed with appropriate X-ray scattering techniques before and after hydrogenation. An attempt was made to perform these experiments, but the “after” results were not conclusive, possibly due to aging effects (as well as the uncontrolled sample conditions during shipment between Rice and Cornell). Given the large pre-existing strain due to the TiO_2/VO_2 lattice mismatch, however, we believe that any such modification of strain is likely small compared to the pre-existing strain.

The first film sample, denoted HP1703, was exposed to atomic hydrogen for an initial time of 2 minutes, followed by a second treatment for an additional 2 minutes, and showed evidence of doping beyond the point of stabilizing the metallic phase. After the initial 2-minute exposure, the sample shows a quite insulating temperature dependence of resistivity upon cooling to 75 K, becoming even more so after the second 2-minute atomic hydrogen exposure ($>$ 2000 mΩ-cm; see Figure 3.3). This is consistent with a recent report that epitaxial VO_2 films doped with hydrogen by the catalytic spillover method first become more conducting at low doping levels, but with progressively more doping the trend reverses, resulting in substantially insulating behavior as the stoichiometry approaches HVO_2.[72] Further, it would imply that the doping fraction in this film is large ($x \to 1$) based on comparison with prior diffraction studies of hydrogenated VO_2 powder, where an increasing hydrogen doping fraction (up to $x \sim 0.6$) is accompanied by stabilization of two successive orthorhombic crystal phases, which are most similar to the pristine metallic state.[64] Since the goal of this work was to stabilize a relatively conducting (but still badly metallic) phase down to low temperatures, two subsequently measured samples, HP1704 and HP1706, were doped for only 30 s. These remain relatively conducting over the temperature range 2–300 K (though with resistivity magnitudes well above the regime of good metal behavior). Despite the fact that they have the same geometry (effective number of squares) and were both doped for the same nominal time, their post-hydrogenation temperature-dependent resistivity curves are substantially different from each other, by a factor of $\sim 2.7\times$ at room temperature and by $\sim 6\times$ at 2 K (as shown in Figs. 3.4a and 3.5a). This may imply an extreme sensitivity to the exact doping level, with a crucial dependence on the treatment process details (a difference of a few seconds in doping time, or the exact sample-filament distance). The built-in strain of the films may also be relevant, in light of this apparently enhanced sensitivity to hydrogen exposure time compared with powder or micro-crystal samples.

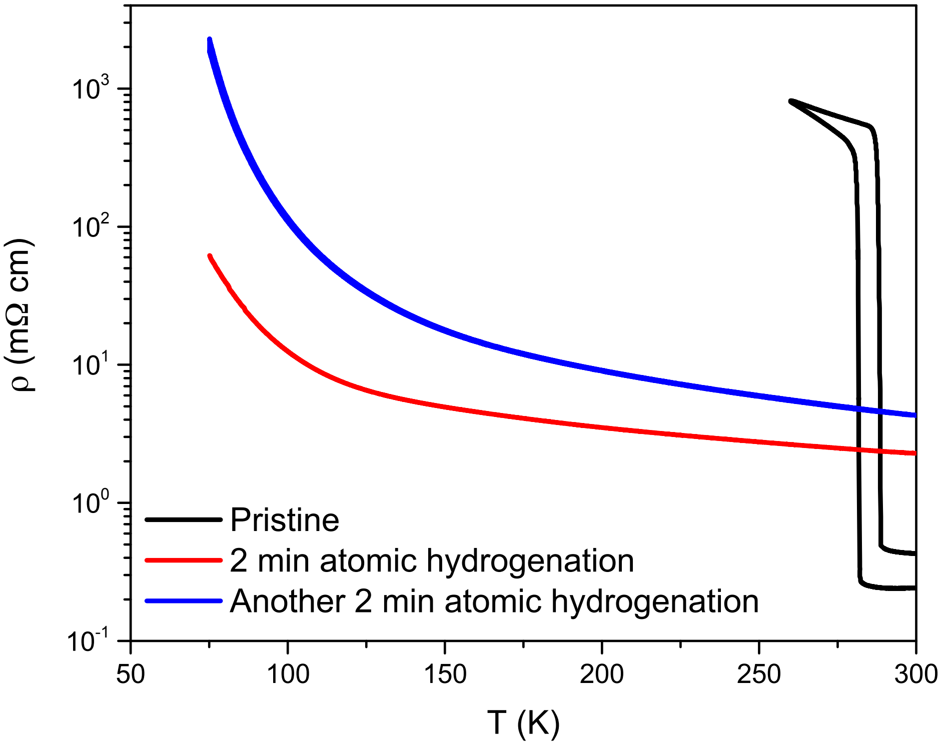

Figure 3.3: Temperature dependent resistivity of film sample HP1703 (10 nm thickness), showing the effect of increasing atomic hydrogenation time. A two-minute hydrogen exposure results in an enhanced room-temperature resistivity (red curve) compared to the pristine state (black curve), and a second exposure of two minutes further increases according to this trend (blue curve). The insulating-like curve slope with decreasing temperature is much steeper and larger in magnitude than for film samples HP1704 and HP1706, which were doped for just 30s each. Such a trend toward insulating behavior with longer hydrogen exposure time was not observed in the PVD-grown nanobeams or flakes, likely due to the significantly slower diffusion time and lower hydrogen doping level for those samples compared to films (which is, in turn, a consequence of the different sample geometries and their crystal orientations and strain states). Figure reproduced from [8].

For hydrogenation of the wires and flakes, performed by Heng Ji, the furnace had to be turned on to increase the ambient temperature to 425 K, so that the VO_2 crystals had the rutile structure best suited for hydrogenation. Since the c_R-axis for these crystals was along the long dimension of the wires or along an in-plane dimension of the flakes, it took 15 minutes for the VO_2 samples to be fully hydrogenated (in the sense that samples appeared homogeneous in color after cooling to room temperature, and showed no significant changes in measured electronic properties if hydrogenated for longer periods). The hydrogen content within the samples is not readily quantifiable experimentally using X-ray diffraction (XRD) due to the small crystal size, nor via transmission electron microscopy (TEM) due to limited resolution and the fact that hydrogen atoms move upon electron irradiation.[7] We point out that for PVD-grown crystals, the measured electronic properties appear to be fairly independent of hydrogen content above the threshold required to stabilize the orthorhombic phase down to low temperatures, perhaps due to the relatively slow hydrogen diffusion compared to the film geometry.

All the transport measurements were done in a Quantum Design Physical Property Measurement System (PPMS), with a base temperature of 1.8 K, and magnetic field up to 9 T. A typical 4-terminal measurement setup was applied for all temperature-dependent resistivity and magnetoresistance (MR) measurements. A low frequency (7–17 Hz) AC signal was powered and collected by two lock-in amplifiers (Signal Recovery model 7270 and model 7265), one current pre-amplifier (Stanford Research Systems model SR570), and one voltage pre-amplifier (Stanford Research Systems model SR560). For Hall measurements, one additional voltage pre-amplifier was used. For all low temperature measurements, currents were limited to below 1 μA to minimize Joule heating.

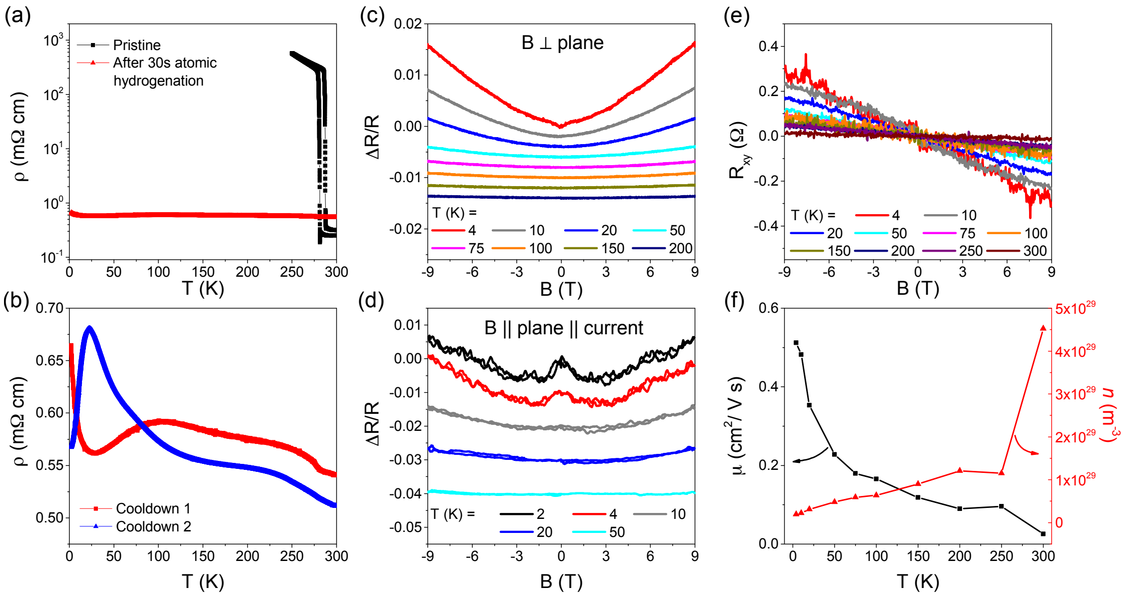

Figure 3.4: (a) Temperature dependence of the resistivity of the VO_2 film sample HP1704 (10 nm thickness), before (black squares) and after (red triangles) the 30 s atomic hydrogenation process. The metal-insulator transition in the pristine material is marked by a sharp increase of resistivity of $>$ 3 orders of magnitude at $\sim$ 282 K on cooling, whereas after hydrogenation, the phase transition disappears and the resisitivity is nearly flat with temperature. (b) A closer view of the resistivity immediately after hydrogenation (red squares) and after a subsequent warming and cooling cycle (blue triangles), showing that the detailed shape of the curve changes over time, even though the sample remains in the controlled cryostat environment, perhaps due to time evolution of the hydrogen distribution in the lattice. (c,d) Hydrogenated film MR curves at various temperatures with the field (c) perpendicular or (d) parallel to the substrate and current direction. Curves are offset by (c) -0.002 or (d) -0.01 for clarity. An overall high-field positive MR develops as the temperature is reduced below $\sim$ 150 K, growing as the temperature decreases. A small dip (perpendicular case) or peak (parallel case) appears at 4 K and below, likely due to localization effects. (e) Hall resistance of the hydrogenated film measured at various temperatures. The data have been antisymmetrized to remove a longitudinal component artifact. (f) Calculated mobility (left axis) and carrier density (right axis) of the hydrogenated film inferred from resisitvity and Hall data assuming a single carrier type (n-type). The unphysically large inferred carrier density implies that more than one carrier type likely contributes to transport in the hydrogenated film. Figure reproduced from [8].

3.3 Results and Discussion

3.3.1 VO_2 film

Before hydrogenation, the VO_2 films of 10 nm thickness show a typical sharp phase transition behavior (Fig. 3.4a) with the transition temperature at ~ 282 K on cooling (290 K for the 30 nm film), instead of the 340 K transition of unstrained bulk VO_2. This reduced transition temperature has been reported previously, and was well explained by a compressive strain along the c_{R}-axis[78]. After the 30s room-temperature atomic hydrogenation process (samples HP1704 and HP1706), the films remain in a conducting state with a resistivity similar to that of the pristine metallic state. Unlike a good metal, the temperature dependence of resistivity of the films shows an overall negative slope, with behavior below 100 K that changes after subsequently warming up and cooling down again (Fig. 3.4b), but without any obvious sign of impending strong localization. The different response on the subsequent cooldown may be due to redistribution of hydrogen concentration in the lattice over time. The total change of resistivity from 300 K to 2 K is no more than a few times for both 10 nm films hydrogenated for 30 s (or less than an order of magnitude for the 30 nm film).

Even at room temperature, the resistivity of the hydrogenated VO_2 film is much higher than expected for a typical metal. Based on the Mott-Ioffe-Regel limit (MIRL), the semiclassical transport model for quasiparticles is only applicable when the mean free path ℓ is larger than the lattice constant a, leading to a criterion of $k_{\mathrm{F}}\ell \sim 1$ (or 2π). This leads to a maximum resistivity of metals in the conventional model on the order of $a\hbar/e^2$. When considering VO_2 with a lattice constant of 2.85 Å along the c_{R}-axis[71], its maximum resistivity should then be around 117 $\mu\Omega$-cm. In our measurements, however, the resistivity of the hydrogenated VO_2 film of 10 nm thickness is larger than 540 $\mu\Omega$-cm for one sample (HP1704) and larger than 1450 $\mu\Omega$-cm for a second sample (HP1706) (or 700 $\mu\Omega$-cm for the 30 nm film) throughout the temperature range from 300 K to 2 K, with similar values measured for PVD-grown wires and flakes, implying the inadequacy of semiclassical quasiparticle conduction in VO_2. The violation of MIRL has been observed at high temperature in some transition metal oxides, like VO_2[71], and some correlated superconducting oxides, like Sr_2RuO_4 [79], $La_xSr_{1-x}CuO_4$, and $YBa_2Cu_3O_7$[80]. There are few reports about violation of the MIRL near the threshold of strong localization at low temperature[81, 82, 83].

I performed MR measurements on the VO_2 films (samples HP1704, HP1706) at various temperatures. For sample HP1704, which appears to be less doped due to its smaller increase of resistivity with temperature, the MR is shown in Fig. 3.4 with the external magnetic field either perpendicular (Fig. 3.4c) or parallel (Fig. 3.4d) to the film surface and current direction. The relative change of resistance $\frac{\Delta R}{R_0} = \frac{R(B)-R_0}{R_0}$ is plotted as a function of external field strength. In both orientations, an overall high-field MR develops and grows as the temperature is reduced below $\sim$ 150 K, with a maximum magnitude less than 2% at low temperatures, and a slope that shows no sign of saturation by 9 T. At the lowest temperatures (2 or 4 K), the low-field region of the MR curves shows a dip when the field is perpendicular to the plane, or a peak when the field is parallel to the plane. Film HP1706, which despite nominally identical processing appears to be more strongly doped (based on its larger room-temperature magnitude of resistivity after doping and steeper increase of resistivity with falling temperature, shown in Figure 3.5(a)), also shows a high-field positive MR of similar magnitude at temperatures below $\sim$ 150 K, and has a zero-field peak at temperatures below 4 K with the field perpendicular to plane (Figure 3.5(b)).

This magnitude of the magnetoresistance, its functional form, and its suppression with increasing temperature, resemble the predictions of the theory of weak localization[67]. Weak localization usually occurs at low temperatures when the in-

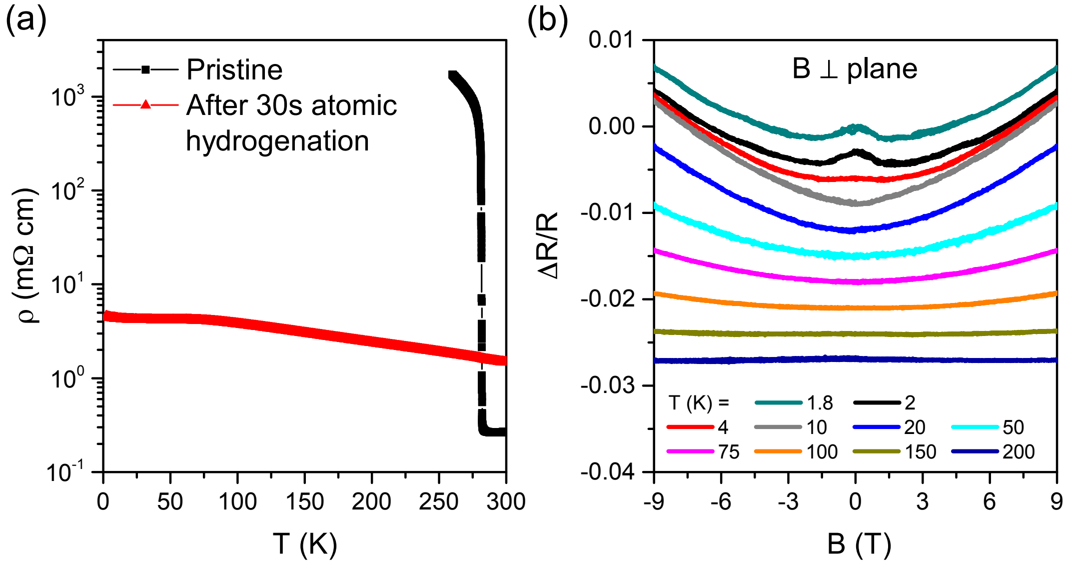

Figure 3.5: Transport measurements of the 10 nm thick film HP1706. (a) Resistivity before (black curve, cooling data) and after (red curve) 30 s atomic hydrogenation. (b) MR curves of the hydrogenated film at various temperatures, with the field perpendicular to the plane of the sample. The curves are offset by -0.003 per temperature value for clarity. An overall positive sign of MR develops below ∼ 150 K, and a zero-field peak emerges when cooling below 4 K. Figure reproduced from [8].

elastic scattering time (τ_i) is much larger than the elastic scattering time (τ_e), so that the electrons can experience momentum relaxation and diffusion before loss of phase coherence. In the absence of strong spin-orbit coupling, trajectories corresponding to closed loops and their time-reversed partners interfere constructively, favoring back-scattering, *i.e.*, localization, and result in a slightly larger resistance. When a magnetic field is applied, the constructive interference is broken due to the Aharonov-Bohm phase, suppressing the back-scattering and leading to negative MR. In a system with strong spin-orbit scattering, this interference at the origin point becomes destructive, suppressing back-scattering; the MR sign flips to positive, producing weak anti-localization. The functional form of the MR depends on the effective dimensionality of the sample with respect to the coherence length. In conventional (good) metal systems, WL or WAL data can be modeled by functional forms that are tailored for the case of either two [84] or three [85] dimensions, and the relevant field scales that allow determination of the coherence length, spin-orbit contribution, spin-flip contribution, and inelastic scattering can be deduced from the fitting parameters.

Quantitatively fitting the data to the theoretical expressions for WL/WAL with self-consistent values of parameters, particularly the role of elastic scattering, is not possible. The MIR-violating resistivity and difficulty extracting meaningful carrier densities from Hall data are the source of the problems. We can use the Einstein relation, $\sigma = e^2 D\nu(E_\mathrm{F})$, where $\sigma = 1/\rho$, e is the electronic charge, and $\nu(E_\mathrm{F})$ is the density of states at the Fermi level, to infer a value for D. Using the estimate of $k_\mathrm{F} \sim 10^8$ cm^{-1} employed by Qazilbash *et al.*[71] and assuming a spherical Fermi surface and an effective mass close to the free electron mass, one finds $\nu(E_\mathrm{F}) \sim 8 \times 10^{46}$ J^{-1}m^{-3}, implying a diffusion constant $D \sim 5 \times 10^{-5}$ m^2/s when $\rho = 1$ mΩ-cm. As expected for the MIRL situation, however, this also implies a mean free path small compared to the lattice spacing and is therefore likely unphysical. We note that employing a different value of the effective mass m^* could also affect the inferred D, with increasing m^* causing a reduction of D. Early works [86] estimate the effective mass at $1.6 - 7\ m_0$, depending on the method, while more recent analyses based on measurements of optical conductivity put the effective mass at no more than a few times the free electron mass. For example, the work by Okazaki *et al.* [87] suggests $m^* \sim 4\ m_0$, while recent theory work[88] suggests $m^* \sim 2\ m_0$. Further, optical conductivity results indicate the possibility of a diverging effective mass as the system nears the metal-insulator transition [71], which would imply a vanishing diffusion constant. As discussed below in the context of the Hall number, the electronic structure of metallic VO_2 remains a topic of debate[89].

These issues with D and $k_\mathrm{F}\ell$ make it very difficult to apply the quantitative formula of WAL/WL meaningfully, particularly as the underlying theory is based on the assumption that $k_F\ell >> 1$. However, the qualitative features of the MR (growing magnitude and increasing “cuspiness” near zero field as $T \rightarrow 0$) suggest that the MR mechanism is analogous to weak localization. To support this, we also present the film sample MR data plotted instead as magnetoconductance, in units of e^2/h (see Fig. 3.6). The maximum magnitude change of conductance over the ± 9 T field range is $\sim$ 1.9 e^2/h (sample HP1704, field in plane), $\sim$ 2.5 e^2/h (HP1704, field out of plane), or $\sim$ 0.28 e^2/h (sample HP1706, field out of plane), values which are of the typical magnitude of WL/WAL. Also, the similar high-field MR for in-plane and out-of-plane field orientations imply that the system is effectively in or close to the 3d limit, with a coherence length comparable to film thickness. These observations show the need for treatments of quantum corrections to conduction applicable to such bad metals.

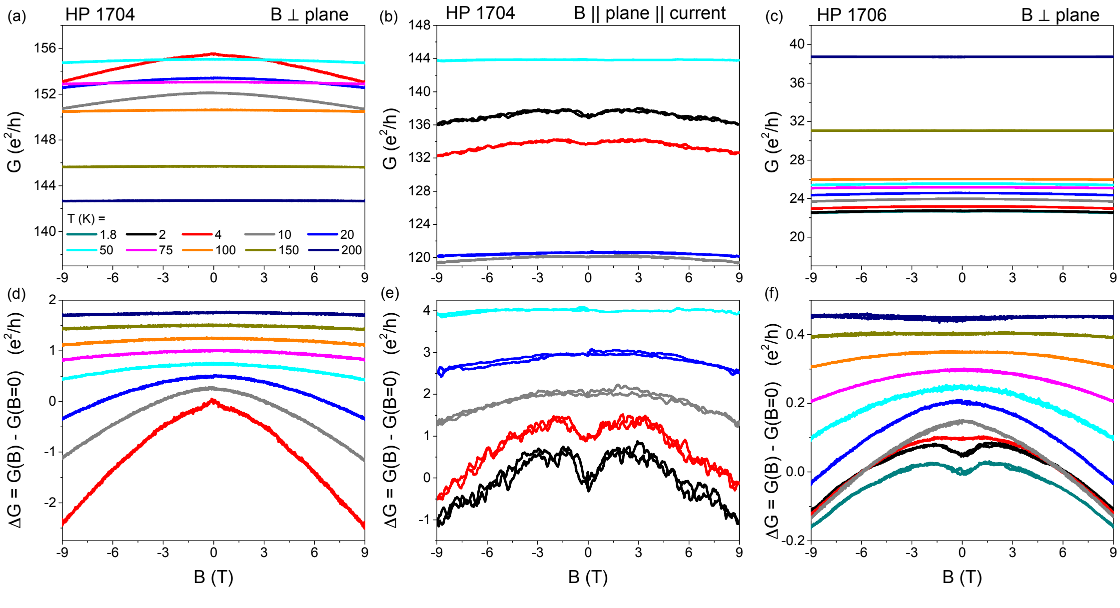

Figure 3.6: Magnetoconductance for film sample HP1704 with the field (a,d) perpendicular or (b,e) parallel to the plane of the substrate, and (c,f) film sample HP1706 with the field perpendicular to the plane of the substrate. The top row shows plots in units of raw conductance, and the bottom row shows the difference $\Delta G = G(B) - G(B = 0)$. Curves in the bottom row have been offset for clarity by (d) 0.25, (e) 1, and (f) 0.05. Figure reproduced from [8].

We note that an isotropic negative magnetoresistance quantitatively similar in magnitude and field scale to these observations has been reported previously[83] in few-unit-cell-thick films of the correlated material $LaNiO_3$. In that system this effect was interpreted as evidence for the importance of magnetic fluctuations[90] acting as a source of inelastic scattering, and possible proximity to a spin glass state[91] or antiferromagnetic ordering. While the partially filled vanadium $3d$ band could in principle be relevant for magnetism in H_xVO_2, measurements to date have found no evidence of magnetic ordering[64].

Given the substantial change in the shape of the resistivity versus temperature curve for successive cooldowns of the HP1704 film sample, and the larger resistivity of sample HP1706 after doping with nominally the same hydrogenation protocol as for HP1704, it is worth considering whether the presence of either a dip or peak in the low-field MR is a consequence of both the hydrogen doping fraction and the redistribution of hydrogen within the lattice over time, rather than an intrinsic anisotropic response of the material. The absence of anisotropy is further supported by measurements on nanobeam and micron-scale flake samples, as we describe in a subsequent section.

I also performed Hall measurements on the hydrogenated 10 nm thickness VO_2 films. In the metallic state of pristine VO_2 single crystals[73] and thin films[74, 92], the sign of the Hall coefficient indicates the dominance of n-type carriers. Interpreting the Hall data in terms of a single carrier type leads to the conclusion that there are several mobile carriers per vanadium ion. This has resulted in the suggestion that both n- and p-type carriers are present in the system, leading to a comparatively small Hall number[73, 74]. In both our as-grown and hydrogenated films, we observe a very small Hall signal at room temperature (Fig. 3.4e, hydrogenated film data) with a negative slope, consistent with a dominant contribution of n-type carriers. For the hydrogenated films, the Hall voltage becomes larger as the temperature decreases, which conventionally implies a decrease in carrier density. Linear fits are performed to obtain the slope of the Hall data.

Assuming only n-type carriers, we are able to deduce the Hall carrier density n and mobility μ from the Hall measurements and the resistivity, according to the equations: $n = IB/(V_{\mathrm{H}}ed)$, $\mu = 1/en\rho$, where I is the current, B is the perpendicular magnetic field, V_{H} is the Hall voltage, d is the thickness of the sample, and ρ is the resistivity. The temperature dependence of the deduced n and μ is presented in Fig. 3.4f. The extremely small Hall voltage leads to an extraordinarily high calculated carrier density, further resulting in an extremely small calculated value of mobility. At room temperature, the deduced n for the 10 nm film sample HP1704 is about 45×10^{28} m^{-3}, much larger than the density of vanadium atoms ($\sim 3 \times 10^{28}$ m^{-3}). Even at 2 K, where n reaches the minimum in the limit of our measurement setup, the inferred value is still as large as 1.9×10^{28} m^{-3}.

All these results further support the conjecture originating in the pristine VO_2 literature that the assumption of a single carrier type is incorrect; thus both n- and p-type carriers are likely present in this system, with comparable contributions to the conductance. While a two-carrier interpretation has been long been suggested to explain the small Hall number (and therefore large inferred carrier density) in metallic VO_2,[86] there remains no direct evidence for this, or an explicit electronic structure treatment that clearly identifies a possible source of hole carriers. This aspect of the band structure (*e.g.*, the source of the small Hall number; any hole-like source of carriers that could contribute) of doped (or even pristine metallic) VO_2 remains unresolved.

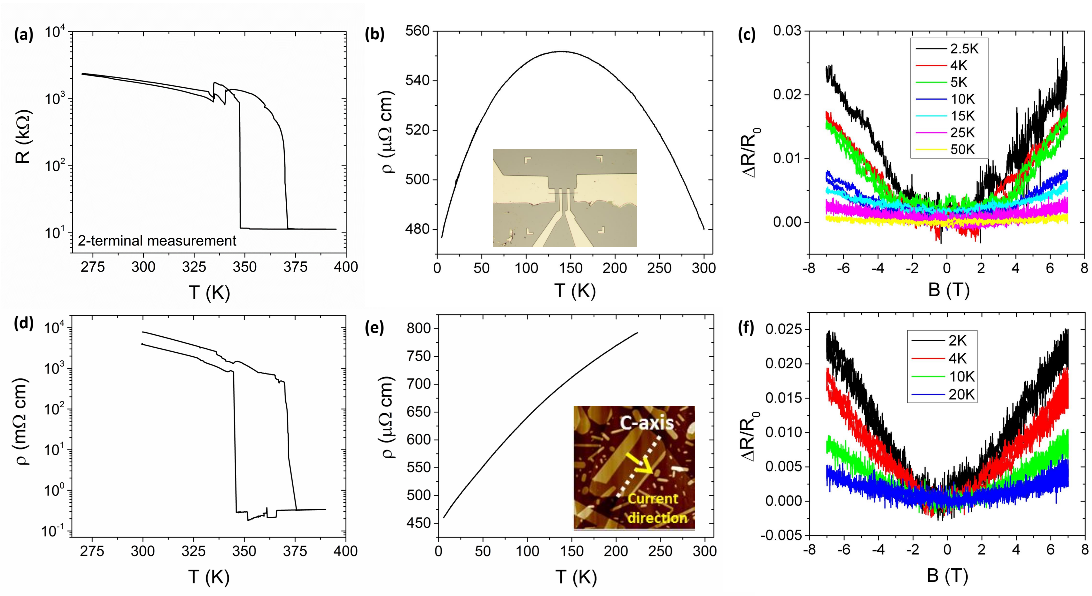

Figure 3.7: Top row: Temperature dependence of the resistance of a VO_2 nanobeam sample (a) before and (b) temperature dependence of resistivity after hydrogenation. The inset of (b) is a photo of the measured nanobeam test structure, taken under an optical microscope. (c) Positive MR response of hydrogenated VO_2 nanobeam sample at various temperatures with the field perpendicular to the substrate plane. Bottom row: Temperature dependence of resistivity of a VO_2 micron-size flake like sample (d) before and (e) after hydrogenation, with the inset of (e) showing the atomic force microscopy (AFM) image of the flake sample measured. Panel (f) shows its MR responses at various temperatures with the field perpendicular to the substrate plane. Figure reproduced from [8].

3.3.2 VO_2 nanobeams

As a comparison, the temperature dependence of resistance and the magnetoresistance of hydrogenated VO_2 nanobeams were also measured by H. Ji under comparable temperature and field conditions. The resistance of a representative sample shows a non-monotonic temperature dependence (Fig. 3.7(b)). The resistance gradually increases as the temperature decreases from 300 K to 140 K, at which point it reaches a maximum, though the total change is less than 20% and is thus quite different from the temperature dependence of resistance of a semiconductor. Below 140 K, the resistance decreases with cooling, similar to the behavior of a metal. Based on the temperature dependence of resistance measurement of the pristine sample, this transferred nanobeam should be rutile under c-axis tensile strain, which is due to direct contact with the substrate. When grown at high temperatures, the undoped nanobeams and flakes are initially in the rutile state, and are strongly elastically coupled to the underlying SiO_2 layer. After cooling to room temperature, the nanobeams transition into the monoclinic state (with its differing lattice parameters), yet remain firmly mechanically clamped by the underlying SiO_2, and thus become compressively strained along the rutile c-direction due to differences in thermal expansion. Nanobeams transferred onto a non-growth substrate are then in a comparatively unstrained state when they are in the monoclinic insulating phase, but they tend to be adhered to the substrate by van der Waals forces; when they transition to the metallic phase (either by heating or hydrogen doping), they will be under tensile strain. This is in contrast to the case of a VO_2 film grown on a TiO_2 substrate, which has a much stronger rutile c-axis compressive epitaxial strain due to the lattice mismatch[78].

The magnetoresistance of the VO_2 nanobeam shown in Fig. 3.7(c) has a positive high-field MR response below ~ 25 K, similar to the films, but without evidence of a low-field peak or dip feature at the lowest temperatures. Since the width and thickness of the nanobeam are both more than 50 nm, and the MR measurement with the magnetic field parallel to the current indeed shows the same rough magnitude of change as the perpendicular case (see Fig. 3.8), it seems reasonable to conclude that this system is also effectively 3d from the perspective of localization corrections. The appearance of positive MR at low temperature here and in the films suggests the possibility of weak anti-localization, and implies that vanadium may possess strong enough spin-orbit scattering to observe WAL. This is not entirely surprising, considering that some positive weak anti-localization MR is observed in copper films[67] whose atomic number ($Z = 29$) is only slightly larger than that of vanadium ($Z = 23$). As in the films, the MIRL resistivity here precludes a self-consistent quantitative analysis of the MR in terms of WL/WAL.

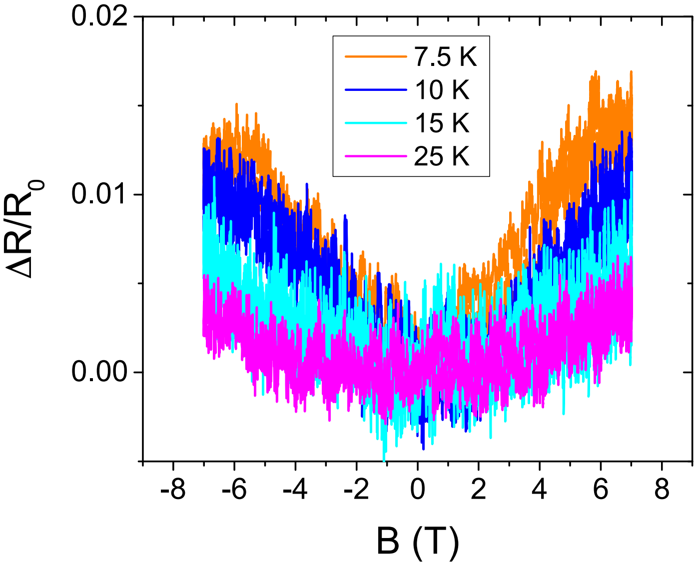

Figure 3.8: Positive MR response at various temperatures of the same hydrogenated VO$_2$ nanobeam sample as in Fig. 3.7(a-c), with the magnetic field oriented in the plane of the substrate and parallel to the current. The MR shape and magnitude are similar to what was observed in the field-perpendicular-to-plane orientation at comparable temperatures. Figure reproduced from [8].

Even though the positive MR of both VO$_2$ films and nanobeams may be interpreted as a consequence of weak anti-localization, the reason for the differences in the low-field MR response of the two sample types remains unclear. Beyond the question of the exact hydrogen concentration, there are two significant differences between these kinds of samples: strain direction and current direction with respect to the c_{R}-axis. The difference of strain directions has been mentioned above, and is clearly important based on the fact that the phase transition temperature in the undoped samples shifts to opposite directions in these two morphologies. It is long established that strain can modify the spin-orbit coupling[93]; in principle a strain-induced modification of the band structure and inversion symmetry could explain a sign flip in weak (anti)localization MR if the resulting SOC is sufficient. An example of strain modifying SOC and in turn the MR is Habib et al.[94], where SOC is explicitly tuned in GaAs 2d holes as a function of strain. Without a detailed electronic structure calculation, however, that explains, *e.g.*, the small Hall number in undoped metallic VO_2 and the electronic structure of the hydrogen-stabilized phase, or further spin-sensitive experiments, it is difficult to draw firm conclusions about the interplay of strain and SOC in this system.

The current direction may also be important if the hydrogenated VO_2 has anisotropic electronic properties. The physical structure (one-dimensional V chains in the undoped rutile structure) and highly anisotropic H diffusion properties clearly show that the c_R-axis is a special direction in VO_2; it is the direction along which dimerization of the V occurs in the insulating state of VO_2. For films, the current is in-plane, and the c_R-axis is perpendicular to the plane, therefore, the current is perpendicular to the c_R-axis. In nanobeams, however, the current is by necessity parallel to the c_R-axis. To investigate the possible existence of anisotropy, we turn to measurements of VO_2 flake-like single-crystal samples, also performed by H. Ji.

3.3.3 VO_2 microflakes

The c_R-axis of the VO_2 micro flakes can be determined by optical microscopy, because the domains formed during the phase transition in the undoped material are always in a stripe shape perpendicular to the c_R-axis, and are visible through their optical contrast. Generally, the c_R-axis is along the long side of rectangular VO_2 flakes. Here, four V/Au contacts were deposited by H. Ji along the short side of the flake, so that the current would be perpendicular to the c_R-axis (inset of Fig. 3.7(e)), as in the film measurements, and in contrast to the nanobeam measurements. Although the VO_2 flakes remain on their growth substrate, and thus are expected to have larger strain than transferred VO_2 nanobeams, the hydrogenated flake sample shows a monotonic positive temperature-dependent resistivity (Fig. 3.7(e)), similar to a metal.

The MR measurements of the flake sample show a positive response that grows with decreasing temperature (Fig. 3.7 (f)), just as for the nanobeam case. Since the current direction is now perpendicular to the c_{R}-axis, this essentially rules out the possibility that the different MR response of the films and the single-crystal wires/flakes (the low-field peak or dip features seen in the films) is caused by intrinsic anisotropy.

3.3.4 Mesoscopic conductance fluctuations

We also study submicron-size hydrogenated VO_2 test structures, consisting of both an epitaxial film sample and a nanobeam sample. On the film, H. Ji used e-beam lithography and e-beam evaporation to define and deposit multiple contacts with spacings between voltage probes varying from 500 nm to 8 μm, followed by e-beam lithography and reactive-ion etching (RIE) to pattern and etch away the unwanted VO_2 between the gold contacts except for a strip about 10 μm wide in the middle (Fig. 3.9(a)). The cracked 30 nm thin film is used for these measurements, though the length scales between the metal contacts are sufficiently small that the cracks are not expected to affect the transport. Qualitatively similar results are obtained on nanobeam samples as well. For the nanobeam samples, Ji and I used a self-aligned technique to deposit gold contacts (deposition of one contact at normal incidence, and the other at a 45° angle), forming a gap size on the order of 100 nm (Fig. 3.9(b)). All these samples are hydrogenated using the same process described above, and transport measurements are done in the PPMS. Although the magnitude of resistivity and its temperature dependence show behavior similar to that of the large-scale samples, the MR is quite different. In both film and wire samples with submicron

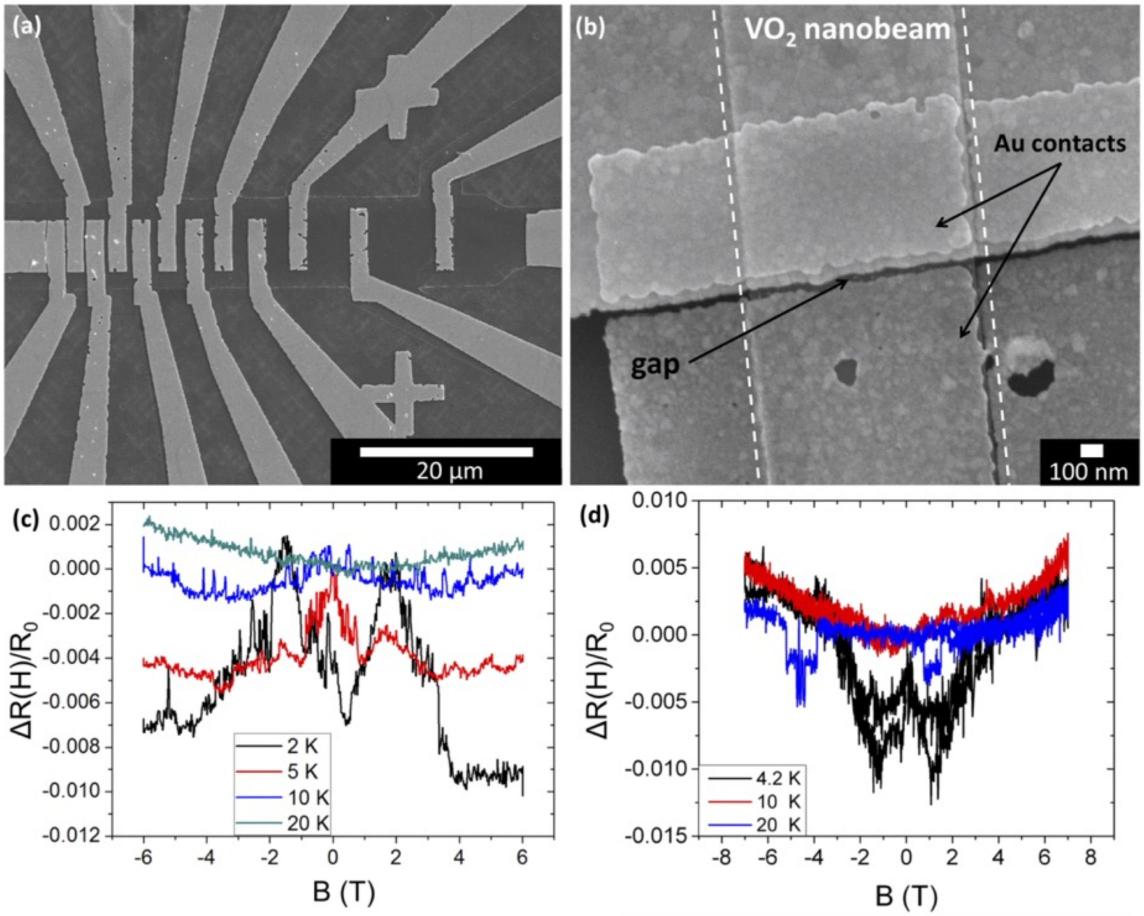

Figure 3.9: (a) SEM image of a patterned and etched VO_2 film sample, with spacings between the gold contacts ranging from 300 nm to 8 μm. (b) SEM image of a VO_2 nanobeam sample patterned by a self-aligned technique, with a gap size of about 20 nm. (c) MR response of the hydrogenated VO_2 film with a contact spacing of about 400 nm. (d) MR response of the hydrogenated VO_2 nanobeam nano-gap sample. Both samples show apparently random, but retraceable MR fluctuations, consistent with UCF physics. Figure reproduced from [8].

voltage probe separations, the MR varies nonmonotonically in an apparently random manner (Fig. 3.9, panels (c) and (d)), with some signs of telegraph noise. The randomness, however, still follows certain rules: the curves retrace themselves with increasing or decreasing magnetic field; are approximately symmetric (to within the effects of telegraph switching) about zero field; and the lower the temperature, the larger the fluctuations. For a given sample, after warming up to room temperature and cooling down again, the pattern of MR changes. All these features suggest that the fluctuations are likely a form of universal conductance fluctuation (UCF)[68]. The large field scale associated with the observed fluctuations is consistent with the short coherence length on the order of ∼10 nm implied by 3d WLMR. If the MR fluctuations are interpreted in terms of a fluctuating parallel conductance, the change of conductance is less than 1 G_0 ($2e^2/h \sim 7.748\times10^{-5}$ S), consistent with expectations of UCF, which is suppressed with increasing sample size through ensemble averaging. The large field scale precluded detailed studies of the conductance fluctuations (*e.g.*, autocorrelation of the conductance, G, as a function of magnetic field).

3.4 Conclusions

In this work, we studied the low temperature transport properties of hydrogenated VO_2 of different morphologies that were grown by distinct methods. The large resistivity of these samples apparently violates the Mott-Ioffe-Regel limit over the full temperature range examined, implying the failure of simple semiclassical transport for this doping-stabilized metallic state of H_xVO_2. VO_2 films grown by MBE on TiO_2 (001) substrates show a positive high-field MR when $T < 150$ K independent of field direction. The detailed low-field MR structure shows either a dip or peak at low temperatures, with the sign likely determined by a combination of strain effects and the hydrogen doping level and uniformity. Analogous MR measurements of VO_2 nanobeams and micron-scale flake-like crystals grown by PVD on Si/SiO_2 substrates show a high-field positive response similar to that of the films, but with a low-field response that is featureless (no sharp peak or dip) to within the noise background. This positive overall MR resembles a quantum interference correction to conduction like WAL/WL. Quantitative analysis of the MR, however, is complicated by poor understanding of the electronic structure of the bad metal state and a lack of a self-consistent theoretical framework for analyzing such quantum interference effects in MIRL-violating materials. Hall measurements on the film material confirm a very small Hall number, both in the pristine room-temperature metallic state and in the hydrogen-stabilized metallic state. Finally, magnetoresistance measurements on sub-micron scales show evidence for mesoscopic conductance fluctuations with a field scale consistent with a short ($\sim$ 10 nm) coherence length.

These observations demonstrate that mesoscopic corrections to electronic conduction can be present even in materials that apparently violate the Mott-Ioffe-Regel limit, and hence should conventionally be expected to be crossing into the strongly localized regime. Our experiments highlight the need for a better understanding of the electronic properties of metallic VO_2 (undoped or stabilized by hydrogen doping), and the importance of developing treatments of mesoscopic effects in systems where the conventional, long-useful, semiclassical picture is not appropriate.

Chapter 4

Potential Fluctuations at Low Temperatures in Mesoscopic-Scale $SmTiO_3/SrTiO_3/SmTiO_3$ Quantum Well Structures

---

Part of this chapter is adapted from the published work [12] :

Potential Fluctuations at Low Temperatures in Mesoscopic-Scale $SmTiO_3/SrTiO_3/SmTiO_3$ Quantum Well Structures

Will J. Hardy, Brandon Isaac, Patrick Marshall, Evgeny Mikheev, Panpan Zhou, Susanne Stemmer, and Douglas Natelson

ACS Nano, in press

DOI: 10.1021/acsnano.6b08427

In Chapter 3, we considered a long-studied prototypical SCM, VO_2, and we now turn to a more recently developed topic in correlated oxide materials: The conducting interface that can form between certain insulating transition metal oxides with the perovskite structure and composition ABO_3 (A = rare earth, B = trivalent transition metal). As will be described below, such systems have opened new avenues of inquiry, which are of special interest in light of the possibility of engineering exotic behaviors through advanced growth techniques, which are now capable of single-atomic-layer precision.

4.1 Introduction

Interest in oxide-based heterostructures has intensified in recent years, in large part due to advances in epitaxial film growth and the 2004 discovery by Ohtomo and Hwang of a two-dimensional conductive interface (a high carrier density two-dimensional

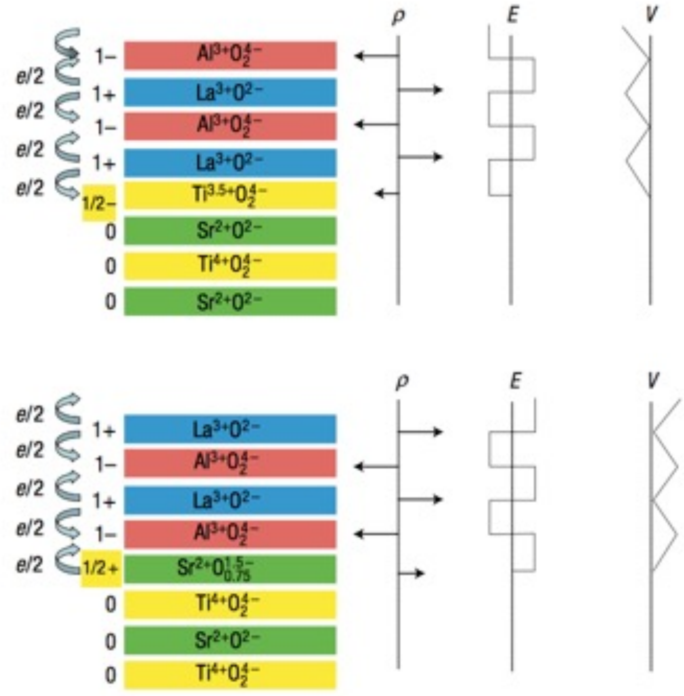

Figure 4.1: **Polar discontinuity at LAO/STO interfaces.** LAO has planes of alternating +1 and -1 net charge, while STO is neutral. To resolve this polar discontinuity, and depending on which material layers touch at the interface, redistribution of electron density occurs as shown either as (upper panel) AlO_2/LaO/TiO_2 with half an electron per unit cell transferred from LAO to STO, or (lower panel) AlO_2/SrO/TiO_2 with half an electron transferred from STO to LAO. The line diagrams on the right show the charge density ρ, electric field E, and potential V. After reconstruction, the electric field alternates about zero, and the potential no longer diverges. Figure reproduced with permission from [9]. © 2006 Macmillan Publishers Ltd.

electron gas, 2DEG) between the insulating perovskite materials $LaAlO_3$ (LAO) and $SrTiO_3$ (STO) [95, 10]. There, the difference in electron density of the two sides (when polar and nonpolar oxides are interfaced) results in the "polar catastrophe," in which a built-in electric field exists at the interface. This situation is depicted in Fig. 4.1. In response to this, either the crystal structure at the interface can reconstruct (in which case, no 2DEG forms), or the electron density can be redistributed to compensate, with charge accumulating at the interface to form the confined 2DEG.[9] The electronic properties of this electron gas are determined by a combination of lattice distortions, spin-orbit coupling, defects, and various regimes of magnetic, charge, and orbital ordering. Strong electronic correlations result from this situation, resulting in competing orders that can be tuned by various external parameters (*e.g.*, temperature, magnetic field, pressure, chemical doping, and electrostatic gating)[96, 97, 98, 99, 100, 101]. Nonstoichiometry at the interface can complicate matters considerably.

Techniques for growing high-quality films and atomically sharp interfaces of these transition metal oxides (TMOs) and their characterization are central to many ongoing research efforts [102]. The possibility for rich interplay between charge, spin, and orbital ordering (depicted schematically by Hwang *et al.* in the diagram of Fig. 4.2) makes oxide heterostructure systems excellent tools in the study of correlation phenomena with wide-ranging implications, from understanding high-T_C superconductivity [36] to engineering materials with novel functional properties [103, 104, 105, 106]. Many aspects of these and related oxide heterostructures remain, however, only partially understood, including the nature of quantum coherence in transport, and the relationship of coherence with other effects such as spin-orbit coupling, localization (both weak and strong), and charge and magnetic ordering.

Here, we examine electronic transport in mesoscale devices made with heterostruc-

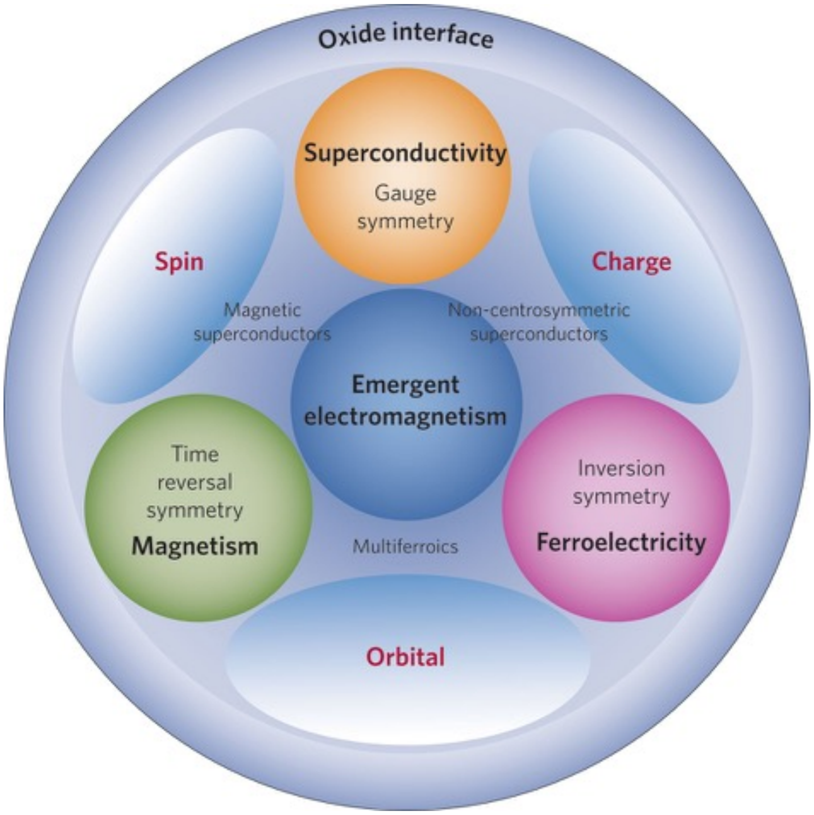

Figure 4.2: **Rich interplay of phenomena at oxide interfaces.** These systems display intriguing and potentially useful competitions in their electronic and magnetic properties, driven by the underlying symmetries and degrees of freedom depicted here. Figure reproduced with permission from [10]. © 2012 Macmillan Publishers Ltd.

tures of $SrTiO_3$ sandwiched between layers of $SmTiO_3$. Motivating the present study is a body of prior work focused on quantum wells (QWs) in epitaxial STO layers sandwiched between layers of either antiferromagnetic (AFM) $SmTiO_3$ (SmTO) or ferrimagnetic $GdTiO_3$ (GdTO). Those studies, performed using structures with lateral dimensions of 100 μm^2 to 1 cm^2, [101, 107, 11, 108] demonstrated that the transport properties of the SmTO/STO QWs can be tuned from a regime of seemingly Fermi liquid (FL) behavior to a non-Fermi liquid (NFL) regime as the STO thickness is reduced below a critical value of 5 SrO layers, as inferred from the temperature dependence of the resistance. Fitting with the functional form $\rho = \rho_0 + A\ T^{\ n}$, a fitting exponent $n < 2$ is interpreted as NFL behavior (in this case, the present NFL samples exhibit $n \sim\ 5/3$ over a fairly broad temperature range). Using these results, a phase diagram for SmTO/STO/SmTO QWs can be constructed, as shown in Fig. 4.3. Subsequent work [109] focused on tunneling spectroscopy in these QW samples, uncovering spectroscopic evidence of a pseudogap at low temperatures in AFM-confined QWs, as well as evidence of coherent transport in these structures.

In this chapter, we expand upon those measurements to examine transport in structures of mesoscopic size. We find unexpected, time-dependent voltage fluctuations that emerge at low temperatures for devices of small contact electrode size ($\sim$ 250 nm width). These fluctuations were detected between voltage probes in measurements of temperature-dependent resistivity and as a correction to the field-perpendicular-to-plane magnetoresistance (MR). Remarkably, the voltage fluctuations are independent of measurement current, ruling out conventional temporal universal conductance fluctuations (UCF) as a mechanism, and are systematically suppressed with increasing contact spatial size and increasing temperature. The suppression on larger temperature and spatial scales implies that the fluctuations are mesoscopic in nature. We propose a possible origin of the observed behavior in terms

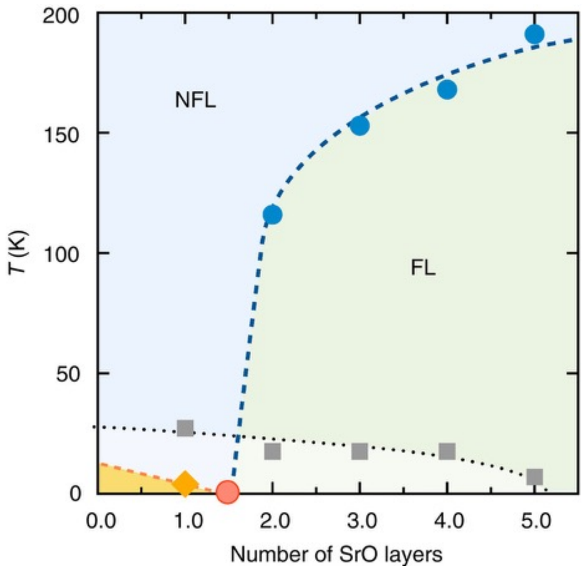

Figure 4.3: **Phase diagram of SmTO/STO/SmTO quantum wells** The quantum well thickness, in terms of number of SrO layers, determines the details of crossover between FL and NFL behavior. Blue circles are points determined from the fitting of temperature dependent resistivity data, and gray squares mark the temperature of resistivity upturn, below which the data are not included for fitting. The red circle marks a possible quantum critical point. Figure reproduced with permission from [11]. © 2014 Macmillan Publishers Ltd.

of a time-varying Seebeck coefficient within this system. An improved understanding of charge transport in model systems such as this one, especially any quantum coherent properties, may lead to new insights into the nature of transport in strongly correlated materials that deviate from Fermi liquid theory.

4.2 Methods

The SmTO/STO/SmTO heterostructures used in these studies were grown by Brandon Isaac under the guidance of Prof. Susanne Stemmer at the University of California, Santa Barbara (UCSB), using the technique of hybrid molecular beam epitaxy (MBE) on LSAT substrates as described elsewhere [101, 11, 110] Based on prior transport results [108], the STO layer thickness (given in number of SrO layers) was chosen to yield one nominally NFL sample (4 SrO layers) and one nominally FL sample (10 SrO layers) for comparison. The STO layer thickness was verified by the UCSB team using cross-sectional scanning transmission electron microscopy (STEM). An example of a STEM image of a similar QW sample used in a previous work is shown in Fig. 4.4, demonstrating the excellent crystallinity and atomic sharpness of the MBE-grown layers. Initial resistivity and Hall measurements were also performed on the as-grown samples using shadow-masked Ti/Au contacts, before sample shipment to Rice.

Mesoscale devices for transport measurements (Hall bars and mesa samples) were fabricated from the as-grown QWs by a combination of e-beam and photolithography to define contacts for metallization (e-beam evaporation of 5 nm Ti and 50 nm Au), followed by room-temperature directional reactive ion etching (RIE) with chlorine (a process suggested by Dr. E. Mikheev) to isolate well-defined regions of QW sample for study. For the etching process, the metal contacts were protected with either 35 nm of Al_2O_3 deposited by e-beam evaporation (for samples with several small contacts

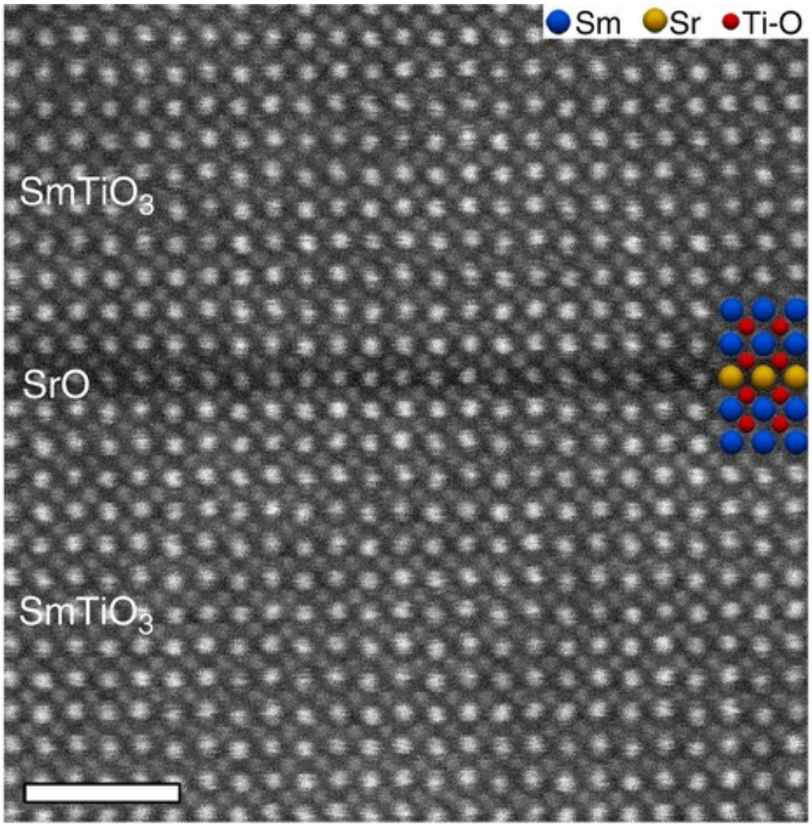

Figure 4.4: **Cross-sectional STEM image of a 1-SrO thick QW sample.** The heterostructures used in the work discussed in this chapter have thicker STO than shown in this image, increasing to either 4 or 10 SrO layers in thickness.The scale bar represents 2 nm. Figure reproduced with permission from [11]. © 2014 Macmillan Publishers Ltd.

at variable spacing) or Shipley S1813 photoresist (for larger Hall bar samples).

Transport measurements were performed using low-frequency lock-in techniques in a Quantum Design Physical Property Measurement System (PPMS). After processing the as-grown samples into test structures, temperature-dependent resistance and variable-temperature Hall measurements were performed at Rice and their results compared to those obtained in advance with the unprocessed films (which were measured in Van der Pauw geometry by B. Isaac), to ensure that the QW properties had not changed over time during the device fabrication. Since the QW samples are known to degrade when baked at high temperatures in ambient atmosphere (as noted by the UCSB team), all processing was limited to temperatures below 120°C, and no evidence of degradation was observed when comparing transport data taken before and after processing.

4.3 Results

Brandon Isaac first performed van der Pauw measurements to characterize the as-grown samples (see Fig. 4.5). He determined that the sheet resistance at 2 K is $\sim$ 135 Ω/square (FL sample) or $\sim$ 345 Ω/square (NFL sample). At 2 K, the FL sample has an apparent carrier density (estimated from Hall measurements) of $\sim$ 3.2 $\times 10^{14}$ /cm^2 and a mobility of $\sim$ 140 cm^2/V s; by comparison, at 2 K the NFL sample has a carrier density of $\sim$ 9.4 $\times$ 10^{14}/cm^2 and an inferred mobility of 19 cm^2/V s. Prior work [108] has noted that the apparent carrier density values inferred from Hall measurements (and subsequently inferred carrier mobility) in these structures are not strictly accurate at low temperatures due to the phenomenon of lifetime separation, which entails different scattering rates governing longitudinal transport and Hall resistances. Thus, it is more accurate to label these measurements as $(eRH)^{-1}$ rather than carrier density.

The as-grown samples were shipped to Rice, where I then processed them into meso- and nanoscale devices as described in the Methods. Briefly, the as-grown QW films were patterned into micron-scale test structures with several Ti/Au metal contacts, in two geometries: a Hall bar with lateral dimensions of $\gtrsim$ 10 μm, and a long mesa (3.5 μm wide and $\sim$ 200 μm long) of QW material with multiple narrow contacts (either nominally all $\sim$ 250 nm width, or in a range of widths from $\sim$ 0.2 – 5 μm) along its length at variable spacing intervals ($\sim$ 0.1 – 3 μm contact separations), as well as large current contacts located at the mesa ends in the long direction. Top view images of representative devices of each type are shown in Fig.

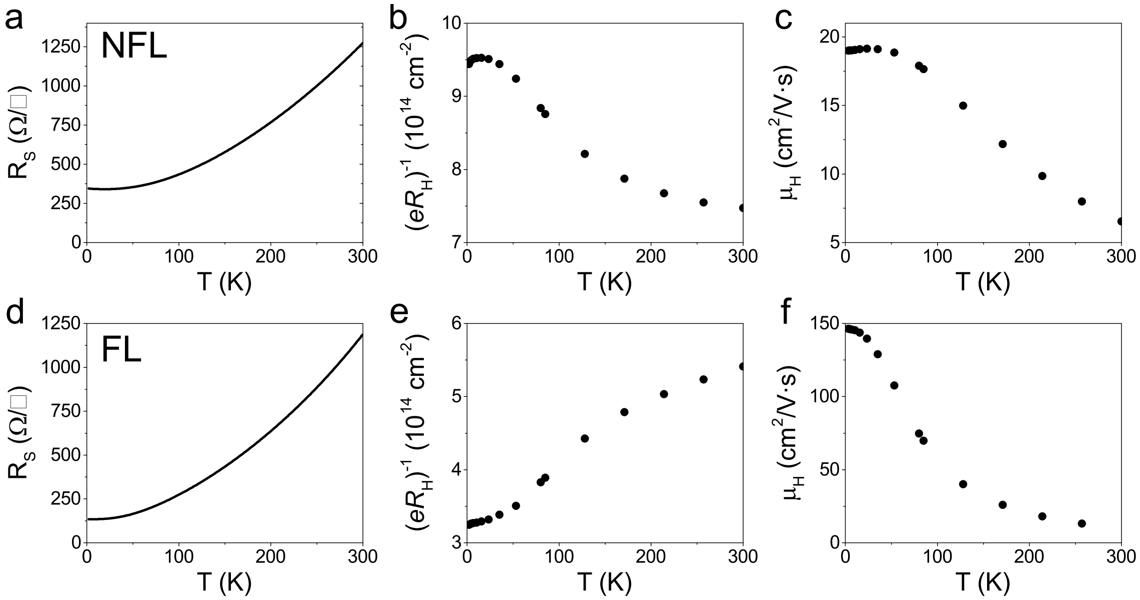

Figure 4.5: **Transport characterization of as-grown samples** Initial characterization of the as-grown NFL sample (top row, a-c) and FL sample (bottom row,d-f) (each of lateral dimensions 1 cm^2) in van der Pauw configuration showing temperature dependence of sheet resistance (a,d), apparent carrier density $(eRH)^{-1}$ (b,e) and mobility (c,f) inferred from Hall and resistivity measurements. As discussed in the main text, the apparent carrier density (and inferred mobility) values obtained from Hall measurements are not accurate at low temperatures due to the phenomenon of lifetime separation. Figure reproduced from [12].

4.6, along with a cross-section diagram of the QW stack. These structures were used to measure temperature-dependent resistance (circuit schematic shown in Fig. 4.7), MR isotherms, and time-dependent isotherms to assess low-temperature fluctuations initially observed in the resistance, but later found to be pure voltage fluctuations independent of measurement current.

The temperature dependent resistance (shown in Fig. 4.8 (a-d) has a positive slope at high temperatures for both FL and NFL samples, consistent with metallicity, followed by a small low-T upturn that appears at around 20 K upon cooling. For both FL and NFL samples, the resistance is measured in a four-terminal configuration with two large current leads and two small voltage probe electrodes ($\sim$ 250 nm wide, as in Fig. 4.6b), with a constant ac current in the range 10 – 200 nA, sourced using a large series resistance (much larger than the two-terminal device resistance). Unexpected, greatly enhanced fluctuations of the inferred resistance were observed at low temperatures (below $\sim$ 20 K). They are clearly visible in the temperature dependent resistance plots (see Fig. 4.8(a-d)), with the fluctuations growing as the temperature is decreased below $\sim$ 20 K, despite the fact that the (average) magnitude of resistivity changes much less in this temperature range. Such fluctuations were not observed in the larger Hall bar type devices (of the style shown in Fig. 4.6a) to within the background noise level of the measurement, although in the Hall bar devices the overall shape of the $R(T)$ curves is in otherwise good agreement with what is measured using the small-contact samples.

This phenomenology is superficially reminiscent of time-dependent universal conductance fluctuations (TDUCF) [68, 111, 112, 113, 114, 115, 116, 117]. In TDUCF, fluctuating disorder alters the relative phases of coherently interfering electronic trajectories, leading to a time-varying mesoscopic correction to the resistance that is suppressed by ensemble averaging as temperature or length scales are increased. The

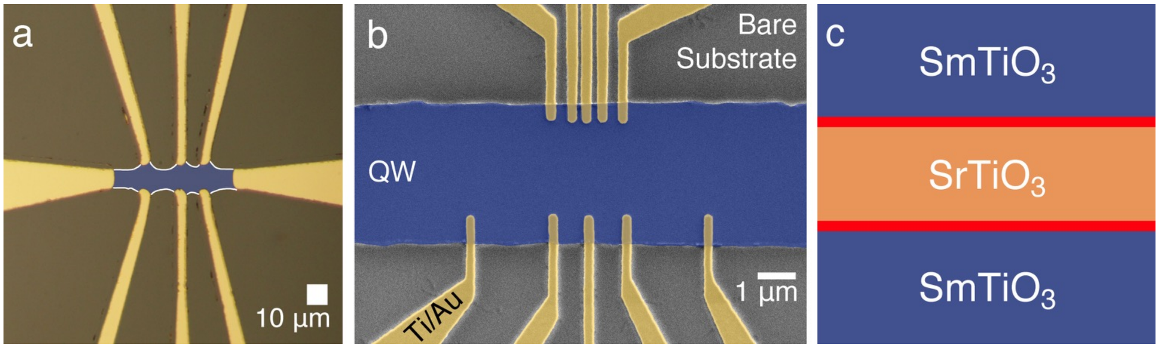

Figure 4.6: **Sample device layout.** Top-view images of (a) a Hall bar structure (optical image, QW area highlighted in blue) and (b) a narrow mesa-style sample with variable contact spacing (false-color SEM image; large current lead contacts, not shown, are located beyond the field of view at the left and right ends of the mesa). In both cases, the current flows along the horizontal direction through a mesa of QW structure isolated by etching. Voltage probes located along the QW mesa's edges are used to sense the potential drop. (c) Cross-sectional schematic view (not to scale) showing the structure of a SmTO/STO/SmTO layer stack. Red bars schematically represent the 2d electron gases that form at the SmTO/STO interfaces (though a fraction of the electrons in the d_{xz} and d_{yz} orbitals are delocalized throughout the depth of the well, and overlap of the gases can take place in thin wells) [13]. Figure reproduced from [12].

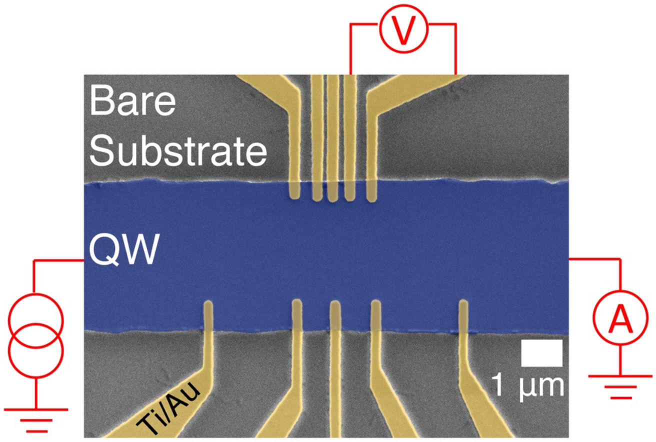

Figure 4.7: **Measurement schematic.** Circuit diagram showing the QW mesa structure wired up for a resistance measurement, with a current source connected on the left side, ammeter in series on the right side, and voltmeter connected in parallel via two narrow potential probe contacts at the top. The ammeter measures the longitudinal current, and the voltmeter measures the corresponding potential difference that develops in response to the applied current. Figure adapted from [12].

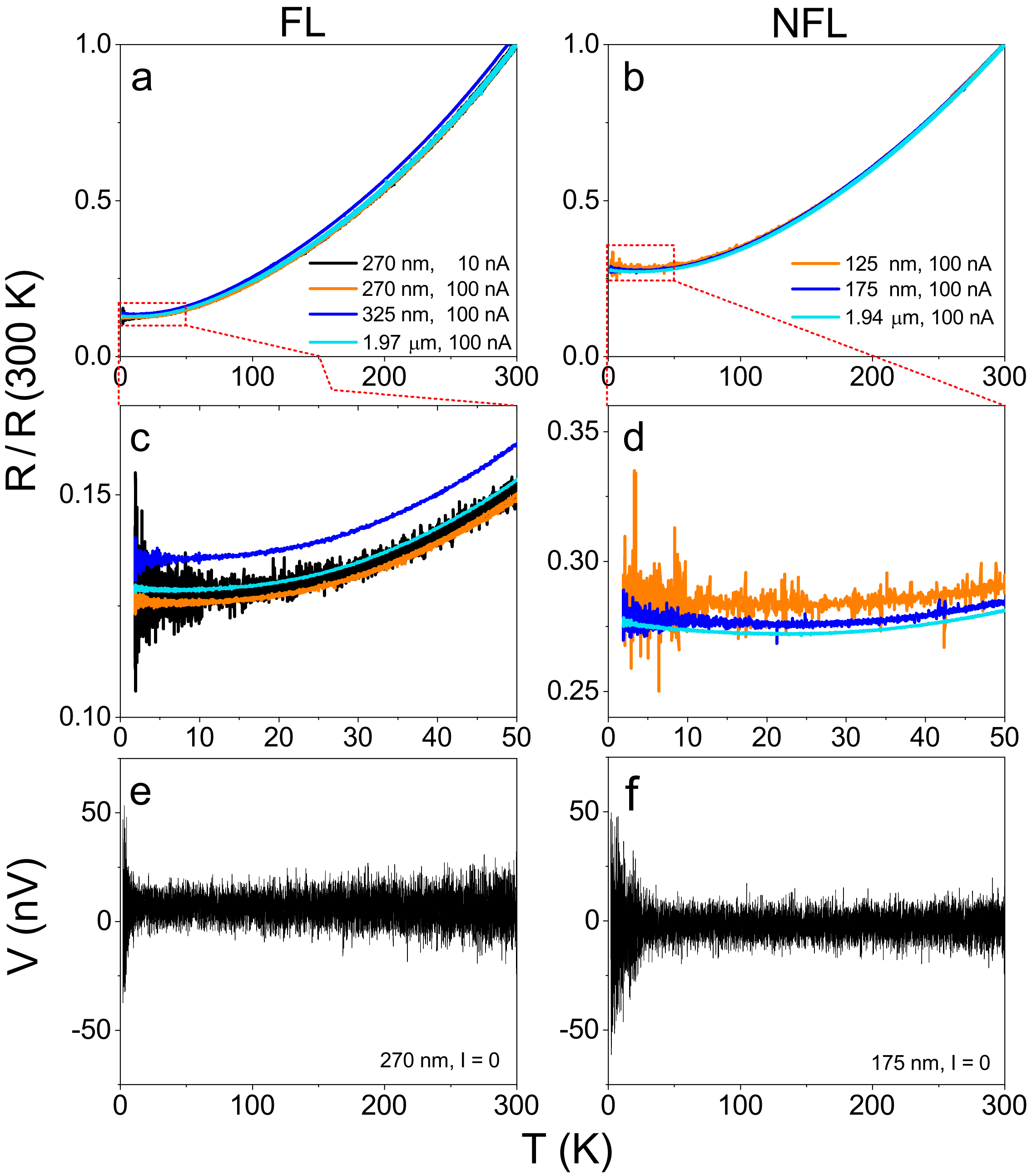

Figure 4.8: **Temperature dependence of resistance and voltage fluctuations without current.** Resistance (normalized to T = 300 K values) as a function of temperature for mesa-style samples of both FL (a,c) and NFL (b,d) type, with various separation distances between narrow voltage probe contacts and using various drive currents. Panels (c) and (d) show enlarged views of the region below 50 K, where enhanced fluctuations appear as the temperature is decreased below 20 K. Even when the drive current is zero (panels (e) and (f)), the measured potential between two narrow voltage probe electrodes (separated by 270 nm for FL or 175 nm for NFL) displays fluctuations that grow with decreasing temperatures, reaching several tens of nV in amplitude at T = 2 K. Figure reproduced from [12].

TDUCF typically have a $1/f$ frequency dependence of spectral power density, and since they are true resistance fluctuations, TDUCF voltage noise power scales with the square of the measurement current.

Several comparison measurements were made using small contacts separated by various distances, and with drive currents ranging from 10 – 200 nA. In contrast to the expectations for TDUCF, the voltage fluctuation magnitude is approximately the same for all measurements, while the inferred resistance fluctuation level appears to decrease with larger drive current or larger contact separation distance due to the larger measured voltage drop (i.e., the ratio of the voltage fluctuation size to the total voltage drop, δV/V, decreases). In contrast to the fluctuating potential, the simultaneously measured drive current and its fluctuation level are found to be stable under all measurement circumstances, with no appreciable change at low temperatures.

We further confirm the lack of dependence of the fluctuations on the drive current by measuring the voltage drop between two electrodes as a function of temperature, *in the absence of any drive current* (the current terminals are left electrically floated), as shown in Fig. 4.8(e,f). Just as for the resistance measurement, here the potential fluctuations increase dramatically at low temperatures for both FL and NFL samples, reaching several tens of nV.

We examined the voltage fluctuations in further detail using frequency domain measurements. [118, 119] We measured the amplitude of the potential difference between various pairs of electrodes, under zero applied current, as a function of frequency using a fast Fourier transform (FFT) spectrum analyzer, over a range of 0.5 – 25 Hz. For each measurement, 500 individual spectra were collected and averaged to reduce background noise contributions. As shown in the log-log plots of Fig. 4.9, the measured spectra have decreasing amplitude contributions at higher frequencies for both FL and NFL samples, following a rough $1/f$ relationship for most traces.

For small size contacts ($\sim$ 250 nm wide voltage probes), the measured amplitude was largest at low temperatures, decreasing by more than an order of magnitude at room temperature. By comparison, for large contacts (the current leads at the ends of the mesa, $\sim$ 3.5 μm wide), the fluctuation spectrum at 2 K was in reasonable agreement in magnitude with the 300 K data for small contacts, approximating the noise floor of our measurement system (see Fig. 4.15). A separate sample was also fabricated with voltage probe contacts of various widths, and similar frequency spectra were collected to compare the effects of increasing contact size (see Fig. 4.10).These trends indicate that the fluctuations are most prominent in contacts of small size, and the separation distance between the small contacts seems to have little effect on the voltage fluctuation amplitude at low temperatures, as shown in panels (b) and (c) of Fig. 3 for two pairs of narrow contacts on an NFL sample, separated by $> 10\times$ different distances.

To further constrain possible mechanisms behind these observations, we also consider the transport properties under application of an external magnetic field. MR curves were measured at selected temperatures for both NFL and FL samples, using both small and large voltage probe contacts separated by various distances in the range of $\sim$ 100 nm – 10 μm. For small voltage measurement contacts, and most prominently in the NFL case (also for FL samples, but to a lesser extent), the MR shape is overlaid with large time-varying fluctuations (due to the potential fluctuations), causing a mismatch between the portions of the curve sweeping up and down in field.

The NFL samples (Fig. 4.11, panels a-d) show a negative MR at low temperatures with a cusp at zero field. This curve shape flattens noticeably as the temperature is increased to 75 K, and becomes weakly positive by 100 K. The MR magnitude is less than 1% at 2 K and less than 0.1% at 100 K. In contrast, for the FL samples (Fig. 4.11, panels e-g), the MR is positive at all temperatures and is nearly linear at

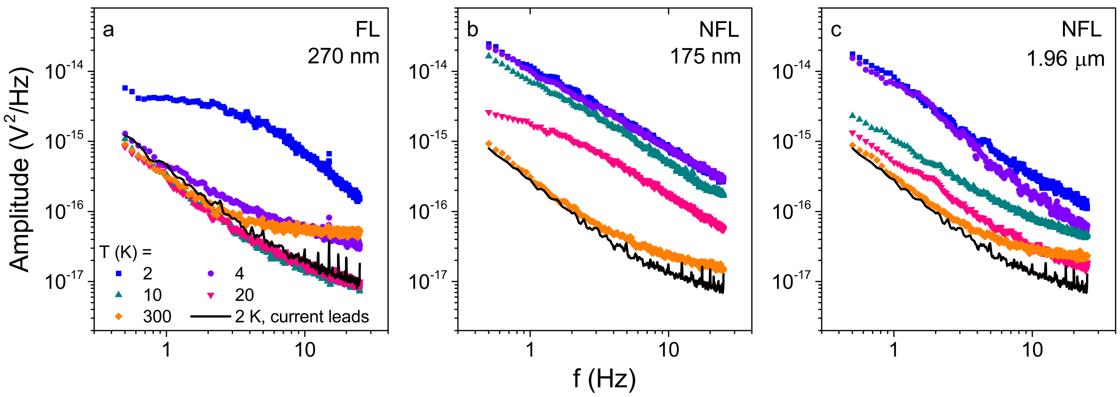

Figure 4.9: **FFT spectra of fluctuation amplitude at low frequencies and various temperatures.** Log-log plots of fluctuation amplitude (at zero drive current) as a function of frequency, collected using narrow ∼ 250 nm wide voltage probe contacts (solid points) on (a) FL sample with contact separation ∼ 270 nm, (b) NFL sample with contact separation ∼ 175 nm, and (c) NFL sample with contact separation ∼ 1.96 μm. For comparison, each plot also includes the spectrum collected using the large contacts at the two ends of the mesa at T = 2 K (black solid line). This trace is of the same magnitude as the room-temperature curves collected using small voltage probe contacts. Note that the spectral traces in solid points in (b) and (c) are similar in magnitude despite the > 10× difference in contact separation distance, which supports the idea that contact size is the most important factor in determining the fluctuation amplitude. Figure reproduced from [12].

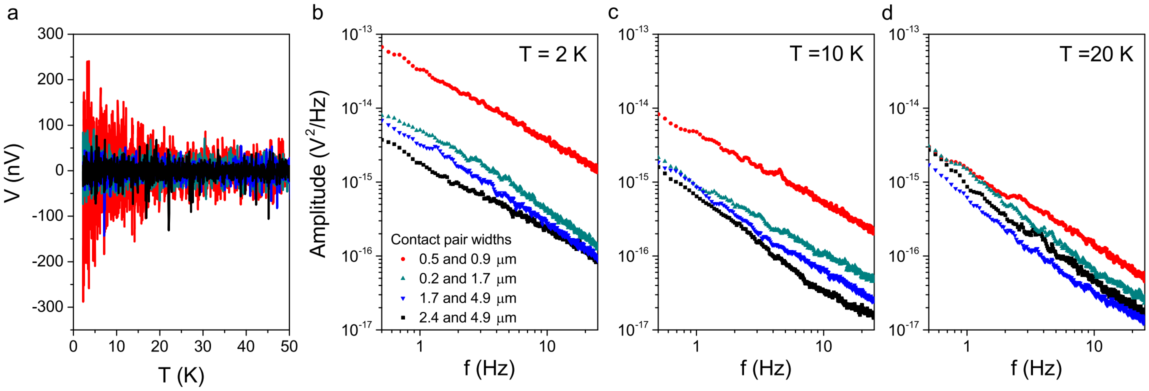

Figure 4.10: **Fluctuations measured with different contact sizes.** (a) Potential fluctuation measured as a function of temperature (with zero drive current) collected on a mesa-style FL sample using pairs of contacts of various widths. (b-d) Log-log plots of voltage fluctuation amplitude (at zero drive current) as a function of frequency for the same contact pairs as in (a). At 2 K, there is an enhancement of fluctuation amplitude with decreasing contact size, and as the temperature is increased, the overall fluctuation amplitude decreases for all contact pairs, and the curves for all contact pairs reach similar magnitudes. Figure reproduced from [12].

100 K, with magnitude $\sim 0.25\%$, increasing to $\sim 0.5\%$ by 2 K. As the temperature is decreased below $\sim$ 100 K, an approximately flat region appears at low magnetic fields that widens with decreasing temperature, with an upturn at a field scale of $\sim$ 3.7 T at T = 2 K (though the precise field value of the upturn is difficult to determine due to the fluctuations).

Even at relatively large currents (200 nA), under which conditions the temporal voltage fluctuations feature less prominently in the resistance (due to the larger average voltage drop compared to the roughly fixed fluctuation size at a given temperature), Fig. 4.12 shows that sweeping the field back and forth several times between $\pm$ 9 T produces a collection of MR curves that presumably should be identical, but differ with each other in their detailed structure (also see additional data in Figs. 4.13 and 4.14). We further note that there is little effect of an applied magnetic field of up to 9 Tesla on the magnitude of the time-dependent potential fluctuations for either FL or NFL samples. This, too, is inconsistent with the Feng-Lee-Stone TDUCF theory prediction of a relative reduction in noise by a factor of two when a sufficiently strong magnetic field is applied to a disordered conductor and time reversal symmetry is broken (where the required field strength is proportional to the inverse square of the phase coherence length L_ϕ). [114, 115, 116, 117, 120] These two behaviors are not in agreement with the typical observations of universal conductance fluctuations, and suggest the need for a better understanding of transport in these QW systems.

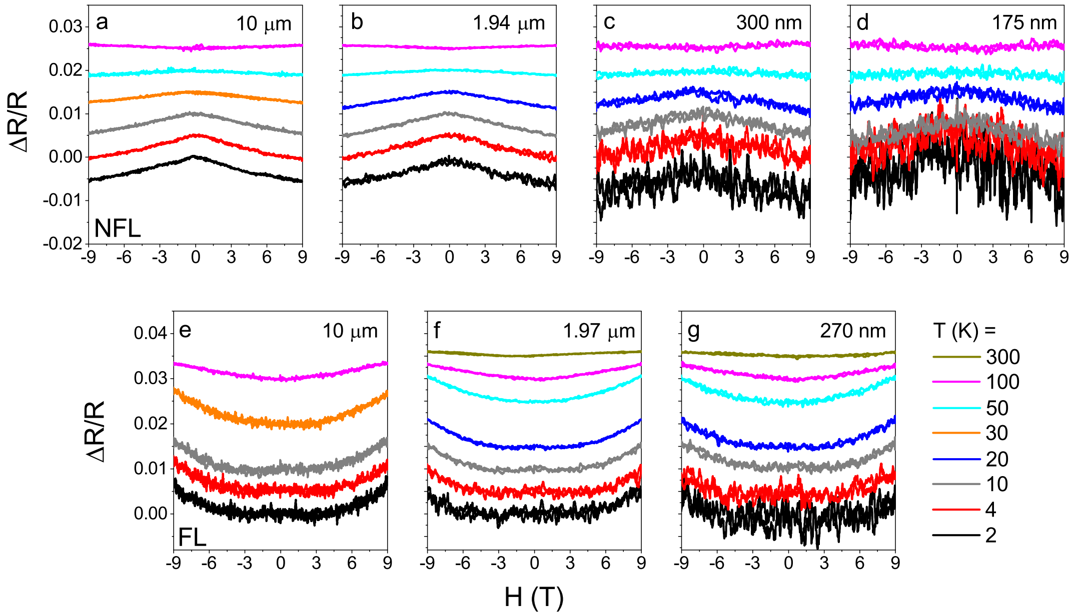

Figure 4.11: **Magnetoresistance isotherms.** Curves are offset by 0.005 per temperature value for clarity. Top row (a-d): MR curves at selected temperatures for NFL samples of various contact separation distances (I = 100 nA). The MR is negative at low temperatures and becomes slightly positive by 100 K. Bottom row (e-g): MR curves at selected temperatures for FL samples of various contact separations (I = 100 nA). The MR is positive at all measured temperatures, with an approximately flat region at low field below 100 K, widening as the temperature is decreased. For both NFL and FL samples, the apparent fluctuation level is nearly constant at different temperatures for curves measured using the relatively large 5 μm wide voltage contacts of a Hall bar device as in (a) and (e), whereas (b-d) show that for various separation distances on a mesa-style sample with $\sim$ 250 nm wide voltage probes, the fluctuation level increases significantly with decreasing temperature at low temperatures. Although the voltage fluctuation level is approximately the same for a given contact size, regardless of the separation distance, that distance determines the total voltage drop and thus, the relative contribution δV/V of the fluctuation amplitude to the resistance signal. Curves taken using longer separation distances therefore look less noisy at low T when plotted as four-terminal resistance. Figure reproduced from [12].

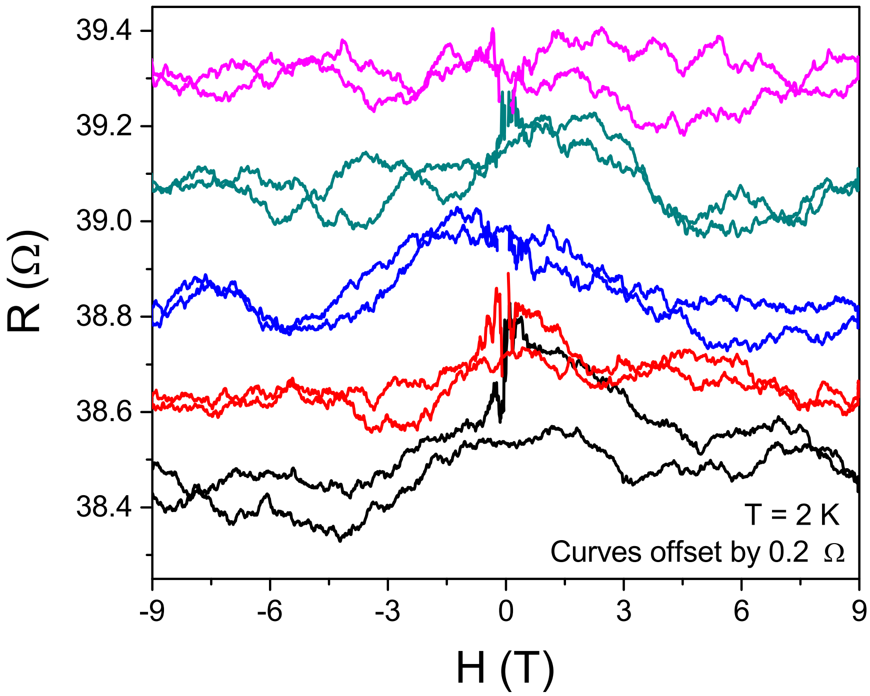

Figure 4.12: **Magnetofingerprint-like MR traces at 2 K.** Five repeated four-terminal MR sweeps for the NFL mesa sample with voltage probes separated by ∼ 125 nm, taken while the temperature was held stable at 2 K and with the current fixed at I = 200 nA. Curves are offset by 0.2 Ω for clarity, starting from lowest (black) trace. For some curve sections, the fluctuations retrace closely upon sweeping from zero to high field and back to zero, which is a characteristic feature of a "magnetofingerprint." However, the effects of time-dependent fluctuations in the potential landscape result in successively acquired MR curves that do not match one another in their detailed fluctuations. Figure reproduced from [12].

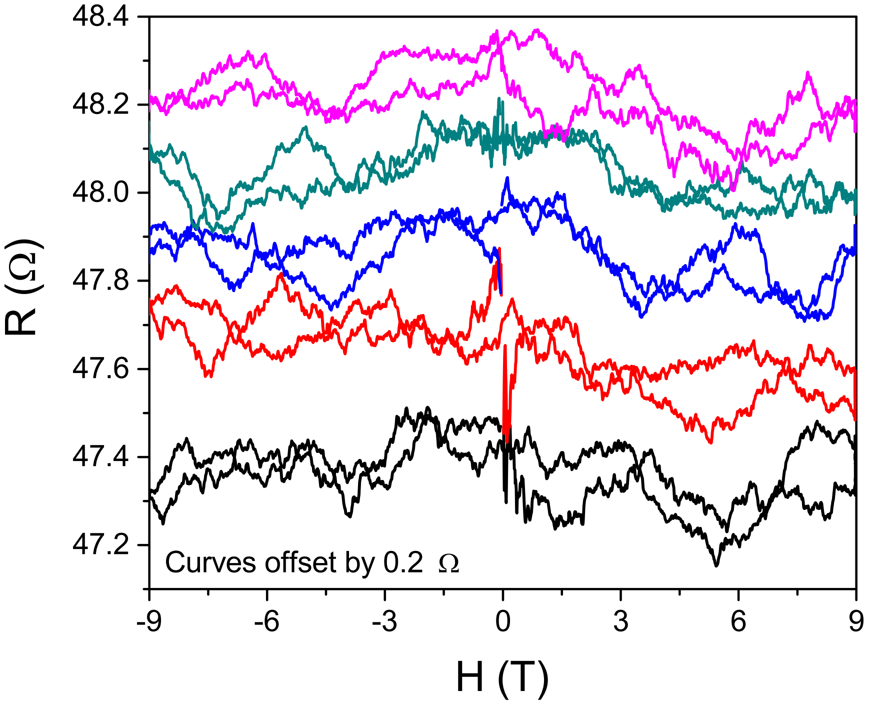

Figure 4.13: Five repeated MR sweeps for the NFL 175 nm contact separation distance. The data were taken consecutively while the temperature was held stable at T = 2 K and the current fixed at I = 100 nA. The effects of time-dependent fluctuations result in MR curves that do not match one another in their detailed fluctuations. Curves are offset by 0.2 Ω for clarity, starting from lowest (black) trace. Figure reproduced from [12].

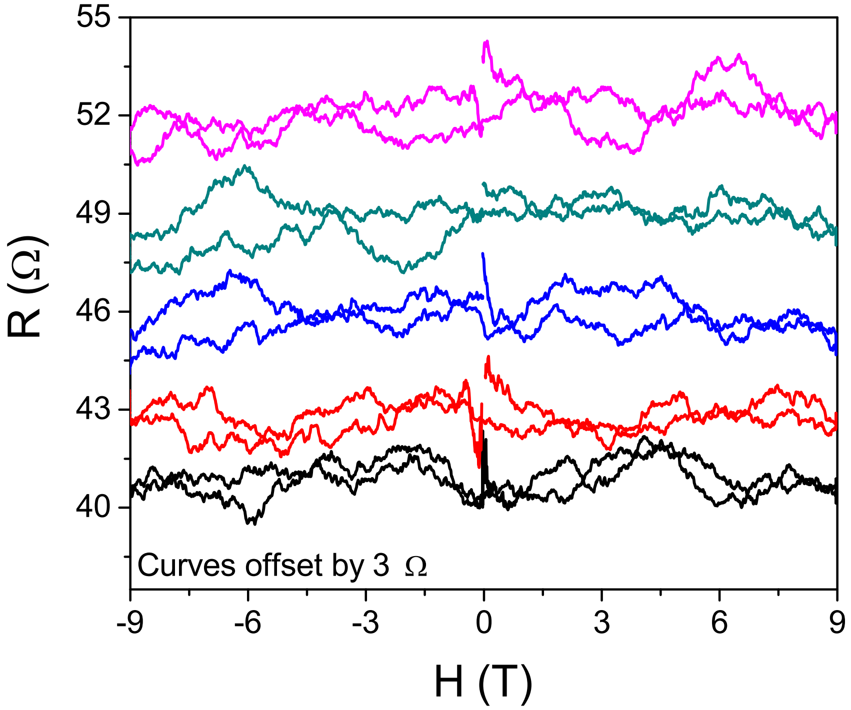

Figure 4.14: Five repeated MR sweeps for the NFL 125 nm contact separation distance taken while the temperature was held stable at T = 2 K and the current fixed at I = 10 nA. The effects of time-dependent fluctuations result in MR curves that do not match one another in their detailed fluctuations. Curves are offset by 3 Ω for clarity, starting from lowest (black) trace. Figure reproduced from [12].

To verify that the large potential fluctuations are indeed due to the intrinsic QW sample properties, it is necessary to rule out other possible origins of fluctuations, which could include instrumental noise, thermal noise, contact effects, and conventional UCF. We first consider the contribution of voltage preamplifier noise (including current noise on the preamplifier voltage inputs), the magnitude of which depends on the impedance of the measured sample. The preamplifier is a Stanford Research Systems SR560, for which in low-noise mode, the input noise floor is about 10 nV/ $\sqrt{Hz}$ for R $<$ 1 kΩ at 10 Hz (see Fig. 4.15). To rule this out as a significant source of noise, we collected time dependent fluctuation data on two kinds of control samples, mounted on the PPMS sample holder and cooled to the same measurement temperatures as for the QW samples. These control samples consisted of either commercial metal film resistors with nominal values of 100 Ω, 1 kΩ, and 10 kΩ (whose resistances were chosen to simulate the two- or four-terminal QW device resistances, and were nearly temperature-independent over the range 2 – 300 K), or an evaporated strip of $Au_{0.6}Pd_{0.4}$ metal film (fabricated on an oxidized silicon wafer by e-beam lithography, e-beam evaporation, and liftoff; dimensions about 10 μm $\times$ 200 μm $\times$ 50 nm) with a room temperature resistance of $\sim$ 88 Ω, falling to $\sim$ 78 Ω at 2 K. The measurement apparatus and control settings (*e.g.*, amplifier gain) were the same as those used for QW studies. These tests showed no dependence of voltage fluctuation level on control sample temperature. For completeness, we also note that the temperature as measured by the internal cryostat thermometer is stable to typically $<$ 10 mK during isothermal measurements.

We also consider the possible role of contact resistance and current noise on the preamplifier inputs in the measured voltage fluctuations enhancement at low temperatures, but find that this can reasonably be ruled it out as the primary source of the large fluctuations. Measurements of the 2-terminal resistance as a function of

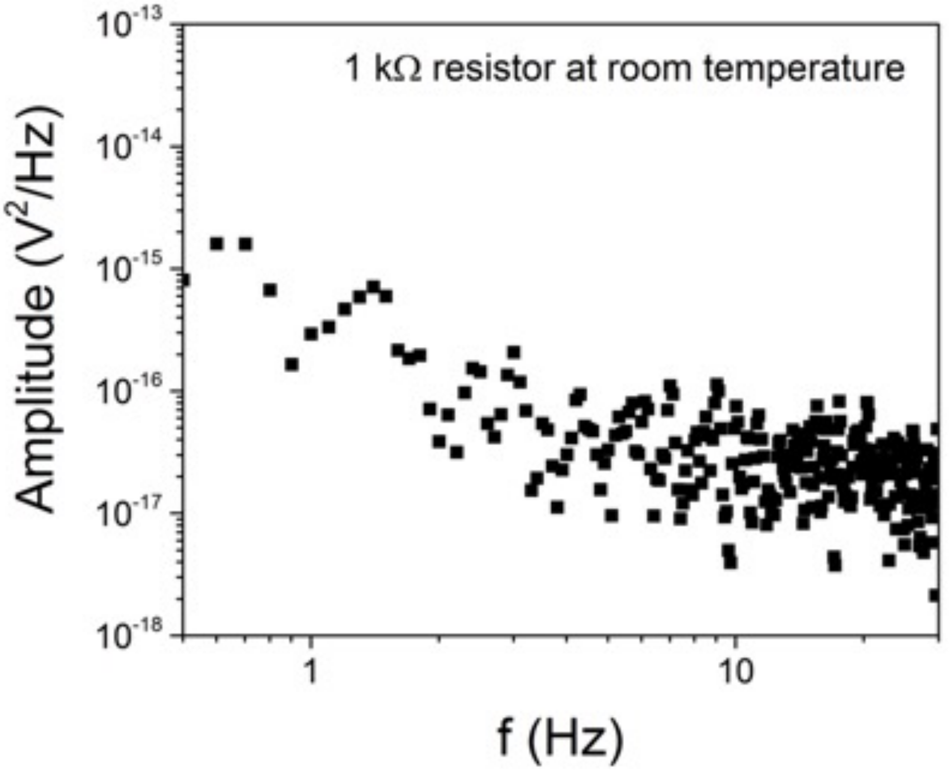

Figure 4.15: Noise floor of measurement setup, verified using a 1 kΩ resistor mounted in a closed metal box at room temperature. These noise values are consistent with expectations from the technical specifications of the voltage preamplifier. Figure reproduced from [12].

temperature (Fig. 4.16) show that the sum of contact and channel resistances does not change greatly over the temperature range in which the potential fluctuations are observed to change by factors of several. For the FL sample, the 2-terminal resistance at 2 K is a factor of $\sim$ 4 smaller than at room temperature, and the increase in 2-probe resistance from 10 K to 2 K is only $\sim$ 10%, while the potential fluctuations grow by more than an order of magnitude over that temperature range (Fig. 4.9a). Given the relatively modest change in 2-terminal resistance over the temperature range studied in both FL and NFL cases, we posit that contact resistance cannot reasonably account for the dramatic increase in voltage fluctuations at low temperatures.

Similarly, the expected Johnson-Nyquist (J-N) noise of the QW sample must also be considered, accounting for both decreasing temperature and increasing two-terminal contact resistance at low temperatures. Using the value of the measured sample resistance (a typical value for four-terminal resistance would be $\sim$ 100 Ω at low temperature, or in the range of a few kΩ for two-terminal resistance, which takes contact effects into account) and the frequency bandwidth Δf of the measurement, the expected J-N noise can be calculated as $V_n = \sqrt{4k_bTR\Delta f}$. At a temperature of 2 K, with a frequency bandwidth of 25 Hz for the FFT measurements, a 100 Ω resistor is expected to have V$_n \sim$ 0.5 nV. This is significantly smaller than the actual measured magnitude of voltage fluctuation of several tens of nV. Even a growing 2-terminal contact resistance at low temperatures cannot explain the observed fluctuations as T is decreased in terms of Johnson-Nyquist noise.

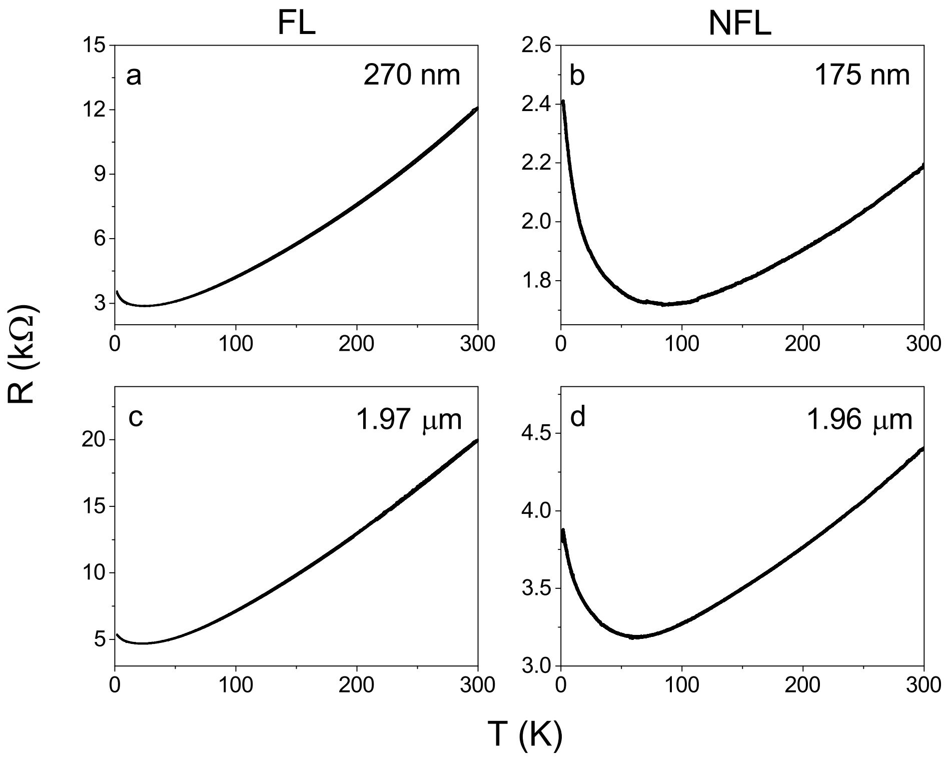

Figure 4.16: Two-terminal resistance versus temperature plots for FL sample (left column, (a) and (c)) and NFL sample (right column, (b) and (d)), for two different contact separation distances on each mesa-style sample. For the FL sample, the 2-terminal resistance drops by a factor of ∼ 4 over the displayed temperature range, and the increase in 2-probe resistance from 10 K to 2 K is only ∼ 10%. For the NFL sample, the 2-probe resistance is not monotonic and increases below ∼ 100 K to a value ∼ 10% higher or lower than at room temperature, depending on the contact set used. However, neither FL nor NFL sample shows a sudden, extreme change in 2-probe resistance occurring near 10 K, when the large potential fluctuations turn on. Figure reproduced from [12].

4.4 Discussion

Taking into account the data presented above, we now seek a self-consistent explanation for the two groups of phenomena observed in the QW samples: the large, low-temperature, current-independent mesoscopic voltage fluctuations observed as a function of time, as well as the magnetofingerprint style resistance (or conductance) fluctuations measured as a function of magnetic field. Recent findings [109] imply that below ∼ 20 K a pseudogap forms in the NFL samples and a zero-bias anomaly appears for the FL samples (the latter consistent with weak depletion of the density of states near the Fermi level), and it makes sense to consider whether these phenomena are relevant to our observations. There is no evidence that the fluctuations are due to proximity to a regime of strong localization, given the samples' low sheet resistance, positive $R(T)$ slope for the FL sample down to 2 K, and very slight low-T upturn in resistivity for the otherwise metallic NFL sample.

The presence of voltage fluctuations even in the absence of an applied current strongly constrains the possibilities. Since both types of samples measured here exhibit similar magnitudes of potential fluctuation, we conjecture that the fluctuations are likely a feature of the conductive SmTO/STO interface and its etching-induced defects, rather than a consequence of FL-to-NFL crossover with STO layer thickness. An explanation involving transduction of a fluctuating thermopower is most consistent with the observations. The difference in Seebeck coefficients of dissimilar metals can generate a net voltage in the absence of any bias current. If some microscopic mechanism causes local temporal fluctuations in the Seebeck coefficient S of the QW electron gas, this would be measured as a fluctuating voltage by the sensing electrodes. These SmTO/STO/SmTO QWs are known to display a relatively large thermopower, on the order of 1-10 μV/K at temperatures below 50 K, [13, 121] and mesoscopic fluctuations in the local chemical potential could credibly manifest as a fluctuating thermovoltage on the order of tens of nV. While full, quantitatively calibrated measurements of the thermopower of the QW/voltage contacts are beyond the scope of this work, preliminary photothermovoltage measurements using optical heating have been performed by Dr. Pavlo Zolotavin in order to check for a resolvable thermally-induced potential difference between two contacts. One of the same mesa-style samples used for transport measurements (NFL type) was mounted in an optical cryostat and cooled to a substrate temperature of 3.5 K. A 785 nm cw laser focused to a ∼ 1 μm spot was raster-scanned over the sample while measuring the potential between a small 250 nm-wide voltage probe and a grounded large current contact. This local optical heating through absorption, which causes a corresponding induced thermophotovoltage, is most significant when the laser spot is positioned directly over the small voltage probe, with a maximum value of ∼ 250 μV when the laser power at the sample is 10 mW (see Fig. 4.17). Based on measurements of the thermopower in these QWs ($S \sim$ 1-10 μV/K at low temperatures, and likely on the lower end of this range, especially below 10 K), [13, 121] the temperature increase due to laser heating can be estimated to be within the range 25-250 K. Conversely, this would imply that a transduced voltage fluctuation of several tens of nV would correspond to a fluctuation of S of approximately <1%. A more well-calibrated method of heating would be required to extract accurate thermopower data, but this method serves as a convenient demonstration of the importance of the Seebeck effect in our QW samples.

Prior work has established that in mesoscopic devices, fluctuation phenomena analogous to what is often observed in electronic transport also appear in thermoelectric transport. A previous experimental study presented results of magnetic-field dependent resistance and thermopower as direct evidence that the Onsager reciprocity relations extend to the case of thermoelectric transport, [122] resulting in mesoscopic fluctuations in thermoelectric coefficients, and there is corresponding theoretical support as well. [123, 124] An additional control experiment was performed using analogous QW structures that were prepared either with or without etching to define a mesa. Here, we used analogous QW structures made with $GdTiO_3/SrTiO_3/GdTiO_3$ [101, 13], grown with the same layer thicknesses as the SmTO/STO/SmTO samples discussed in the manuscript. Structures were fabricated on pristine QW ma-

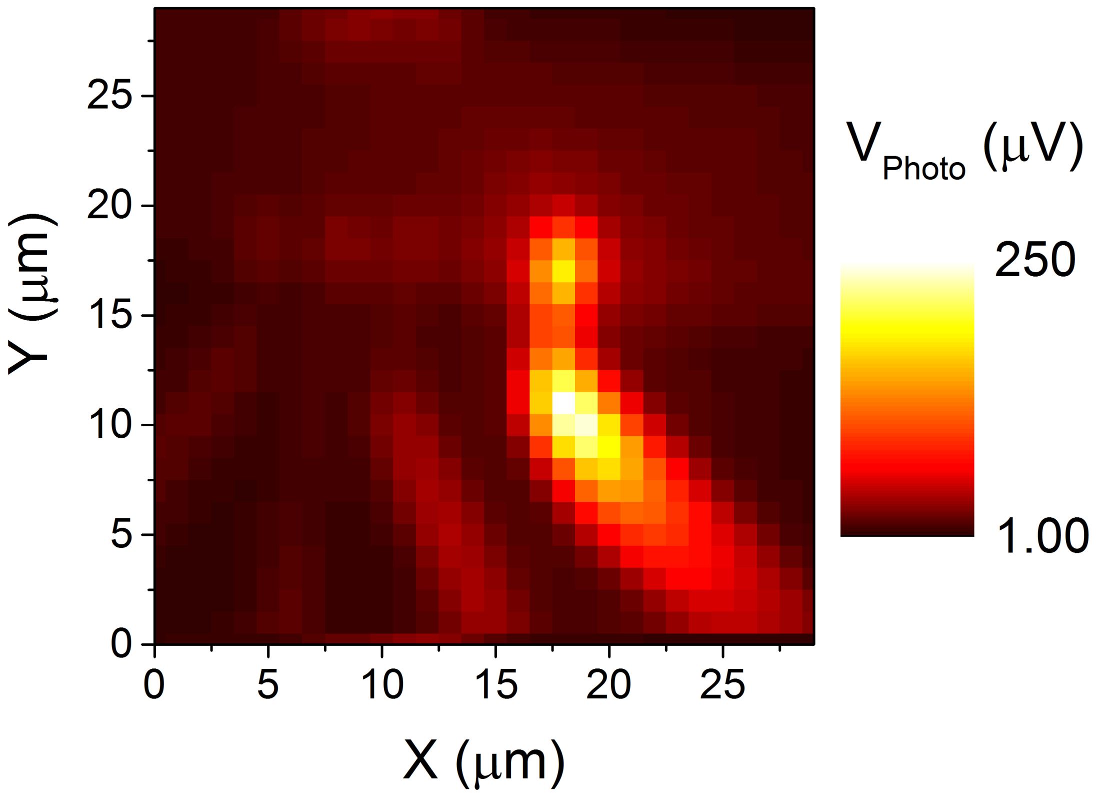

Figure 4.17: **Photothermovoltage mapping of FL mesa-style sample.** The map was produced by raster-scanning a 785 nm cw laser (10 mW at the sample) over the sample at T = 3.5 K while measuring the photovoltage V_{photo} between a narrow voltage contact (brightest area) and a large grounded current lead (not pictured). The contact geometry is the same as shown in Fig. 4.6(b). The shapes of three other narrow contacts are faintly visible in the bottom left quadrant, as is the horizontal edge of the QW mesa near the middle, but the rightmost voltage probe clearly yields the largest photovoltage when the laser is scanned over it. Figure reproduced from [12].

terial by e-beam lithography to form closely-spaced narrow electrodes (inset of Fig. 4.18a), allowing the current flow to be (primarily) confined to a limited area, but without defining a mesa and channel region by etching. In this configuration, no enhancement of time-dependent voltage fluctuations is observed at low temperatures in any measurement, including the temperature-dependent resistivity (Fig. 4.18a), the temperature-dependent voltage between two narrow contacts measured at zero current (Fig. 4.18b), and the low-temperature magnetoresistance. A second set of GdTO/STO/GdTO devices was also fabricated in the etched "mesa-style" configuration (the same as described in the preceding text), and in that case, low-temperature fluctuations are indeed observed, and are very similar to what we discuss in the case of SmTO/STO/SmTO. These results support the idea that etching-related defects are the real culprits of the fluctuation behavior, and that the large Seebeck coefficient serves as a likely mechanism to amplify the effects of local fluctuations in the chemical potential.

A fluctuating Seebeck coefficient with a microscopic origin of fluctuating chemical potential due to two-level defects [125, 126, 127] in the etched nanostructures is reasonable in the context of an emerging pseudogap at low T. The pseudogap in these QW structures emerges over the same temperature range as the increase in voltage fluctuations, as T is reduced below 20 K [109]. The transfer of states away from the Fermi level during pseudogap formation and the resulting energy dependence of the density of states is both likely to enhance potential fluctuations due to defects and to enhance the Seebeck coefficient. An analogous response has been observed previously in germanium single crystals, where carrier density fluctuations result in a $1/f$ noise spectrum of the Seebeck coefficient, even without a dc current. [128] In the case of our QW samples, such carrier density fluctuations could be imagined to occur on one or both sides of the heterointerface, though within the metallic QW system

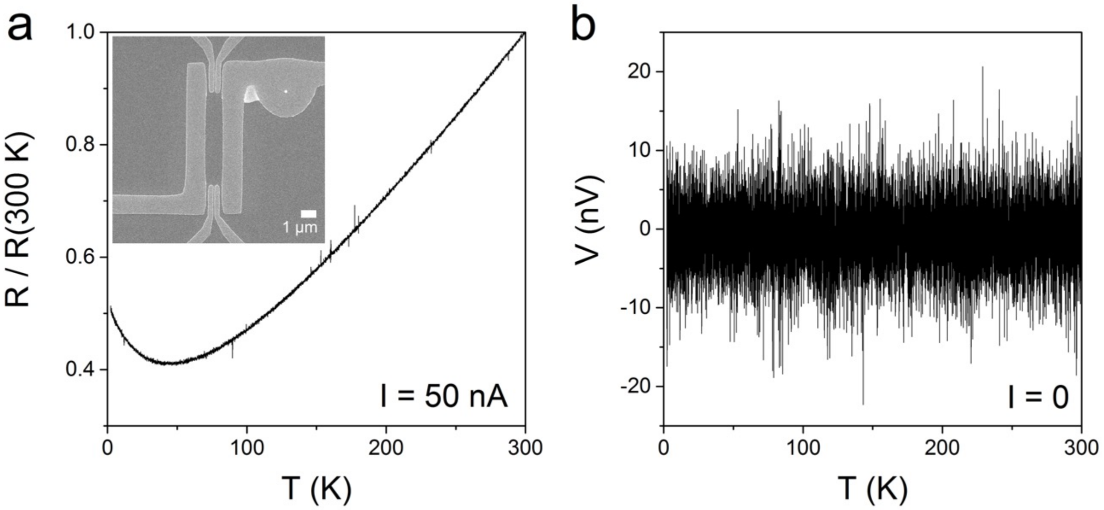

Figure 4.18: (a) The temperature-dependent four-terminal resistance of the GdTO/STO/GdTO test structure with patterned closely-spaced electrodes, prepared without any etch processing. No enhanced low-temperature resistance fluctuations are observed at a measurement current of 50 nA (note that a few small spikes in the otherwise smooth data are measurement artifacts). The inset is an SEM image of the test structure, for which the large L - shaped electrodes at the left and right ends are the designed current electrodes, while the narrow closely spaced inner electrodes (∼70 nm edge-to-edge inner separation) are the potential probes. The lack of enhanced low-T fluctuation level is confirmed in (b), which shows the measured potential difference between the potential probe contacts, without any applied current. Here, the potential fluctuates primarily within the level of ±10 nV over the entire temperature range, which is consistent with our measurement system noise floor. Figure reproduced from [12].

with its carrier density of $\sim\ 10^{14}/\mathrm{cm}^2$, screening should take place on very short length scales. Regarding deviations from pure $1/f$ frequency dependence, while a $1/f$ functional form of distribution of fluctuators is very common, this is not *a priori* required; if there were only a single type of fluctuating defect introduced by etching, one would not expect a broad frequency distribution at all.

Local fluctuations in Seebeck coefficient would be consistent with suppression of the voltage fluctuations in larger contacts, as increasing contact size would lead to ensemble averaging of local fluctuations. In addition to direct measurements of thermopower, another possible test of this picture would be low-temperature Kelvin probe force microscopy, an approach that can locally image spatial and temporal variations in the chemical potential. This specialized technique is, however, beyond the scope of the present work.

The magnetofingerprint MR traces in Figs. 4.12, 4.13, and 4.14 further support the idea that mesoscopic fluctuations are detectable in these oxide QW systems, and that the potential landscape is varying in time. In the presence of static disorder, a retraceable “magnetofingerprint” is the signature of UCF as a function of external magnetic field (MFUCF). Long established as an indicator of coherence in transport on the mesoscopic scale, [68, 111, 112, 113] MFUCF have been reported in other oxide structures. [129, 130, 131, 132] As shown in the figures, the magnetofingerprint is fairly retraceable on the timescale of tens of minutes, but time-varying disorder (due to the presumed two-level fluctuators responsible for the voltage fluctuations) scrambles the MR on the time scale of hours.

4.5 Conclusions

We have studied the transport properties of interface quantum wells in SmTO/STO/SmTO heterostructures using mesoscopic devices with micro/nanoscale electrodes. Unexpected time-dependent voltage fluctuations are observed in devices with the smallest voltage contacts at low temperatures. These fluctuations are found to be suppressed with increasing temperature and contact size, and are independent of the drive current. The suggested mechanism most consistent with the data involves a fluctuating Seebeck coefficient that is transduced as a fluctuating potential at low temperatures. The presence of mesoscopic fluctuations and time-varying disorder is further supported by the observation of "magnetofingerprint" magnetoresistance at the lowest temperatures that is short-time retraceable but shows strong variation on the timescale of hours. This work highlights the need for an improved understanding of the mesoscopic electronic properties in complex oxides that are not necessarily conventional Fermi liquids.

CHAPTER 5

Very Large Magnetoresistance in $\mathbf{Fe_{0.28}TaS_2}$ Single Crystals

---

Part of this chapter is adapted from the published work [14]:

Very Large Magnetoresistance in $Fe_{0.28}TaS_2$ *Single Crystals*

Will J. Hardy, Chih-Wei Chen, Andrea Marcinkova, Heng Ji, Jairo Sinova, Douglas Natelson and Emilia Morosan

Phys. Rev. B **91**, 054426 (2015)
DOI:https://doi.org/10.1103/PhysRevB.91.054426

We now proceed from our discussion of correlated transition metal oxides to consider another class of SCMs: Layered transition metal dichalcogenide (TMD) materials with intercalated magnetic moments. There has been much recent interest in fabricating functional devices using extremely thin (2-dimensional) materials with layered crystal structure, such as graphene and MoS_2. Potential applications of 2d materials to the field of spintronics would crucially depend on availability of layered magnetic materials, yet relatively little attention has been devoted to developing this part of the layered material toolkit. Although most layered materials are not magnetic in their pristine form, intercalation of atoms with magnetic moments between a host crystal's layered planes is one viable route to impart magnetism to these systems. One principal advantage of this method is the ability to tune the strength and type of magnetic interactions present by choosing the host material, intercalated magnetic moment species, and intercalation fraction. Among readily available host compounds, many options exist for the choice of transition metal(s), with S or Se typically used as the chalcogens, although layered tellurides have recently become available as well. In principle, these are all potential candidates for intercalation of magnetic atoms between the layers.

Scientifically, crucial questions regarding many such materials include the nature of interactions of magnetic moments within 2d planes, coupling of the 2d planes with each other, the relative importance of surface effects compared to the bulk, and the evolution of magnetic properties as the crystal thickness is tuned from the bulk toward the single-layer limit along the 2d-plane stacking direction (typically the crystallographic *c*-axis). Crystal thickness can be tuned either through control of growth process parameters, or by thinning bulk crystals using mechanical Scotch tape exfoliation. In this chapter, we consider a layered hard ferromagnet, and then in Chapter 6, we examine a layered antiferromagnet.

For our first example, we explore the idea that magnetic moments intercalated into layered transition metal dichalcogenides are an excellent system for investigating the rich physics associated with magnetic ordering in a strongly anisotropic, strong spin-orbit coupling environment. Specifically, we examine electronic transport and magnetization in $\mathrm{Fe_{0.28}TaS_2}$, a highly anisotropic ferromagnet with a Curie temperature $T_\mathrm{C} \sim 68.8$ K. We find anomalous Hall data confirming a dominance of spin-orbit coupling in the magnetotransport properties of this material, and a remarkably large field-perpendicular-to-plane MR exceeding 60% at 2 K, much larger than the typical

MR for bulk metals, and comparable to state-of-the-art GMR in thin film heterostructures, smaller only than CMR in Mn perovskites or high mobility semiconductors. Even within the $\mathrm{Fe}_x\mathrm{TaS}_2$ series, for the current $x = 0.28$ single crystals the MR is nearly 100× higher than that found previously in the commensurate compound $\mathrm{Fe}_{0.25}\mathrm{TaS}_2$. After considering alternatives, we argue that the large MR arises from spin disorder scattering in the strong spin-orbit coupling environment, and suggest that this can be a design principle for materials with large MR.

5.1 Introduction

In a broader context, the field of spintronics, which concerns the effects on transport due to the coupled spin and charge degrees of freedom of the electron, has raised intense interest due to its broad industrial applications and theoretical challenges.[133, 134, 135, 136, 137] These magnetic transport properties underlie giant, tunneling, and colossal magnetoresistance (GMR, TMR, and CMR),[138, 139, 140, 141, 142] tunneling anisotropic magnetoresistance (TAMR),[143, 144] and the anomalous Hall effect (AHE).[145] Both GMR and TMR are widely observed in thin films[138, 139, 140, 141] where the magnetic coupling between layers can be artificially tuned. Observations in bulk materials[146, 147] revealed that CMR can be a bulk material property. Many mechanisms were suggested for the large magnetoresistance (MR) observed in bulk materials: nanoscale phase separation of the metallic ferromagnetic and insulating antiferromagnetic clusters in manganites;[148, 149] metamagnetic transitions in rare earth intermetallics;[150, 151] and metal-insulator transitions and double exchange interactions for transition metal oxides.[152, 153, 154, 155]

While structures that exhibit GMR and TMR are already widely used in electronic devices, there remains strong technological and fundamental interest in homogeneous materials that exhibit large magnetoresistive effects. Moreover, since ordinary MR effects in bulk metals are typically only a few percent, understanding any occurrences of enhanced MR effects in bulk is of fundamental interest. In the ongoing search for new magnetic materials, transition metal dichalcogenides (TMDs) may be ideal candidates, due to their layered crystal structure and ease of intercalation with magnetic elements.[156, 157, 158, 159] For nearly forty years, the family of layered compounds Fe_xTaS_2 has been the subject of sustained inquiry focused on a surprising variety of anisotropic ferromagnetic properties.[160, 1] The layered structure is visualized in Fig. 1.1. Prior studies have demonstrated that tuning the Fe concentration allows control of these magnetic properties, and measurements of magnetization, MR, and the anomalous Hall effect have been effective probes of the resulting modifications in behavior.[160, 161, 162, 163, 1, 164] Here, we report experimental characterization of such a compound, with $x \approx 0.28$, which exhibits MR in the ordered state exceeding 60%, nearly two orders of magnitude larger than was previously measured. By comparing our complementary results from bulk and thin exfoliated samples, we conclude that the large observed change in resistance is intrinsic and does not result from size-dependent phenomena, such as domain wall scattering. We argue that spin disorder scattering in the presence of strong spin-orbit coupling is the mechanism behind this MR, and that this is a potential paradigm for creating homogeneous materials with large MR. These observations suggest that the TMDs are rich targets for further theoretical study and potential industrial applications.[165]

5.2 Methods

Single crystals of $Fe_{0.28}TaS_2$ were prepared and characterized by Dr. Andrea Marcinkova and Dr. Chih-Wei Chen, working under the guidance of Prof. Emilia Morosan, using iodine vapor transport in a sealed quartz tube, as described elsewhere.[1] The typical size of the resulting bulk $Fe_{0.28}TaS_2$ single crystals was $2\times2\times0.1$ mm^3. Powder x-ray diffraction and analysis of the resulting data, performed by Marcinkova, Chen, and Morosan, revealed the expected $Fe_{0.28}TaS_2$ phase, with the lattice parameters consistent with a composition x between 0.20 and 0.34.[161] Energy-dispersive spectroscopy (EDS) and inductively coupled plasma (ICP) on bulk samples as well were used to more precisely determine the Fe concentration to be $x = 0.28\pm3\%$. I collected the EDS data using a scanning electron microscope (SEM) equipped with an energy-dispersive spectroscopy (EDS) detector. ICP data were collected and analyzed by Chen and Morosan using a Perkin Elmer Optima 8300 ICP-OES system, and the iron concentration of the sample was derived by comparison with commercial iron pure single-element standards (Perkin Elmer). Selected area electron diffraction (SAED) was also performed by Dr. Wenhua Guo (Rice University) at room temperature. For this measurement, a bulk single crystal was ground in ethanol using an agate mortar and pestle, and a drop of this crystal-containing ethanol was placed on a holey carbon TEM grid and allowed to dry naturally.

I processed bulk crystals into exfoliated samples using the tape exfoliation method [55], and characterized the prepared samples. Bulk $Fe_{0.28}TaS_2$ single crystals were mechanically cleaved using blue Nitto SPV 224 tape, and the resulting exfoliated crystals were deposited onto an oxidized silicon wafer (300 nm or 2 μm oxide thickness). Metallic contacts were defined using standard electron beam lithography and development. Contact metals were then deposited by electron beam evaporation of a Ti, Cr, or Fe adhesion layer ($\sim$ 3 nm) and Au (50 nm); an extra 20 nm of Au was added by sputtering.

For the exfoliated samples, the thickness was determined using atomic force microscopy (AFM). The measured thickness, with average values between 80 and 180 nm, varied by up to 21% within each sample. Scanning electron microscopy (SEM) images showed that the exfoliated flakes had lateral dimensions on the order of 10 μm, with variation from sample to sample. Thinner samples could only be produced with lateral dimensions much smaller than 10 μm due to relatively strong bonding between the layers compared to, *e.g.*, graphite. Two exfoliated samples were prepared with electrodes configured to enable Hall measurements as well as conventional MR, while a third exfoliated sample was prepared for MR alone. Voltage probes were separated by less than 5 μm in these devices.

Temperature- and field-dependent magnetization data for bulk $\mathrm{Fe_{0.28}TaS_2}$ were collected by Marcinkova, Chen, and Morosan in a Quantum Design (QD) Magnetic Property Measurement System (MPMS). Temperature- and magnetic field-dependent AC resistivity measurements were performed in a QD Physical Property Measurement System (PPMS) using standard four-probe methods, for both bulk samples (by Marcinkova, Chen, and Morosan) and exfoliated $\mathrm{Fe_{0.28}TaS_2}$. Additional Hall resistivity data were collected using a five probe configuration for both the bulk and the exfoliated samples. Angle-dependent transport measurements were performed on an exfoliated sample mounted on a QD horizontal rotator insert, which allowed the sample to be rotated relative to the magnetic field direction.

5.3 Results and discussion

$\mathrm{Fe}_x\mathrm{TaS}_2$ is a unique intercalated transition metal dichalcogenide (TMD), with its strong and non-monotonic dependence of the magnetic properties (the ground state – ferromagnetic or antiferromagnetic, the ordering temperature) on the Fe concentration x.[161, 162, 163] It has been shown that a 3% difference in the Fe concentration (from 0.25 to 0.28) causes a modification of T_C as large as 90 K (from 160 K to 70 K),[1, 162] while increasing x from $x < 0.40$ to $x \geq 0.40$[162, 163] results in a change of the magnetic interactions from ferro- (FM) to antiferromagnetic (AFM). In the current $\mathrm{Fe_{0.28}TaS_2}$ single crystals, the $H \parallel c$ temperature-dependent magnetic susceptibility measurements (Fig. 5.1a) are consistent with the onset of FM order below ~ 70 K upon cooling. The $H = 0$ temperature dependent resitivity data $\rho(T)$ on bulk (open symbols) and exfoliated (solid line) samples are virtually identical, as

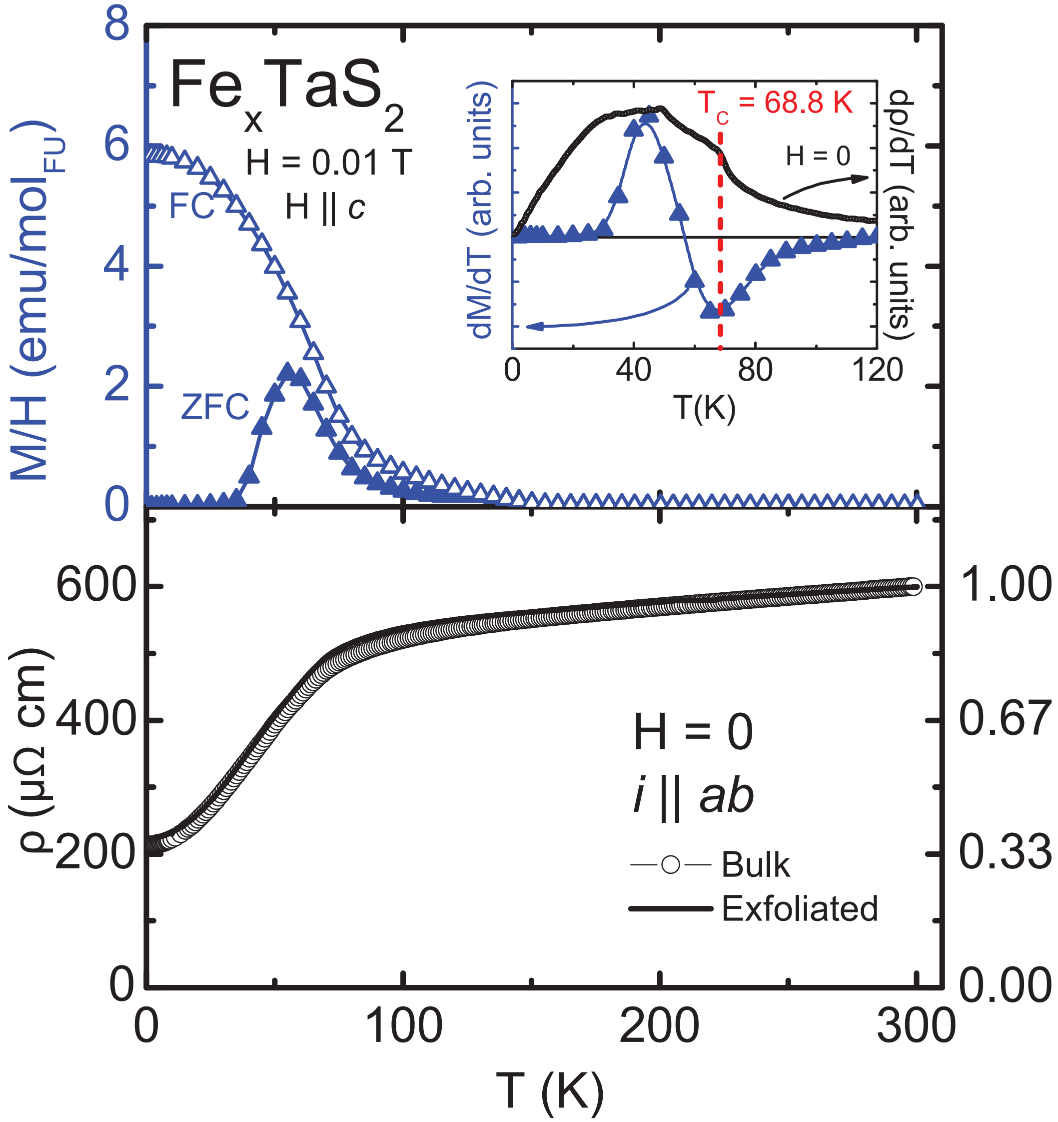

Figure 5.1: **Magnetization and resistivity vs. T of bulk Fe$_{0.28}$TaS$_2$** (a) ZFC (solid symbols) and FC (open symbols) temperature-dependent magnetic susceptibility of a bulk sample measure in an applied field $H = 0.1$ T, $H \parallel c$. Inset: The Curie temperature T_C is determined from the minimum in dM/dT (solid symbols) and an inflexion point in $d\rho/dT$ (line).and. (b) Temperature-dependent resistivity of both bulk (open symbols) and exfoliated (solid line) samples. Figure reproduced from [14].

can be seen in Fig. 5.1b. The weakly linear decrease in $\rho(T)$ at high T is indicative of the poor metal behavior in both bulk and exfoliated samples, while a drop below 70 K is consistent with loss of spin disorder scattering in the FM state. The derivatives of the ZFC magnetization data dM/dT (symbols, inset) and the bulk resistivity data $d\rho/dT$ (line, inset) suggest that the Curie temperature T_C is close to 68.8 K, if T_C is determined from the minimum in dM/dT and the inflection point in $d\rho/dT$ (vertical dashed line). The T_C value is consistent with the reported T_C for $Fe_{0.28}TaS_2$.[162] We do find the onset of irreversibility in the zero-field-cooled (ZFC, solid symbols) and field-cooled (FC, open symbols) $M(T)$ data occurs around 150 K, well above T_C for x

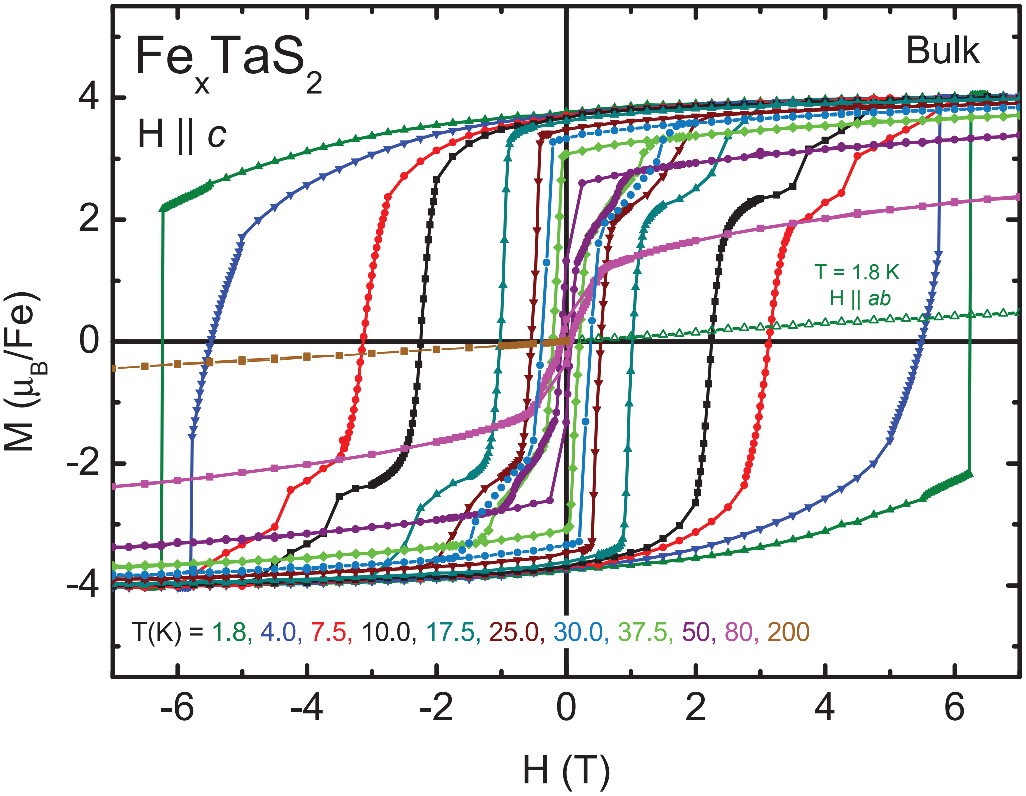

Figure 5.2: **Magnetization vs. field of bulk $Fe_{0.28}TaS_2$** H ∥ c (full symbols) field-dependent magnetization $M(H)$ data at various temperatures, together with the $T = 1.8$ K, $H \parallel ab$ (open symbols) isotherm. For clarity, the two close isotherms ($H \parallel c$ for $T = 200$ K and $H \parallel ab$ for $T = 1.8$ K) are only shown for $H < 0$ and $H > 0$, respectively. Figure reproduced from [14].

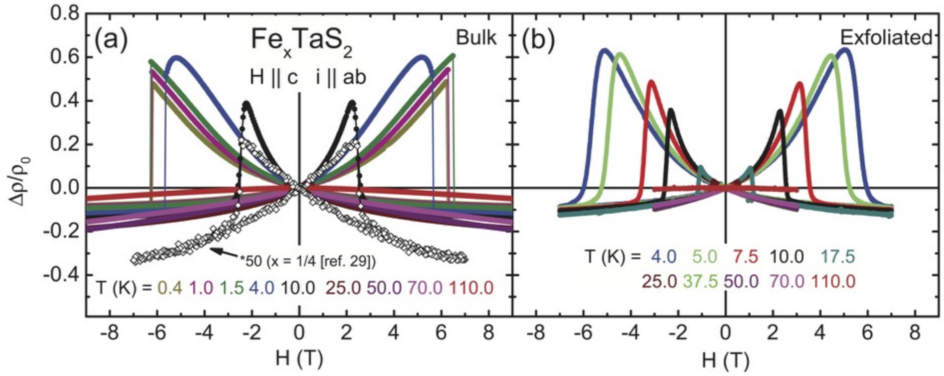

Figure 5.3: **Magnetoresistance of $\mathbf{Fe_{0.28}TaS_2}$** MR of (a) bulk and (b) exfoliated samples at selected temperatures for $H \parallel c$, and the current $i \parallel ab$. Figure reproduced from [14].

= 0.28 and very close to that for $x = 0.25$.[1] This may be due to a small amount of Fe ions forming a commensurate superstructure as in Fe$_{0.25}$TaS$_2$, which, however, has very little effect on the transport properties, where the transition is not even visible.

Remarkable behavior is observed in field-dependent magnetization and resistivity measurements with the magnetic field H along the reported easy axis $H \parallel c$.[1] The magnetization isotherms $M(H)$ of the bulk single crystals (Fig. 5.2) reveal a sharp switching, similar to that for both Fe$_{0.28}$TaS$_2$[161] and Fe$_{0.25}$TaS$_2$ compounds.[1] The switching field H_S is defined as the field where the magnetization crosses zero and where, as will be shown, the MR $\Delta\rho/\rho_0$ and Hall resistivivity ρ_{xy} display rapid changes as a function of H $\parallel$ c. In this study, both H_S and the sharpness of the transition decrease with increasing temperature. H_S at 1.8 K has the highest value of 6.23 T, while at $T = 4$ K, $H_\mathrm{S} = 5.5$ T, very close to value reported for Fe$_{0.28}$TaS$_2$.[160] A second step-like feature in $M(H)$ appears for $7.5 \leq T \leq 80$ K and disappears when $T > 200$ K. While this could simply be attributed to the small amount of Fe$_x$TaS$_2$ phase with $0.25 \leq x \leq 0.28$, this scenario is inconsistent with the absence of the additional $M(H)$ step at the lowest temperatures. Another possible explanation for the second step-like feature could be heat release during the dynamic switching

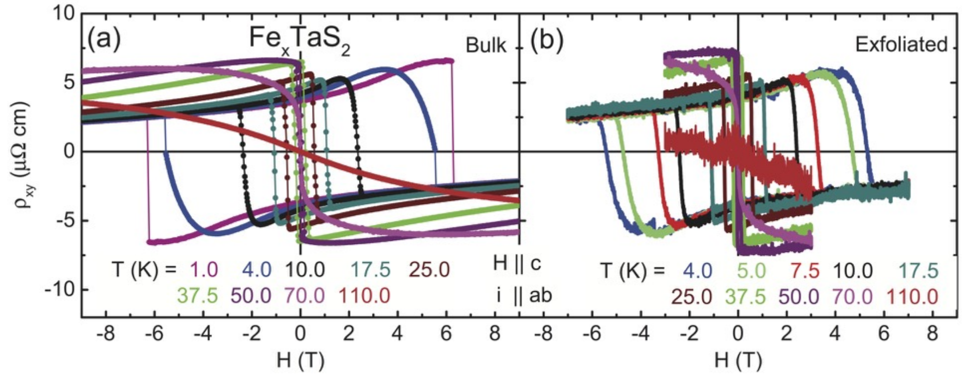

Figure 5.4: **Hall effect measurements of Fe$_{0.28}$TaS$_2$** Anomalous Hall resistivity for (a) bulk and (b) exfoliated samples at selected temperatures for $H \parallel c$, and the current $i \parallel ab$. Figure reproduced from [14].

process in the bulk crystals, which could alter the shape of $M(H)$. We do note that the magnetic and transport measurements are reproducible after the samples remain at low temperatures for long periods of time, and after performing multiple field sweeps at different sweep rates. Moreover, the $H \parallel c$ resistivity data ρ(H) in Fig.5.3 and anomalous Hall resistivity in Fig.5.4 feature a sharp jump at H_{S}.

MR is a crucial measurement for inferring information about the interactions between itinerant charge carriers and the magnetic degrees of freedom in a variety of magnetic materials.[166, 167] The MR is defined as:

$$\frac{\Delta\rho}{\rho_0} = \frac{\rho_{xx}(H) - \rho_{xx}(0)}{\rho_{xx}(0)}$$

where $\rho_{xx}(H)$ is the value of the resistivity in a magnetic field H. The $\Delta\rho/\rho_0$ measurements, with magnetic field H applied along the c axis, were performed at selected temperatures for both bulk and exfoliated Fe$_{0.28}$TaS$_2$ single crystals (Fig. 5.3a and b respectively). Below $T_{\mathrm{C}} \approx$ 68.8 K, as the magnetic field H increases from 0 to 9 T, $\Delta\rho/\rho_0$ smoothly increases to its maximum value at H_S and sharply drops in a very narrow H interval ΔH, followed by a nearly linear decrease up to the maximum measured field $H = 9$ T. When the magnetic field direction was reversed, the same change in $\Delta\rho/\rho_0$ was observed, resulting in a bow-tie shape of $\Delta\rho/\rho_0$ after one full cycle of field sweeping.

Qualitatively, this MR field-dependence resembles that for $Fe_{0.25}TaS_2$.[1] However, the absolute $\Delta\rho/\rho_0$ values are remarkably high in $Fe_{0.28}TaS_2$ (full symbols, Fig. 5.3a), nearly two orders of magnitude larger than that observed for $x = 0.25$ (open symbols, Fig. 5.3a). In both bulk and exfoliated $Fe_{0.28}TaS_2$ crystals, the largest $\Delta\rho/\rho_0$ close to 60% was observed at $T = 4$ K (blue, Fig. 5.3). Furthermore, both $\Delta\rho/\rho_0$ and H_S decreased with increasing temperature, and the bow-tie shape of the $\Delta\rho/\rho_0$ curves disappears above T_C when $\Delta\rho/\rho_0$ becomes nearly linear for the whole measured field range. It should be noted that ΔH is much smaller in bulk (~ 0.04 T) than in the exfoliated sample (~ 0.8 T) at lower temperatures, and becomes comparable (~ 0.3 T) in both as the temperature exceeds 10 K. The broadening of the transition with increasing T in the bulk seems natural, while the opposite effect (sharpening) in the exfoliated sample emphasizes the role of the long range interplanar coupling in $Fe_{0.28}TaS_2$. This may imply that long range coupling exists between the Fe ions in different layers, which is weakened in the exfoliated sample, even when 100 nm thick.

The observed magnitude of the MR in $Fe_{0.28}TaS_2$, comparable to that seen in GMR and TMR systems, is remarkably large for a homogeneous bulk material not going through a phase transition (as in CMR systems). A useful point of comparison is (Ga,Mn)As, which has a similar ρ vs. T response.[167] This latter material exhibits ordinary AMR, a spin-orbit coupling effect,[166] which is typically at most a few percent in bulk materials based on $3d$ transition metals. To gain insight into the very large MR in $Fe_{0.28}TaS_2$ it is necessary to correlate with other field-dependent measurements, like anomalous Hall effect (AHE). As previously observed in $Fe_{0.25}TaS_2$ and $Fe_{0.28}TaS_2$,[164, 162] the Hall resistance ρ_{xy} for both bulk and exfoliated samples displays hysteresis below T_{C} , with jumps at $\pm$ H_{S} (Fig. 5.4). As was the case for $\Delta\rho/\rho_0$ (Fig. 5.3), ρ_{xy} has a sharper jump at $\pm$ H_{S} in the bulk sample than in the exfoliated one below 4 K, but then became comparable at higher temperatures. When H exceeds $\pm$ H_{S}, the Hall resistivity ρ_{xy} becomes almost linear in field, a result of the ordinary Hall effect contribution. For temperatures above T_{C} , only the ordinary Hall effect is observed, as $\rho_{xy}(H)$ is again nearly linear in H. Note that the Hall coefficient R_H in $\mathrm{Fe_{0.28}TaS_2}$ does not change sign throughout the ordered state, in contrast to the situation in $\mathrm{Fe_{0.25}TaS_2}$.[164] Converting into the Hall conductivity, the change in σ_{xy} when passing through H_{S} at 4 K is close to 200 S/cm, essentially the same as that seen in the $x = 0.25$ compound,[164] and exceeding the values typically seen in (Ga,Mn)As by a factor of five [168]. These results imply that the spin-orbit coupling is very strong in this material and is very similar in the $x = 0.28$ and $x = 0.25$ compositions.

We must consider candidate mechanisms to explain the magnetotransport properties of the $\mathrm{Fe_{0.28}TaS_2}$ single crystals, in particular the remarkably large $H \parallel c$ MR. One natural possibility is AMR,[166] parametrized in terms of the resistivities measured with the current density $\mathbf{J}$ parallel or perpendicular to the magnetization $\mathbf{M}$, $\rho_{||}$ and $\rho_{\perp}$, respectively. Generally the difference between the two $\rho_{\Delta} \equiv \rho_{||} - \rho_{\perp}$ is positive. The prior work[164] on the $x = 0.25$ compound ascribed the small (a maximum $\Delta\rho/\rho_0 \approx 1.5\%$ at 1.5 K) MR for $H \parallel$ c to a ρ_{Δ} of $+260$ $\mu\Omega$-cm and a splaying of the spins as $H \rightarrow H_S$ by about 0.1°. The large value of ρ_{Δ} is consistent in that case with in-plane MR measurements out to very high fields, showing $\Delta\rho/\rho_0 \approx 40\%$ for $H \perp c$ and $H = 31$ T, corresponding to a tilting of M away from the c-axis by around 15°.[164] Note that in these $x = 0.25$ in-plane measurements at 10 K, an in-plane field of several Tesla is able to cant M sufficiently to produce a measured AMR of several percent.

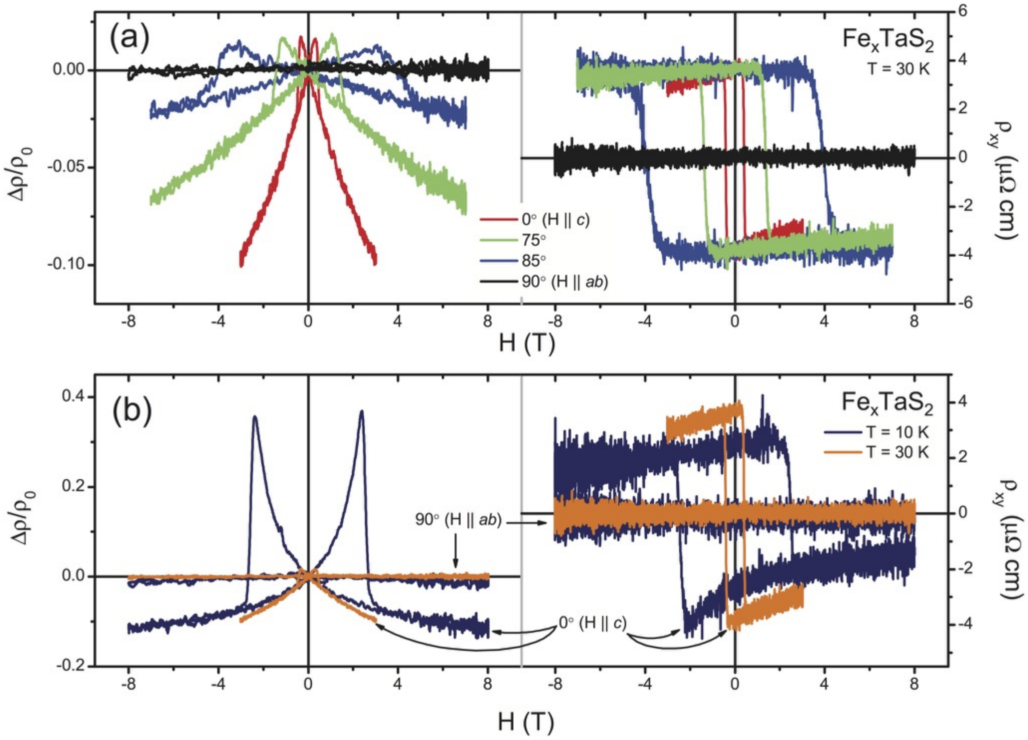

Figure 5.5: **Angle-dependent measurements of Fe$_{0.28}$TaS$_2$** Angle-dependent measurements on an exofoliated sample of the longitudinal MR (left) and Hall resistivity (right) as a function of magnetic field H, for $H \parallel c$, and the current $i \parallel ab$. (a) Data at $T = 30$ K for various field orientations relative to the c axis. (b) Comparison of $H \parallel c$ and $H \parallel ab$ data for $T = 10$ and 30 K. Figure reproduced from [14].

In our $x = 0.28$ compound, it is not unreasonable to assume a similar magnitude of ρ_Δ, given the similarity of the spin-orbit coupling (inferred from the anomalous Hall conductivities) and the switching fields. Our observed magnitude of $\Delta\rho/\rho_0$ for $H \parallel c$ would then imply a canting or splaying of the spins by tens of degrees immediately prior to magnetization reversal ($|H|$ less than or approximately equal to $|H_\mathrm{S}|$). Indeed, a significant rounding of $M(H)$ (Fig. 5.2) and $\sigma_{xy}(H)$ (Fig. 5.3) near H_S for $H \parallel c$ below, *e.g.*, 10 K would at first glance seem to be compatible with this idea. However, angular dependent MR measurements on $\mathrm{Fe_{0.28}TaS_2}$ strongly disfavor this possibility. Fig. 5.5 displays MR $\Delta\rho/\rho_0$ (left) and $\rho_{xy}(H)$ (right) data for (a) different field orientations relative to the c-axis and constant temperature T = 30 K, and (b) two extreme field orientations: $H \parallel c$ and $H \parallel ab$ for T = 10 K (navy) and 30 K (orange). Within the AMR scenario of canting or splaying of the spins, one would expect significant canting of the magnetization when $H \parallel ab$ if such reorientation of $\mathbf{M}$ could happen with H antialigned to $\mathbf{M}$ along c. Instead, there is essentially no detectable magnetoresistive or anomalous Hall response for $H \parallel ab$, and the magnetization response along that field direction (open symbols, Fig. 5.2) is correspondingly weak. This is in contrast to the $x = 0.25$ case described above. These observations suggest that the easy axis of magnetization is strongly aligned with the c-axis, given that an in-plane field of 8 T is insufficient to produce any detectable MR or Hall signal. Thus ordinary AMR seems incompatible with the full ensemble of data, and AMR in the $x = 0.28$ case appears to be quite different than at $x = 0.25$.

Giant magnetoresistance (GMR)[138, 139] is another mechanism capable of producing magnetoresistive effects of tens of percent. GMR results from the interplay between spin-split band structure and the density of states available for each spin species for scattering at the Fermi level. A magnetically inhomogeneous material can exhibit GMR due to current flow between differently aligned magnetic domains.[169]

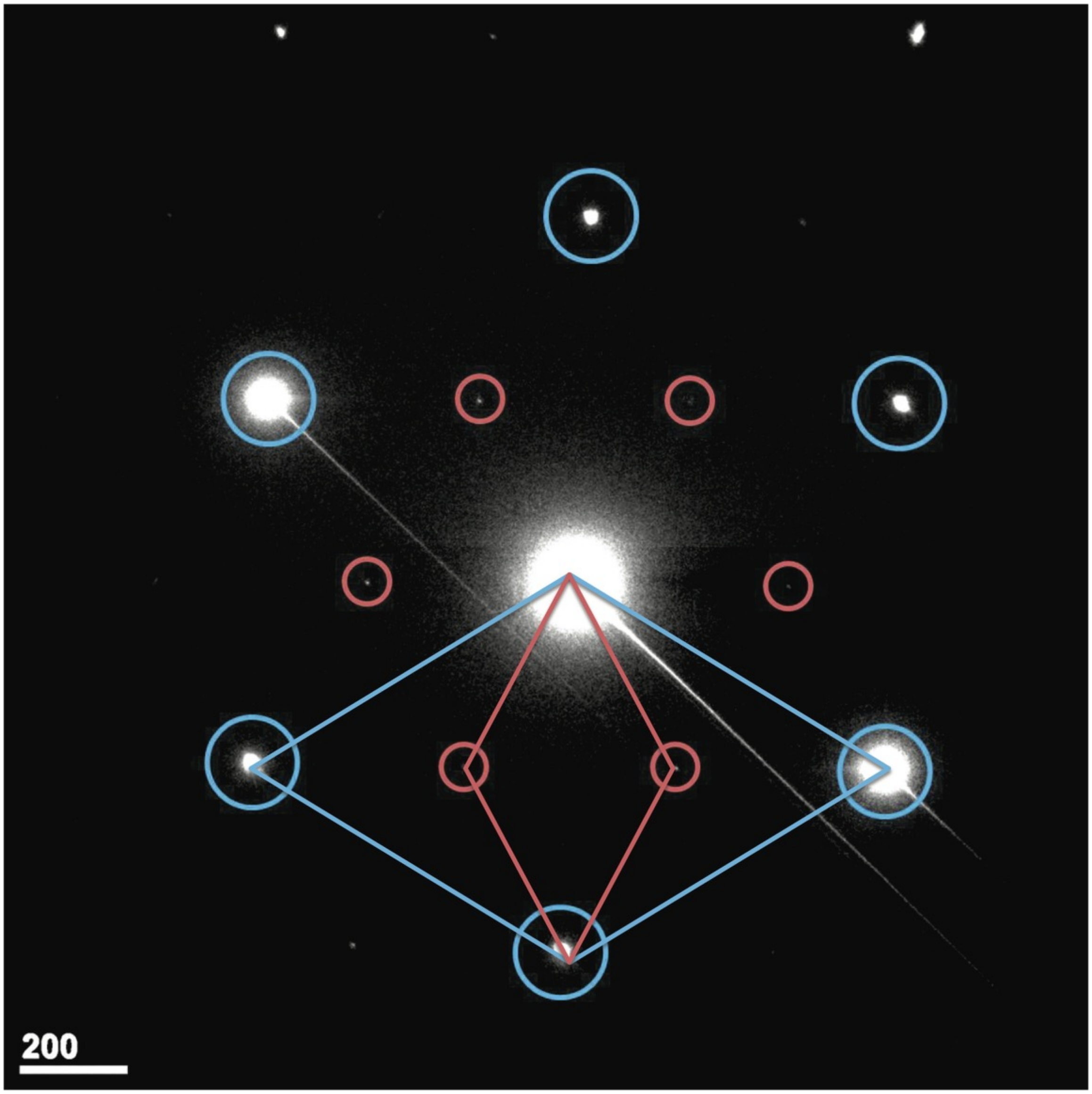

Figure 5.6: **Electron diffraction study of $\mathbf{Fe_{0.28}TaS_2}$**: SAED pattern of $Fe_{0.28}TaS_2$ crystal showing two concentric hexagonal sets of spots: the main structure (bright, large circles) and superlattice reflections (faint, small circles). The superstructure unit cell (small hexagonal cell) appears rotated by 90° from the main structure unit cell (large hexagonal cell). Figure reproduced from [14].

To be a plausible explanation of our data would require that the magnetic domain structure of the material evolve as $H \rightarrow H_{\mathrm{S}}$ so that charge transport is forced to take place across an increasingly large number of boundaries between antialigned domains. This can be tested through magneto-optic studies of the domain structure (beyond the scope of the present work). However, the micro-scale exfoliated samples have transport properties that look very similar to those of the bulk crystals, including a lack of any step-like features in the MR or anomalous Hall data as a function of field. This shows that the flipping of discrete domains near H_{S} and resultant GMR are unlikely to be responsible for the observed large MR. Note further that the domains observed via magneto-optic methods in the $x = 0.25$ composition[170] are typically tens of μm in extent. In the current $x = 0.28$ exfoliated samples the few-μm spacing of the voltage probes combined with the lack of any discrete magnetoresistive or AHE signatures in these devices implies that any domains would have to be much smaller than the μm scale - very different than the $x = 0.25$ case, and difficult to image. Conversely, the similarity in the $M(H)$ data between this study and previous measurements on $\mathrm{Fe}_{0.25}\mathrm{TaS}_2$ suggests that the domain structures are likely very similar. Therefore, domain wall scattering is unlikely the cause of the large observed MR.

We suggest that the mechanism for the extremely large $H \parallel c$ MR and the near-absence of MR when $H \parallel ab$ is spin disorder scattering.[171, 172] The prominent drop in $\rho(T)$ when T falls below T_{C} is readily apparent in Fig. 5.1, showing that spin disorder scattering accounts for approximately 50% of the total scattering relevant to the resistivity above T_{C}. In the case of large spin-orbit coupling (SOC, as indicated by the size of the anomalous Hall conductivity in this material), it is not surprising that spin disorder can be so important. Rather than carrier-magnon scattering or Kondo physics, with the strong anisotropy and SOC the proposed mechanism for the large MR in the current $x = 0.28$ system is scattering from a (quasistatic) disordered arrangement of antialigned moments. In the presence of strong SOC, such spin disorder can be very effective at scattering carriers relative to ordinary potential disorder, since it mixes spin channels and therefore permits greater phase space for scattering.

In the electron diffraction measurements performed on the $Fe_{0.28}TaS_2$ single crystals by Dr. Wenhua Guo (Fig. 5.6), two concentric sets of spots are observed in the *ab* plane, each with sixfold symmetry. The bright spots (large circles) are due to the main TaS_2 phase, while the faint spots (small circles) are assumed to result from an ordered Fe superstructure. When compared to the diffraction patterns presented in a recent study by Horibe *et al.*,[173] the present SAED pattern appears more similar to that of $Fe_{1/3}TaS_2$ than that of $Fe_{1/4}TaS_2$, with the interior hexagon rotated by 90° in relation to the outer one and the resulting superstructure close to $\sqrt{3} \times \sqrt{3}$. The appearance of the superstructure spots in the electron diffraction (Fig. 5.6) indicates that it may be useful to think about the $x = 0.28$ system as a compound with a commensurate $x = 0.25$ Fe structure with additional Fe local moments ($x = 0.25 + \delta$), or $x = 0.33$ Fe structure with missing Fe local moments ($x = 0.33 - \delta$) with small δ ($\delta \leq 0.05$). In either case, the moments in a disordered environment, while coupled ferromagnetically to the bulk, would be expected to have weaker exchange interactions[174] than those on the superstructure sites, and hence would be easier to antialign with the field as $(H \parallel c) \rightarrow H_S$. The maximum MR for this field orientation is seen at H_S as the spins reverse their orientation, leading to an increase in scattering comparable to the spin-disorder contribution to ρ. In other words, during the MR measurement, the antialignment of a significant fraction of the local moments as the field strength is increased (antiparallel to the bulk magnetization) results in enhanced scattering and increased resistance. Once the remaining spins flip to become aligned with the external field, spin disorder scattering is greatly reduced, causing a sharp drop in resistance. Canting of the moments is disfavored by the large magnetic anisotropy, while enhanced scattering (relative to potential scattering) is favored due to strong SOC and channel mixing.

Additional experiments can be used to test this hypothesis. This explanation assumes a population of weakly-coupled, easier-to-reorient spins due to deviations from the $x = 0.25$ stoichiometry. One would therefore expect a monotonic increase in the the $H \parallel c$ MR as x is increased from $x = 0.25$ to $x = 0.28$, as has been subsequently shown by Chen et al. [175]. The dynamics of the spin reorientation should also be manifested in the MR response in this case, though no field sweep rate dependence has been observed so far. Optical perturbation of the local moment orientation would also be expected to lead to large resistive effects.

In conclusion, we show that $Fe_{0.28}TaS_2$ single crystals display remarkably large MR, up to 60%, when the applied magnetic field $H \parallel c$. Both the magnetization and transport properties appear nearly insensitive to sample thickness down to $\sim$ 100 nm, as measurements on bulk and exfoliated single crystals are nearly indistinguishable. As is illustrated in Fig. 5.7 for $T = 10$ K, the switching field H_S values observed from magnetization and magneto-transport measurements on both bulk and exfoliated samples are very close at all temperatures up to T_C. The resulting temperature dependence of H_S (squares) and $\Delta\rho/\rho_0$ at H_S (circles) shown in Fig. 5.8 is indeed identical for both the bulk (full symbols) and exfoliated (open symbols) samples. Moreover, the non-monotonic change with x of the ordering temperature T_C and switching field values H_S between the $Fe_{0.28}TaS_2$ system and the previously reported $Fe_{0.25}TaS_2$ superstructure[1], and, more significantly, the nearly two order of magnitude enhancement of MR in the former compound, appear to be consistent with a scenario of disordered Fe moments mixed with a Fe superstructure. This scenario is even more plausible, given the experimental evidence we present to rule out other likely possibilities, such as AMR or an analog of GMR due to domain structure. The spin disorder scattering scenario reveals a design principle for intrinsically magnetoresistive materials without the need for multilayers or metal-insulator transitions coupled to magnetism. Conditions favoring maximal MR would include: single crystal materials, so that grain boundary, potential disorder, and surface scattering do not limit the mean free path; ferromagnetism with very strong uniaxial anisotropy, to favor moment flipping rather than canting as H is increased; and very strong spin-orbit coupling, magnifying the scattering cross-section of “misaligned” spins. Transition metal dichalcogenides intercalated with various amounts of magnetic metals are promising materials where these optimal intercalation conditions may be achieved to maximize the observed MR.

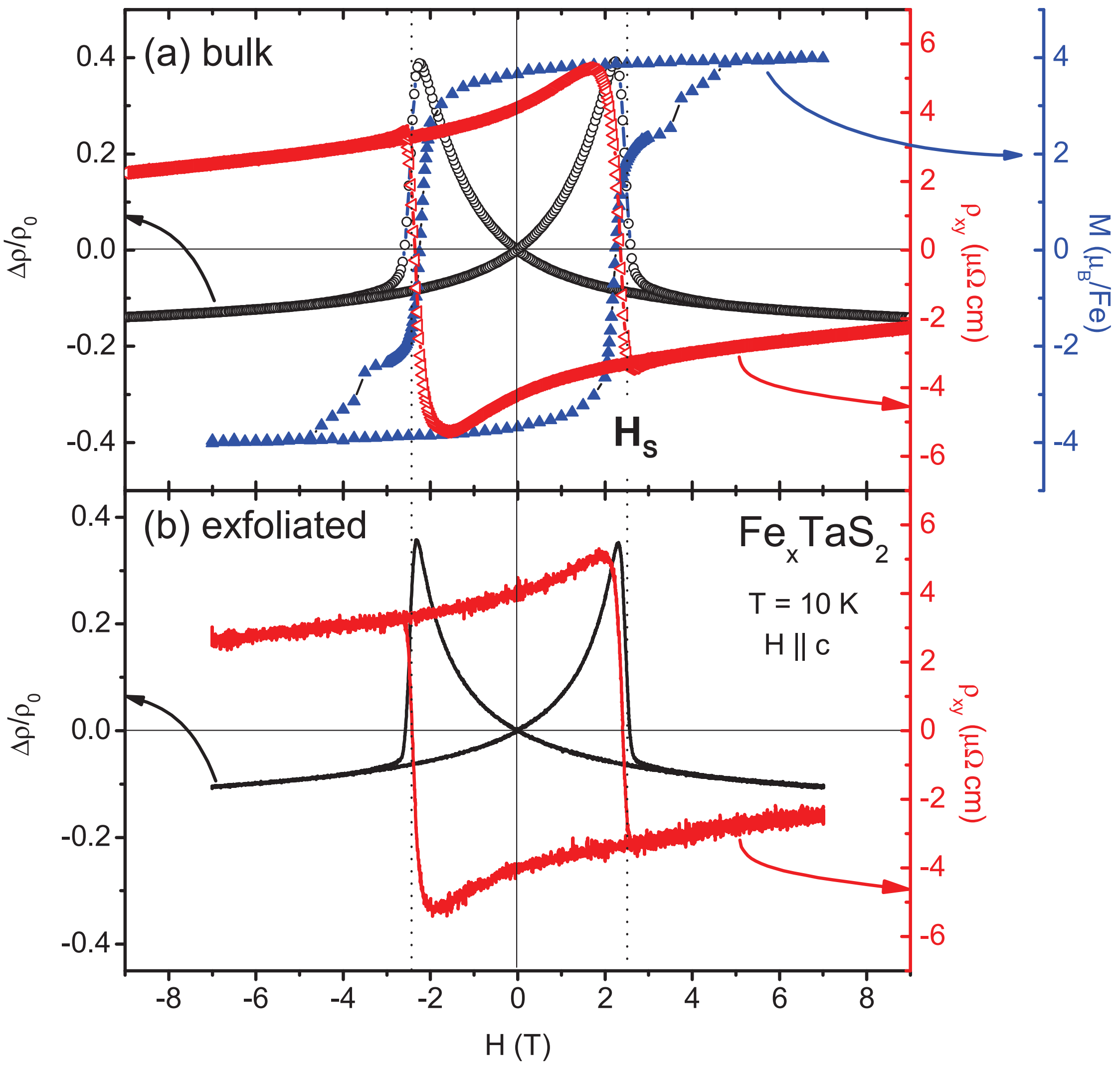

Figure 5.7: **Determination of switching field values of $Fe_{0.28}TaS_2$** Determination of the switching field H_S for (a) bulk and (b) exfoliated samples from $M(H)$ (blue), MR (black) and anomalous Hall resistivity (red). The vertical dashed line marks the switching field H_S, as determined from the field values where $M(H)$ and ρ_{xy} cross H = 0, and where the fastest drop in $\Delta\rho/\rho_0$ occurred. Figure reproduced from [14].

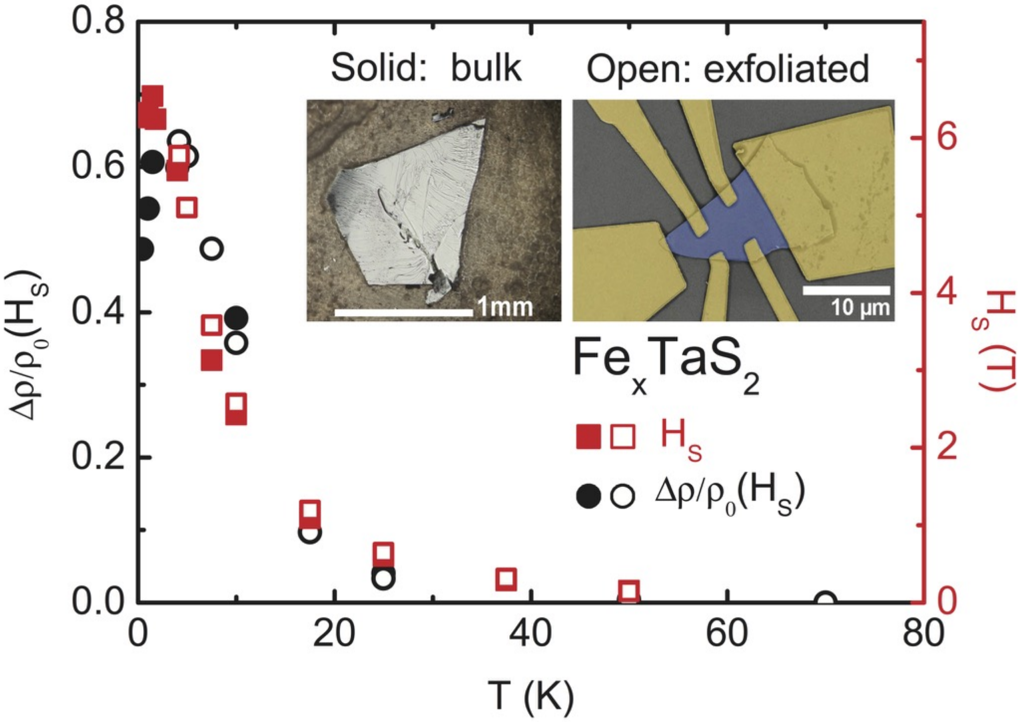

Figure 5.8: **Switching field and MR trends with temperature** Comparison of H_S and magnetoresistivity peak height values as a function of temperature for bulk (solid symbols) and exfoliated (open symbols) samples. H_S increased monotonically with decreasing temperature, while the magnetoresistivity peak height increased with decreasing temperature until 4 K, and then decreased at lower temperatures. Inset: Image of a typical bulk sample (left), and false-color SEM image of a typical exfoliated sample with metal contacts (right). Figure reproduced from [14].

Chapter 6

Thickness-Dependent and Magnetic-Field-Driven Suppression of Antiferromagnetic Order in Thin V_5S_8 Single Crystals

---

Part of this chapter is adapted from the published work [15]:

Thickness-Dependent and Magnetic-Field-Driven Suppression of Antiferromagnetic Order in Thin V_5S_8 Single Crystals

Will J. Hardy, Jiangtan Yuan, Hua Guo, Panpan Zhou, Jun Lou, and Douglas Natelson

ACS Nano **10**, 5941-5946 (2016)

DOI: 10.1021/acsnano.6b01269

As we have now discussed in some detail, with materials approaching the 2d limit yielding many exciting systems with intriguing physical properties and promising technological functionalities, more effort is being devoted to understanding and engineering magnetic order in layered materials. In the previous chapter, we considered a *ferromagnetic* example of such a material, TaS_2 intercalated with Fe; other magnetic ordering configurations are of similar interest in fundamental and applied science, and we now turn our attention to an itinerant $antiferromagnet$ with layered crystal structure.

Here, we consider V_5S_8, a metal with an antiferromagnetic ground state below the Néel temperature $T_\mathrm{N} \sim 32$ K and a prominent spin-flop signature in the magnetoresistance (MR) when $H||c \sim 4.2$ T. We study nanoscale-thickness single crystals of V_5S_8, focusing on temperatures close to T_N and the evolution of material properties in response to systematic reduction in crystal thickness. Transport measurements just below T_N reveal magnetic hysteresis that we ascribe to a metamagnetic transition, the first-order magnetic field-driven breakdown of the ordered state. The reduction of crystal thickness to ~ 10 nm coincides with systematic changes in the magnetic response: T_N falls, implying that antiferromagnetism is suppressed; and while the spin-flop signature remains, the hysteresis disappears, implying that the metamagnetic transition becomes second order as the thickness approaches the 2d limit. This work demonstrates that single crystals of magnetic materials with nanometer thicknesses are promising systems for future studies of magnetism in reduced dimensionality and quantum phase transitions.

6.1 Introduction

The family of two-dimensional materials has grown considerably since the discovery of graphene a decade ago. These 2d materials have demonstrated many exotic and exciting electronic, optical, optoelectronic, mechanical, thermal and catalytic properties.[176, 177, 178, 179] Surprisingly missing from this long list are the 2d magnets that could be critical for spintronics applications and fundamental studies of magnetism at the 2d limit. One strategy proposed is to dope 2d materials with transition metals.[180, 181] Another possible route is to explore the van Hove singularity often found in 2d materials.[182, 183] Layered compounds that possess intrinsic magnetic properties in bulk format such as $CrSiTe_3$ are also proposed to be viable candidates if 2d forms of these materials can be successfully obtained.[184, 185] Despite these early efforts, investigation of 2d magnetism is still in its infancy.

V_5S_8 (also reported as $VS_{1.64}$ or $V_{1.25}S_2$) has a monoclinic NiAs-type crystal structure with space group C2/m (Figure 6.1a, b) and an antiferromagnetic ground state, with $T_\mathrm{N} \sim 32$ K.[186, 187, 188] This material can be relabeled $V_{0.25}VS_2$, to reflect that a fraction of the vanadium atoms are intercalated within the van der Waals gap between VS_2 layers (Fig. 6.1).[189] Early NMR measurements showed that the V sites are not all equivalent [190, 191]; neutron diffraction measurements indicate that the V^I sites (the intercalated V atoms, oxidation state V^{3+}) have localized 3d electrons with local moments at least $\sim 1.1\ \mu_B/V^I$, while the V^{II} and V^{III} sites' 3d electrons are itinerant, resulting in metallicity.[186, 192, 193, 194] Experiments[195] at helium temperatures showed a low-field $H||c$ positive MR sharply switching to negative MR above $\sim$ 4.2 T. While initially modeled as field-induced suppression of AFM order,[193] this sharp feature was identified in bulk samples as the spin-flop transition,[189, 193] with the magnetic easy axis oriented[192, 195] $\sim 10°$away from c toward the a axis. Figure 6.2 shows the magnetic structure of the bulk material and the spin-flopped configuration. Band structure calculations[196] and neutron diffraction[192] estimate a moment $\sim 1.4\ \mu_B/V^I$. Pulsed high-field magnetization measurements[16] found two anomalies in $M(H)$, the spin-flop at $\sim$ 4.5 T and an unknown"distinct hysteresis" at 16.2 – 18.4 T (see Fig. 6.3).

We report magnetotransport measurements on thin single crystals revealing MR hysteresis beginning near zero H just below T_N, with the hysteresis field scale growing dramatically with decreasing T. We surmise that this MR hysteresis is a first-order field-driven transition to a paramagnetic (PM) state. Decreasing thickness down to $\sim$ 10 nm depresses T_N and suppresses the MR hysteresis, while preserving the spin-

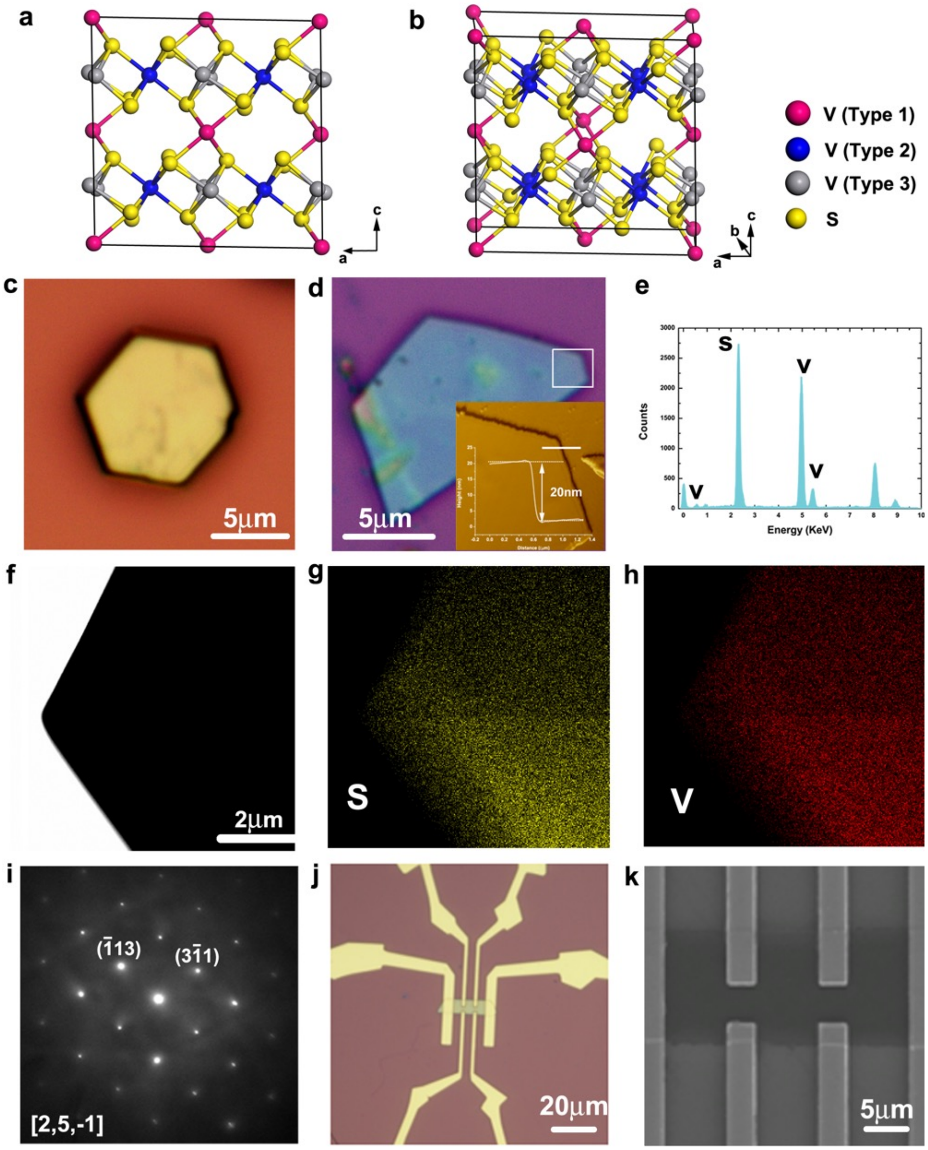

Figure 6.1: **Structure and characterization of thin V_5S_8 crystals and devices.** (a, b), the crystallographic unit cell of V_5S_8. Different colors are used to distinguish three types of vanadium atoms. From the side view along *b* axis in a, V_5S_8 can be considered as intercalating vanadium atoms within the van der Waals gap between layers of VS_2. Optical images of (c) a thick and (d) a thin crystal. Inset of (d) is the AFM height profile which shows the thin crystal has a thickness of about 20nm. (e) EDS spectrum of crystal shown in (f) the brightfield TEM image. EDS peaks for S and V are labeled, while other visible peaks are due to the Cu TEM grid. (g,h) EDS maps of (g) sulfur and (h) vanadium for the crystal in (e), showing a uniform distribution of both elements. (i) SAED pattern of the same crystal along the [2, 5, -1] zone axis, with lattice parameters consistent with V_5S_8. (j) Optical and (k) SEM images of a representative device used for electronic transport measurements (66 nm thick). Figure reproduced from [15].

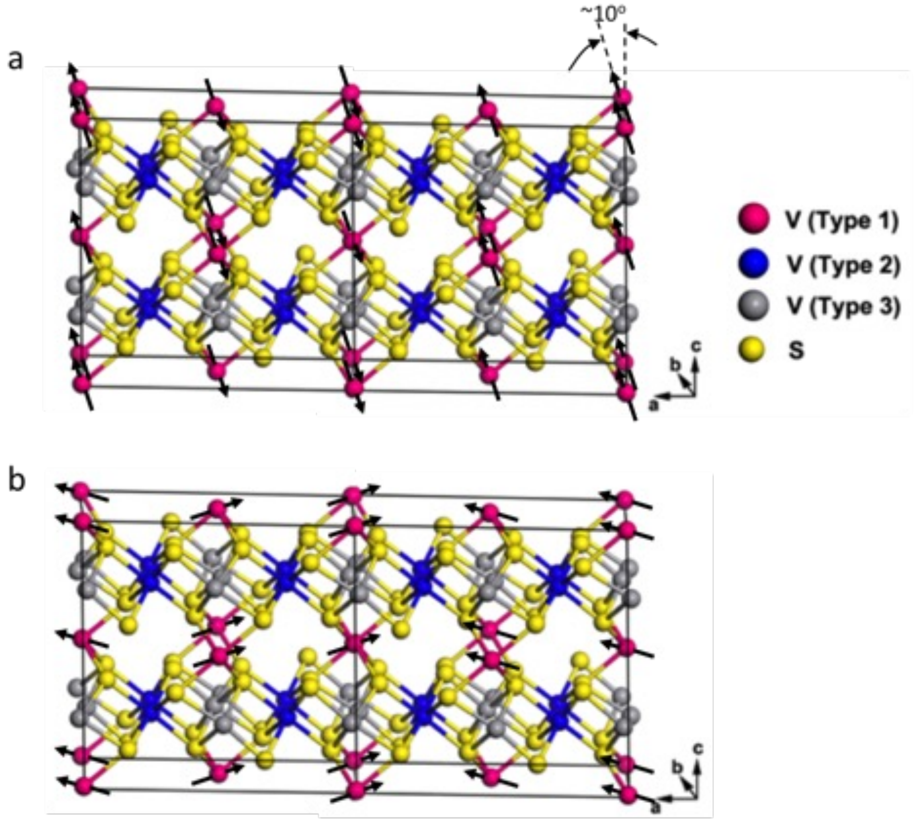

Figure 6.2: **Magnetic structure of bulk V_5S_8 in the AFM state.** (a) The AFM ordered structure in the ordinary Néel state. The magnetic moments are carried by the type-I vanadium atoms. The magnetic easy axis is approximately 10° toward the a axis from the c axis in the $a - c$ plane. (b) The conjectured magnetic structure in the spin-flopped state when a large external magnetic field has been applied along the c axis. Figure reproduced from [15].

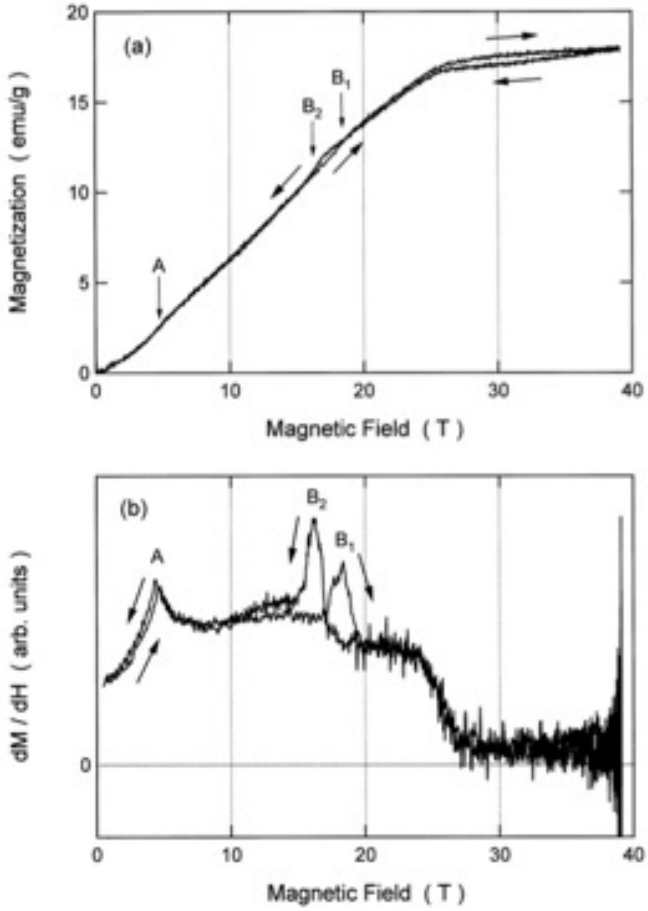

Figure 6.3: **Magnetization hysteresis in V_5S_8.** The low-field feature labeled A, near 4.5 T, is the spin-flop transition. The authors of the study, Nakanishi et al., believe the higher-field hysteresis loop B_2–B_1, in the range 16.2-18.4 T, is magnetic in nature but is otherwise not explained. Figure reproduced with permission from [16]. © 2000 Elsevier.

flop transition. This suggests that reduced dimensionality increases the importance of fluctuations, driving the field-driven transition toward second order and implying the existence of a field-driven quantum phase transition. These investigations show that thin crystals grown by chemical vapor deposition (CVD) are powerful tools for examining magnetism and phase competition in reduced dimensionality.

6.2 Methods

Single crystals were grown using CVD by Jiangtan Yuan, under the supervision of Prof. Jun Lou, on 300 nm SiO_2/Si wafers, with lateral crystal dimensions ranging from a few microns to a few tens of microns, and thicknesses from $\sim$ 10 nm to $\sim$ 1 um. Vanadium trichloride (VCl_3) was used as a precursor (Sigma-Aldrich, 97%, powder). An Al_2O_3 crucible with around 0.1 g of VCl_3 was placed in a quartz tube with diameter of 1 inch at the center of the heating zone of the furnace, and a SiO_2/Si substrate was placed on top of the crucible with oxide surface facing down to collect the final product. Sulfur (1g) was put in the upstream of the tube (Sigma-Aldrich, reagent grade). A mixture of N_2 with 10% of H_2 (99.999%) was used as carrier gas at ambient pressure. The center of the furnace was gradually heated from room temperature to 750 °C in 25 min at a rate of $\sim$ 20 °C /min. After 10 minutes at this temperature, the carrier gas was changed to pure N_2 (99.999%) and the furnace was naturally cooled down to room temperature. Thin crystals are usually formed near the edge of growth substrate.

I then defined metal contacts on the as-grown crystals by a standard procedure of e-beam lithography, e-beam evaporation of Au with a V adhesion layer, and liftoff. For relatively thick samples, an additional step to deposit extra Au (40 nm) by dc sputtering was included between the e-beam evaporation and liftoff steps in order to ensure that the electrodes had continuous metal coating over the crystal side walls.

Both J. Yuan and I characterized the completed devices using optical microscopy, scanning electron microscopy (SEM) and atomic force microscopy (AFM), as shown in Fig.1. Transport measurements were performed using four-probe low frequency lock-in methods in either a Quantum Design Physical Property Measurement System (QD PPMS) equipped with a 9 T superconducting magnet or a QD Dynacool PPMS equipped with a 14 T superconducting magnet (which belongs to the group of Prof. Emilia Morosan; measurements in this system were performed with assistance from Binod Rai). For some measurements, a QD horizontal rotator apparatus was employed to change the relative direction of the applied magnetic field with respect to the sample axes.

6.3 Results and Discussion

Thick, shiny, yellow crystals with hexagonal or half hexagonal shapes, expected for the C2/m symmetry of V_5S_8,[196] are the most common CVD synthesis products (Fig. 6.1c shows an optical micrograph of a representative sample). Very thin crystals (as thin as $\sim$ 10 nm) also form, appearing light blue or purple on the growth substrate (Fig. 6.1d). Figure 6.1d's inset shows the AFM height profile of the pictured crystal with thickness $\sim$ 20 nm. J. Yuan and H. Guo confirmed the structure and composition of the V_5S_8 crystals via energy dispersive X-ray spectroscopy (EDS) and electron diffraction. (Figure 6.1e-i). The crystal structure is identified by acquiring selected area electron diffraction (SAED) patterns at various crystal tilts. The derived lattice parameters (a = 11.375 Å, b = 6.648 Å, c = 11.299 Å) are consistent with those of V_5S_8. Figures 6.1j and k are the optical and SEM images of a typical crystal prepared with electrodes.

Temperature-dependent resistivity, ρ (T), measured from 2–300 K(solid lines in Fig. 6.4, normalized to T = 300 K value) is consistent with metallic conduction and agrees well with prior measurements of a large bulk single crystal of V_5S_8,[186] with room temperature resistivity of a few hundred $\mu\Omega$-cm. Upon cooling, a broad decrease in resistivity is observed, centered at $\sim$ 100 K; with further cooling a kink appears, marking $T_{\rm N}$, whose sharpness and value decrease with decreasing sample thickness. This sharp resistivity drop is attributed to reduction of spin fluctuations upon antiferromagnetic ordering[197]. The resistivity ratio ρ(300K)/ρ(2K) falls with decreasing sample thickness, likely due to enhanced interface scattering at small thickness. Plotting dρ/dT as a function of temperature (Fig. 6.4, open red circles) allows more accurate determination of the transition temperature, in the range of 22–32 K for different thicknesses, with $T_{\rm N}$ decreasing monotonically with thickness. In the thinnest samples ($\sim$ 10 nm), an upturn in resistivity is observed below $\sim$ 10 K, which may be a sign of localization. There is no evidence of temperature hysteresis upon subsequent warming.

For comparison with the temperature dependent resistivity data for the 66 nm thick sample, additional plots are shown in Fig. 6.5 of the resistivity and its derivative dρ/dT as a function of temperature for the 11, 12, 24, and 345 nm thick samples. Vertical gray dashed lines mark the position of $T_{\rm N}$ at the peak of dρ/dT. The 11 and 12 nm thick samples have a subtle resistivity kink at the transition temperature, whereas the corresponding kink for the thicker samples is sharper and more pronounced. The 11 nm sample shows a negative slope of resistivity at high temperatures, possibly due to contact issues, while the data below $\sim$150 K looks very similar to the curve for the 12 nm thick sample. The resistivity curves for both 11 and 12 nm thick samples show an upturn in resistivity at temperatures below $\sim$ 10 K.

The overall variation in magnitude of resistivity among the samples may be due to slight variations in crystal stoichiometry, as well as estimation of the sample dimensions from SEM and AFM images of the hexagon shaped samples, the geometry of

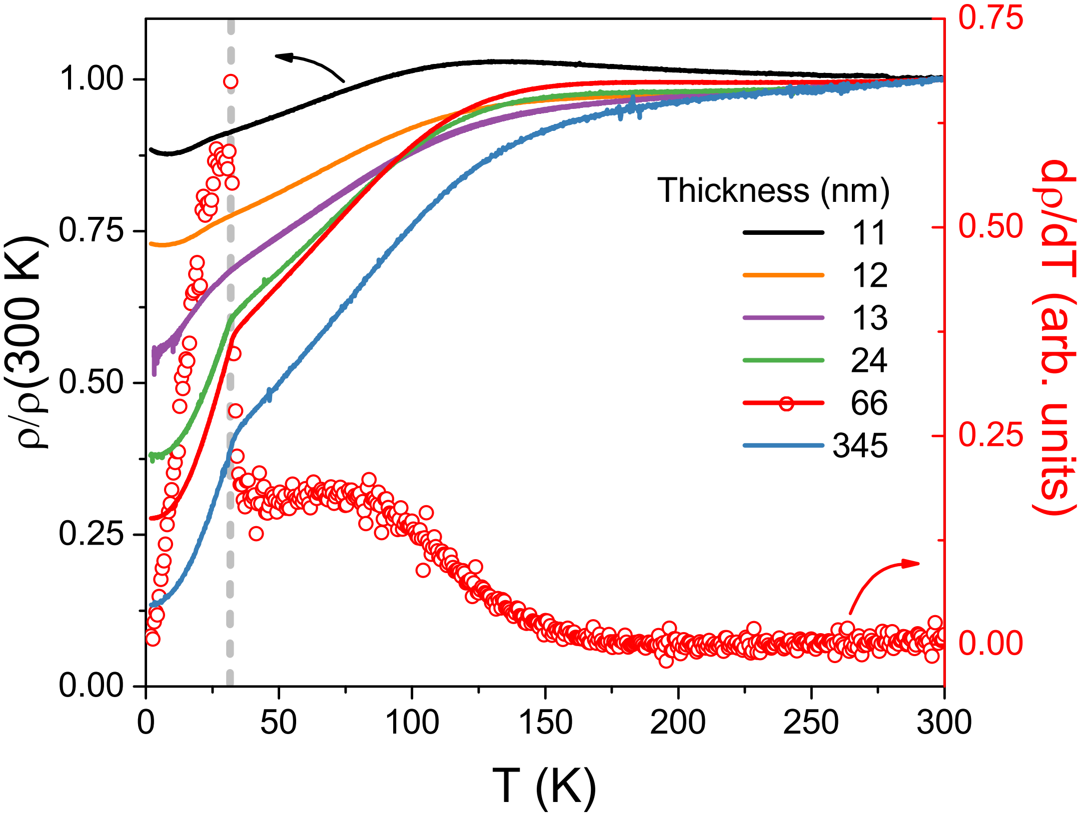

Figure 6.4: **Temperature dependent resistivity.** Resistivity normalized to T = 300 K value for several crystal thicknesses (solid lines, left axis) and calculated derivative dρ/dT (open red circles, right axis) of a 66 nm thick crystal as a function of temperature . The sharp kink in resistivity and corresponding peak in dρ/dT at $\sim$ 32 K mark T_{N} for the 66 nm sample. Figure reproduced from [15].

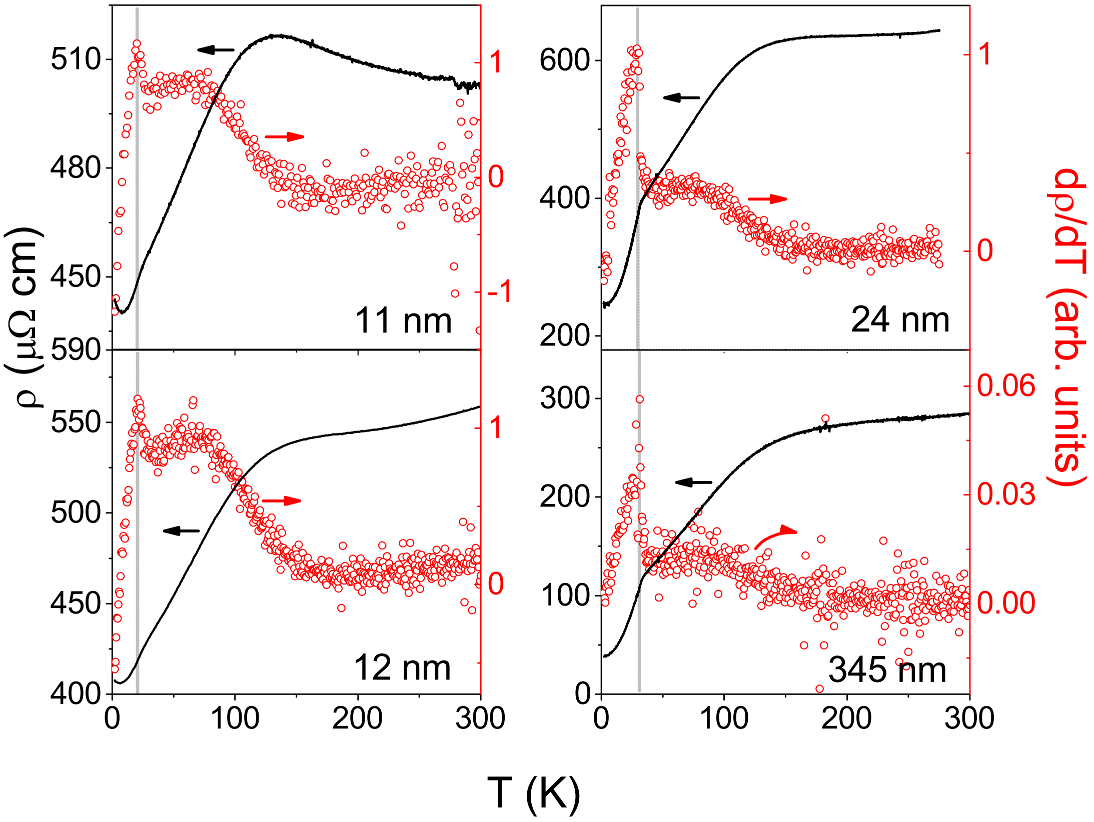

Figure 6.5: **Determination of T_N for additional crystal thicknesses.** (Left axis, black solid lines) Resistivity and (right axis, open red circles) calculated derivative dρ/dT as a function of temperature for the 11, 12, 24, and 345 nm thick samples. The dashed gray lines mark T_N. Figure reproduced from [15].

which makes proper estimation of lateral dimensions somewhat challenging. We note that the fractional change of resistivity relative to its value at $T = 300$ K is larger for thicker samples, which may be either an indication of higher quality of thick crystals or of other thickness dependent effects (*e.g.*, surface scattering).

In Fig. 6.6, we plot the thickness dependence of the Néel temperature T_N as determined from the position of the peak of $\mathrm{d}\rho/\mathrm{dT}$ vs. T. A systematic reduction of the transition temperature from its large-thickness saturation value is visible as the thickness is decreased ($\sim$ 32 K for the 66 nm and 345 nm thick samples; $\sim$ 31 K for the 24 nm sample; $\sim$ 22 K for the 11 and 12 nm thick samples). An estimated error of $\sim \pm 1$ K in determining T_N results from both the width of the transition as well as noise in the calculated $\mathrm{d}\rho/\mathrm{dT}$ vs. T curves.

Small crystal size makes it very difficult to directly probe antiferromagnetic order in situ. Neutron scattering requires far larger sample mass to produce detectable signals. Combining a technique like x-ray magnetic linear dichroism (XMLD) with photoemission electron microscopy (PEEM) at cryogenic conditions is extremely challenging (see Fig. 6.7). Fortunately, the distinct spin-flop MR features reported in the prior work on bulk V_5S_8 give us access to some of this information. We focused on temperatures just below T_N, with H oriented either perpendicular or parallel to the ab plane. The MR is defined here as $\Delta\rho/\rho = [\rho(H) - \rho(0)]/\rho(0)$. We find sharp, nontrivial MR features appearing only below T_N, and in Figure 6.8 present two families of curve shapes for samples of different thickness (24, 66, and 345 nm thicknesses are the first type; 11, 12, and 13 nm thicknesses are the second).

Two relatively thick, simultaneously grown samples, $\sim$ 66 nm and $\sim$ 345 nm thick, display a strikingly hysteretic and anisotropic series of MR responses with H either perpendicular or parallel to c. The 66 nm thick sample's pronounced MR hysteresis appears just below $T_\mathrm{N} \sim 32$ K (Fig. 6.8a). With H$||c$, the MR shows

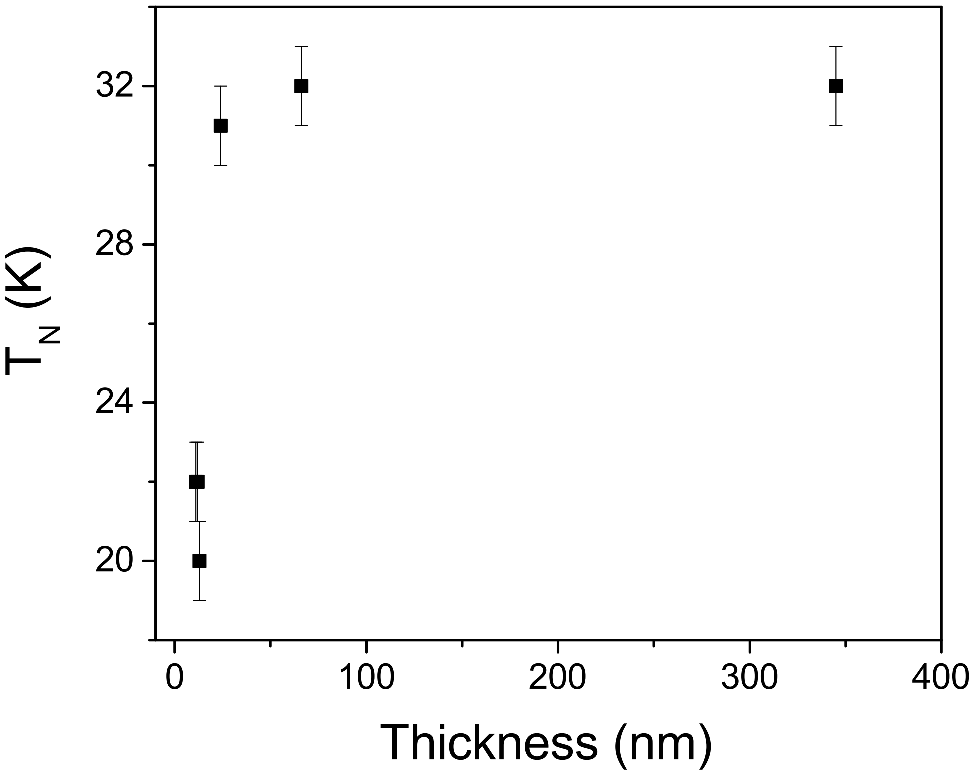

Figure 6.6: **Crystal thickness dependence of T_{N}.** A saturation value of ~ 32 K is observed for the thickest samples. Figure reproduced from [15].

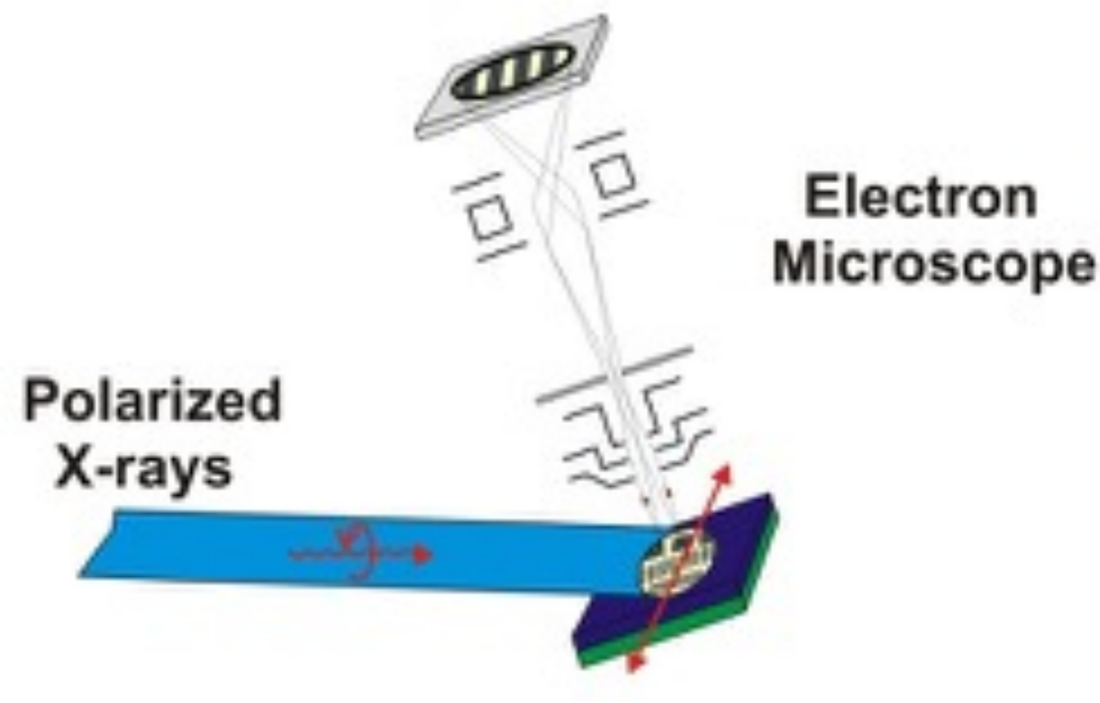

Figure 6.7: **Schematic diagram of x-ray magnetic dichroism + PEEM technique.** Use of linearly polarized x-rays makes the technique sensitive to AFM order, while circularly-polarized x-rays would be useful for imaging FM order. Figure reproduced with permission from [17].

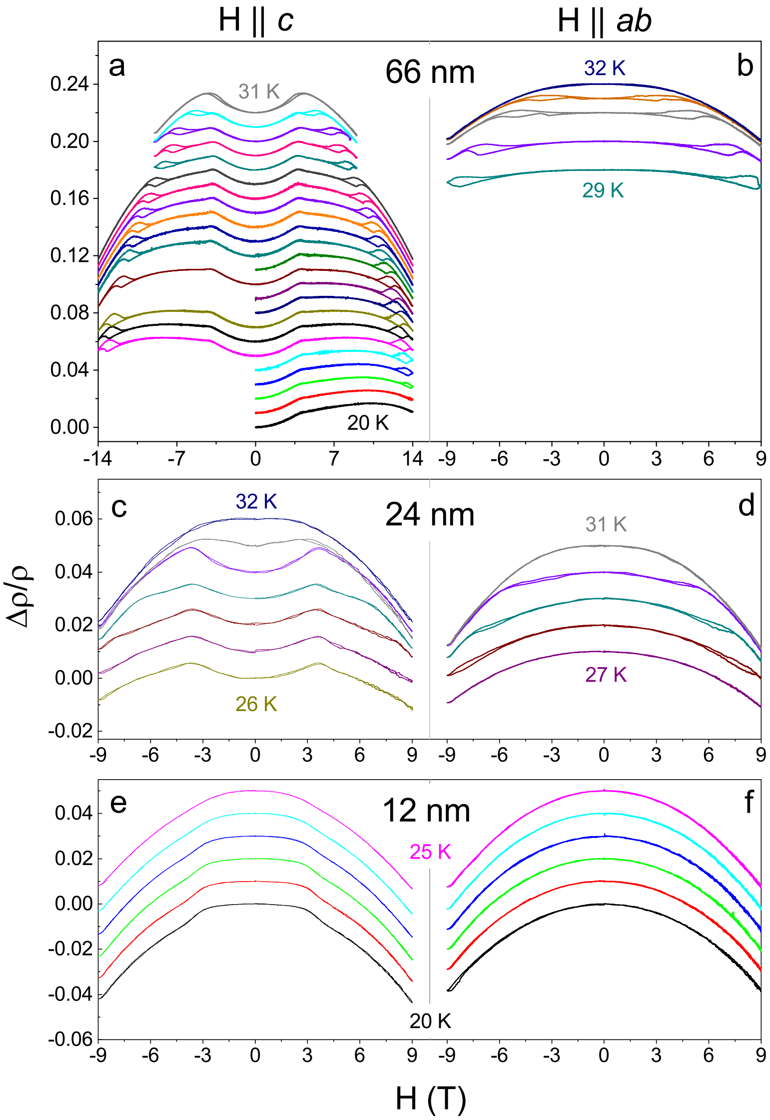

Figure 6.8: **Magnetoresistance at various crystal thicknesses:** Magnetoresistance curves at selected temperatures for three different crystal thicknesses, with H||*c* (left column) or H||*ab* (right column). Curves at different temperatures are offset for clarity, with the offset in the left and right column plots matching for curves at the same temperature. Note that for panel (a) the field scale is 14 T, rather than the 9 T scale of the other panels. (a,b) MR measurements for the t = 66 nm sample focusing on the temperature range 20–32 K (curves offset by 0.01 per 0.5 K) to demonstrate the evolution of hysteresis, with hysteresis loops shifting to higher fields with decreasing temperature. The peaks near 4 T in the H||*c* curves are due to the spin flop transition, whereas the H||*ab* curves are negative over the entire field range. (c,d) MR curves for the t = 24 nm sample from 26–32 K (curves offset by 0.01 per 1 K above 26 K). The H||*c* curves show no hysteresis but otherwise have qualitatively similar features to those observed for thicker samples. Hysteresis appears when H||*ab*. (e,f) MR curves for the t = 12 nm sample in the temperature range 20–25 K (curves offset by 0.01 per 1 K above 20 K). With H||*c*, a smooth and gradual development of kinks is visible near H ∼ 3 T as the temperature is decreased, but no hysteresis is observed. With H ||*ab*, the curves are smooth and without kinks or discernible hysteresis. Figure reproduced from [15].

the sharp spin-flop downturn at ~ 4 T. Hysteretic MR over a limited H range is observed for temperatures near T_{N}. For example, at T = 30 K, the MR hysteresis loop extends from ~ 5 T to ~ 7 T, with the MR retracing itself outside that field range. The hysteresis quickly shifts to much higher fields as T is reduced. Hysteresis is no longer visible below ~ 20.5 K, having presumably shifted beyond the 14 T limit of our magnet, as suggested by magnetization data at helium temperatures.[192] The sense of the hysteresis is that the resistance is lower on increasing magnitude of field than when sweeping from high field toward zero. In order to check for any effects of the magnetic field ramping rate, selected MR curves were measured using different field sweeping rates (either 25 Oersted/s or 50 Oersted/s), with no discernible differences in the results. Sweep rates are limited to relatively slow speeds to avoid any complications from eddy current heating and the strong temperature dependence of the MR. To augment the data taken for the 66 nm crystal close to T_{N}, MR curves over a wider temperature range are shown in Fig. 6.9, along with Hall resistivity data at corresponding temperatures. MR and Hall data for the 345 nm crystal are also shown in Fig. 6.11.

When the magnetic field is instead applied in the *ab* plane, the low-field sign of the 66 nm crystal's MR remains negative over the whole field range, with no sharp features (Fig. 6.8b), consistent with the spin-flop interpretation of the sharp MR feature in the H$||c$ data.[192] Hysteretic MR of comparable magnitude is observed with H$||ab$, at the same field ranges as the H$||c$ case. This implies that the hysteresis is a first-order field-driven phase transition, driven by magnetic tuning of the relative free energies of the AFM and PM states; alternate explanations involving, *e.g.*, domains within the material would be expected to depend strongly on field direction due to geometric and crystallographic anisotropies. The 345 nm thick sample shows quantitatively similar hysteresis below $T_{\mathrm{N}} \sim 32$ K, though the signal-to-noise is worse (Fig. 6.11) because of the thicker sample's very low four-terminal resistance ($\sim 1\ \Omega$).

A third, considerably thinner sample, 24 nm thick and grown independently from the two thicker crystals, has MR curves with $H||c$ below $T_{\mathrm{N}} \sim 31$ K (Fig. 6.8c) qualitatively similar to those of the 66 nm and 345 nm samples, but without discernible hysteresis. Minor $R(H)$ variation likely results from slight temperature drift and/or contact resistance noise, but any true MR hysteresis is too small to detect. In contrast, the $H||ab$ measurement on the 24 nm sample shows monotonic negative MR and clearly resolved hysteresis (Fig. 6.8d), very similar to what was observed for the 66 nm sample. This intermediate thickness value demonstrates gradual evolution of the MR properties from thick to thin samples.

For a group of still thinner samples (11, 12, and 13 nm thick samples measured; 12 nm data shown in Fig. 6.8, and 11 nm in Fig. 6.10) with $H||c$, the low temperature MR is fairly flat at small fields, but with increasing field the spin-flop kink begins at ~ 3 T and the MR (a few percent) is negative (see Fig. 3e). For these thin samples T_{N} is suppressed – for the sample shown ($\mathrm{d}\rho/\mathrm{d}T$ gives $T_{\mathrm{N}} \sim 22 \pm 1$ K) the spin-flop kinks are still visible at 23 K and disappear with increasing temperature. At 25 K and above, the MR is more nearly parabolic and without kinks, gradually flattening as the temperature is increased toward 100 K. When $H||ab$, smooth MR curves without kinks are recorded in the range 20 – 25 K (Fig. 3f). The flat (rather than positive) MR in the low field range for thin samples may be due to a relatively stronger contribution of spin disorder to the zero-field resistivity, weakening the contribution of the spin-flop effect to the MR.

These results demonstrate two features of V_5S_8 that were not explained in the prior literature: Field driven first-order breakdown of the AFM state, resulting in MR hysteresis, and thickness dependent suppression of the AFM state as the thickness approaches 10 nm. There are several examples of field-driven metamagnetic

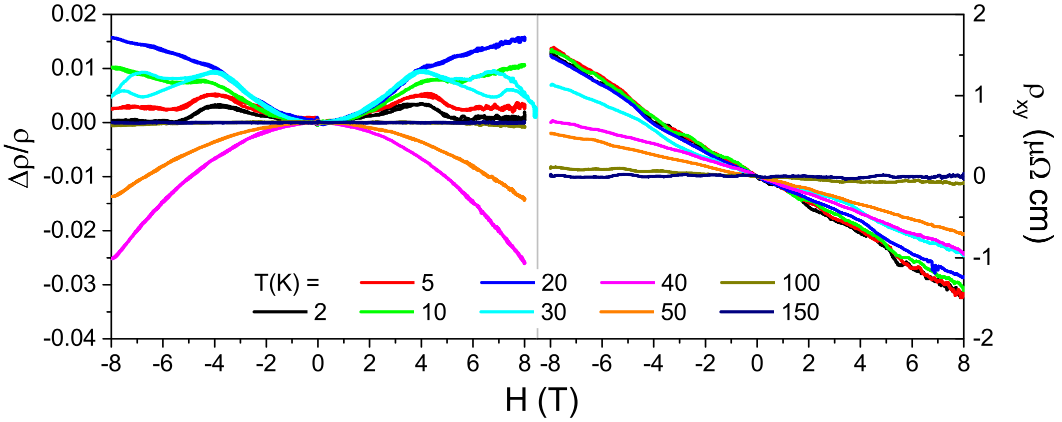

Figure 6.9: (Left) H$||c$ MR isotherms for the 66 nm thick sample at selected temperatures in the range 2 –150 K. (Right) Hall resistivity data for the same sample at corresponding temperatures. Figure reproduced from [15].

transitions involving the breakdown of an AFM state, as in the rare earth containing systems $Nd_{0.5}Sr_{0.5}MnO_3$,[198] DySb,[199] and DyCuSi and HoCuSi.[200, 201] In the case of $Nd_{0.5}Sr_{0.5}MnO_3$, application of a magnetic field up to 12 T at low temperatures causes the insulating AFM state to break down to a metallic FM state, accompanied by a drop in resistivity of more than five orders of magnitude.[198] Alternatively, a metamagnetic transition can occur between AFM and PM order, as in the case of $CeAuSb_2$, where hysteretic MR measurements suggest a first order transition. This material is therefore thought to be very near to a quantum critical point (QCP).[202] While it is conceivable that the hysteresis is an indicator of some other ordered state (*e.g.*, charge density wave), this is unlikely given the lack of any previous evidence for competing order or magnetoelectric effects in this material.

The observed thickness dependence could be intrinsic or extrinsic. Confinement can affect the itinerant carriers, as seen in the thickness-dependent ρ(T), potentially impacting exchange processes. The effects of uncompensated surface spins may also be at play,[203] due to a possible lack of perfect AFM order at the crystal surfaces, which would be more important in crystals of reduced thickness. Thinner crystals are more strained due to their elastic interactions with the underlying substrate.

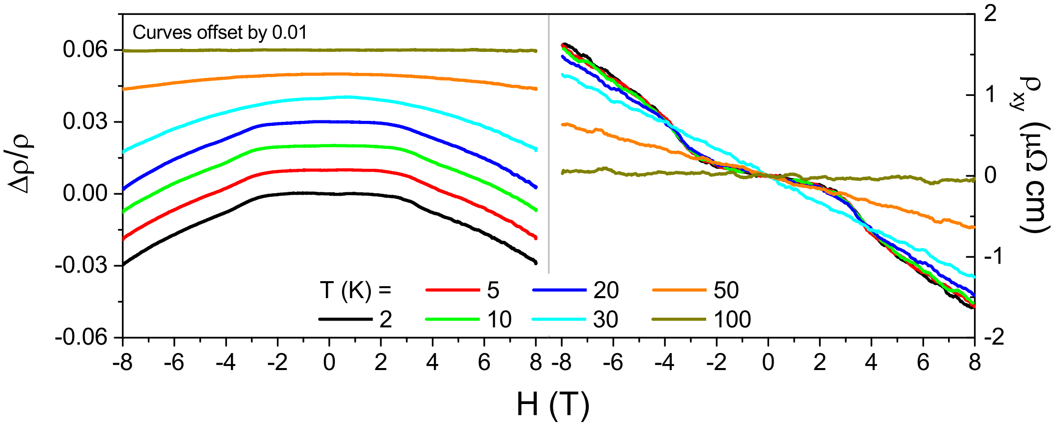

Figure 6.10: (Left) $H||c$ MR isotherms for the 11 nm thick sample in the temperature range 2 – 100 K. Curves are offset by 0.01 for clarity. (Right) Hall resistivity data for the same sample. Figure reproduced from [15].

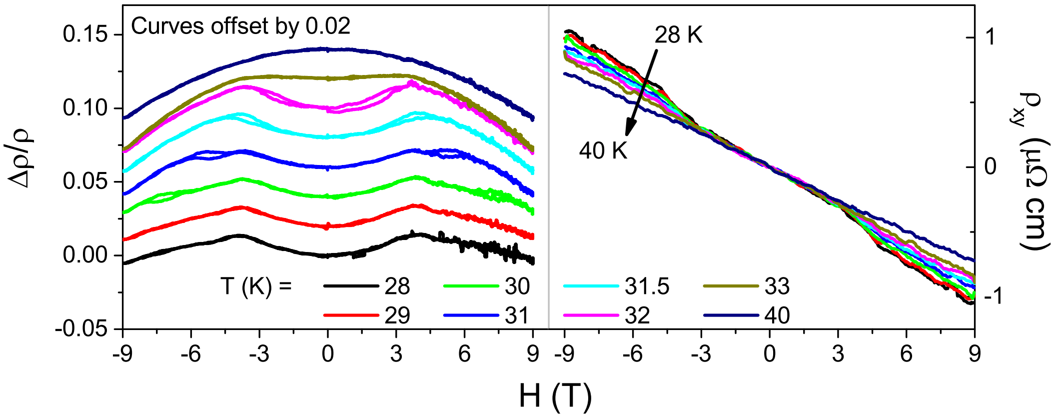

Figure 6.11: (Left) $H||c$ MR isotherms for the 345 nm thick sample in the temperature range near T_{N} from 28–40 K. Curves are offset by 0.02 for clarity. (Right) Hall resistivity curves for the same sample at corresponding temperatures. Figure reproduced from [15].

Stoichiometry could also be a concern, though there is no evidence of systematic variation of V:S ratio with thickness.

Combining resistivity and MR information, we construct a tentative phase diagram using temperature and critical field values (Fig. 6.12). Each filled data point is taken from an MR isotherm such that the point's x-axis position represents the central value of a MR hysteresis loop at a given temperature (scaled by T_{N}), and the horizontal bar represents the hysteresis loop width. Data for the 345 nm and 66 nm samples were extracted from H$||c$ measurements, while for the 24 nm sample, which displayed no apparent H$||c$ hysteresis, the data points were taken from the hysteretic H$||ab$ MR curves. Since our maximum field strength was 14 T, data points at the lower end of the temperature range have horizontal bars limited by the accessible field. These phase assignments are based on the appearance of the previously reported spin-flop kink in the MR, with PM as the logical competing phase based on the onset of the metamagnetic transition at T_{N}, as there is no direct technique available to probe in situ AFM order in these very small samples.

The plot's useful range can extend to lower temperatures by including the single high-field data point at $T = 4.2$ K from $M(H)$ measurements on a bulk polycrystalline sample,[16] presuming that this $M(H)$ hysteresis results from the same AFM breakdown phenomenon as our MR hysteresis close to T_{N}. Fig. 6.12 implies a AFM/PM quantum phase transition at zero temperature and finite magnetic field value $H_{\mathrm{C}}(0)$, which can be estimated by fitting: $H_{\mathrm{C}} = H_{\mathrm{C}}(0)\times(1\text{-}T/T_{\mathrm{N}})^{\alpha}$. The fit yields an estimate of $H_{\mathrm{C}}(0)$= 18.7 T and an exponent $\alpha = 0.345$, which deviates from the value of 1/2 previously seen in other antiferromagnets.[18, 19]

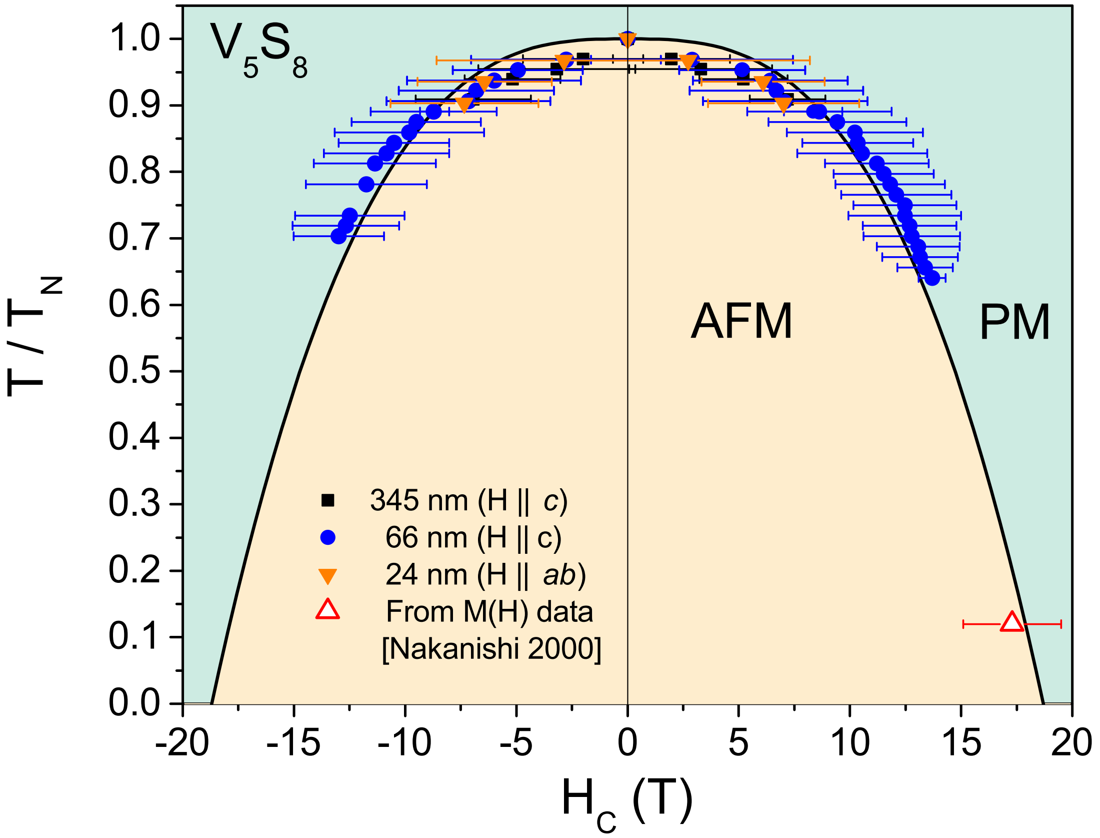

Figure 6.12: **Suggested magnetic phase diagram for V_5S_8:** Temperature-magnetic field phase diagram of V_5S_8. Filled symbols represent the central values H_C of MR hysteresis loops extracted from the data sets of three devices (H ⊥ plane for 345 nm and 66 nm samples, and H || plane for 24 nm sample), and corresponding horizontal bars represent the width of those hysteresis loops. The open red triangle represents one data point from high field magnetization measurements [Funahashi *etal.*, 1981] at T = 4.2 K. The solid line is a fit inspired by a functional form used previously in the field-driven breakdown of AFM order in the $CeIn_3$ system [18, 19]. Figure reproduced from [15].

6.4 Conclusions

The field-driven breakdown of the AFM state implies the existence of a quantum phase transition at accessible fields in this material as T → 0. These studies also suggest a suppression of antiferromagnetism with reducing thickness, although even very thin crystals (∼ 10 nm) maintain some AFM signatures (spin flop kinks in the

H$||c$ MR). Given the suppression of T_{N} in the thinnest crystals, it is unlikely that the metamagnetic transition is absent in those samples, even without its clearest evidence (the hysteretic MR). The disappearance of MR hysteresis as thickness is reduced suggests that the metamagnetic transition changes from first order to second order. This would imply possible quantum critical phenomena at appropriately large field scales, though these have not yet been examined. Further experiments at higher fields and lower temperatures (*e.g.*, noise/resistance fluctuations; magneto-optic response; XMLD with PEEM) are called for and beyond the scope of the present work. While very challenging to implement, XMLD with PEEM in situ in the magnetic field regime of the observed metamagnetic transition could potentially examine the hysteretic state (*e.g.*, domains and phase separation) and its evolution with thickness. The rich phenomenology seen in the V_5S_8 system toward the 2D limit strongly suggests that CVD growth of other magnetically ordered, layered materials will enable insights into the competition between electronically and magnetically ordered phases in reduced dimensionality.

Chapter 7

Closing Remarks

The work presented in this thesis demonstrates that electronic transport measurements made on nanoscale and microscale dimensions can give powerful insights into the electronic and magnetic properties of strongly correlated materials. This approach owes much of its success to its intrinsic simplicity – quantities such as resistance or conductance are readily assessed with fairly straightforward tools – coupled with the fact that the quantities probed in transport are intimately tied to the electronic structure, which has deep importance in tipping the balance between distinct physical states (metal vs. insulator, magnetic ordering, thermoelectric properties,...). The topics discussed in this thesis, such as bad metallicity, transport in oxide quantum wells, and magnetism imparted to layered materials via intercalation, are all examples where nanoscale electronic transport measurements can shed new light on the electronic and magnetic properties of SCMs. It can be anticipated that as other new correlated materials are synthesized, whether bulk materials that are later reduced to nanoscale dimensions, crystals grown with nanometer-scale thickness, or artificially engineered heterostructures grown one atomic layer at a time, nanoscale transport measurements will be fruitfully applied in the search for a better understanding of these new systems.

7.1 Outlook for Future Work

Related transport probes beyond the simple ones discussed already are also available for application to strongly correlated material research, and additional work is already underway in the Natelson group. One option that may yield particularly useful insights is the study of *shot noise*, which is a type of non-equilibrium noise present in electronic measurements beyond the well-known Johnson-Nyquist (thermal) noise and ubiquitous $1/f$ noise. Shot noise results from the fact that electric current is a flow of discrete charge carriers rather than a continuous medium, and fluctuations about the average current must be in multiples of the effective quasiparticle charge. Measurements of shot noise have been used, for example, to examine the pairing of individual electron-like carriers into composite Cooper pairs in superconductors, which is reflected by an additional factor of 2 that appears in the expected shot noise intensity.[204]

Because shot noise is obscured through ensemble averaging and electron-phonon energy transfer in macroscopic conductors, special measurement arrangements are necessary for its observation. Appropriate configurations include atomic-scale metal contacts and tunnel junctions. Regarding the former, the Natelson group has conducted a number of studies using metallic atomic break junctions prepared by three techniques: electromigrating metal nanowires,[205] repeatedly pressing a sharp gold tip into a gold film surface and then pulling it away,[206, 207, 208, 209] and flexing lithographically prepared metal nanowires to the breaking point. [210, 175] An important advantage to all these configurations is the ability to simultaneously measure conductance along with the (bias-dependent) shot noise. This is accomplished by applying a square-wave voltage bias at kHz frequencies while using a lock-in to record the difference in noise power between finite square-wave bias and zero bias. Filters are used to selectively measure noise over a bandwidth in a range of several hundred MHz (which essentially removes the $1/f$ noise contribution). In each case, the quantization of conductance can be observed as the contact becomes very small, reducing the number of available quantum channels for transmission; the shot noise is found to be minimized at these ‘preferred’ integer values of conductance in units of $2e^2/h$.

In SCM systems, it is not clear that the shot noise should have the same well-understood properties as simple junctions of good metals like Au. For example, one could imagine that the electron-electron correlations would result in a more orderly, more even temporal spacing of charge carriers being transmitted from one side of a junction to the other, resulting in reduced shot noise compared to the uncorrelated case.

The break-junction technique, however, is not easily adapted to SCMs, as they are often found to be fragile, not flexible, not malleable, and easily damaged by the high current densities of electromigration. Tunnel junctions could provide an alternate route to shot noise measurements in SCMs. One limitation is that conventional fabrication procedures for preparing tunnel junctions include steps that are too harsh for many correlated materials (baking, etching, dielectric deposition, and so on), particularly for materials that either oxidize or change oxidation state easily. As a way around this, my colleague Panpan Zhou has been developing a method of preparing high quality tunnel junctions, which will likely to be compatible with a wide variety of correlated materials. Zhou’s method makes use of a carefully placed, atomically thin sheet of hexagonal boron nitride (h-BN) as the tunnel barrier, which can be sandwiched between the two leads of the tunnel junction. This arrangement could consist of a typical metal on one side of the tunnel barrier and an SCM on the other, or SCMs on both sides. Analogous in structure to graphene, h-BN is a large-gap crystalline insulator that can be thinned down to a single atomic layer by micromechanical exfoliation, can have low defect density, and is essentially chemically inert. Zhou's initial work has focused on mastering the technique of exfoliating and transferring thin layers of h-BN, constructing an appropriate RF-compatible measurement insert for the PPMS, and characterizing Au/h-BN/Au junctions, and the resulting paper was recently published in *Appl. Phys. Lett.* [211] As a first attempt at applying this technique to a correlated material, Zhou and visiting undergraduate student Chenyuan Li have conducted preliminary trials using Au/h-BN/VO_2 junctions. An improved measurement apparatus is also in the works, including low-temperature signal amplification for an improved signal-to-noise ratio. The general idea of studying correlated materials by tunneling methods seems extremely viable as a path to new information, and the outlook for using h-BN as a universally applicable tunnel barrier in such studies looks similarly promising.

Chapter 8

Appendix A: Modification of the Charge Density Wave Transition in $TiSe_2$ *via* Hydrogenation

---

This appendix contains unpublished work performed by:

Will J. Hardy, Heng Ji, Justin Chen, Maxim Dalton, Emilia Morosan, and Douglas Natelson

In this Appendix, my goal is to provide a useful reference for continuation of a line of inquiry, toward which we have performed preliminary experiments. We explored the feasibility of hydrogen intercalation in the layered transition metal dichalcogenide (TMD) $1T$-$TiSe_2$. Initial results indicate that this is possible, with evidence of suppression of the pristine material's charge density wave transition along with an increase of n-type carrier density. Further experiments would be useful in understanding this phenomenon in more detail, and one could consider applying this technique to additional layered material systems.

8.1 Introduction

The layered TMD $TiSe_2$ has been the subject of decades of study, primarily due to its famous charge density wave (CDW) transition, in which a periodic spatial modulation of charge density sets in below ~ 165 K [212]. The temperature-dependent resistivity shows a peak near 165 K due to the CDW transition. In terms of electronic properties, there is disagreement whether $TiSe_2$ is properly classified as a semiconductor [213] or rather a semimetal with a small band overlap [214, 215]. Approximately equal (low) n- and p-type carrier concentrations ($\sim 10^{20}/\mathrm{cm}^3$) results in a somewhat high resistivity and small magnetoresistance.[212]

Modification of the CDW state has previously been achieved in $TiSe_2$ through the intercalation of Cu [216, 217] and Pd [215], both of which are observed to increase carrier density and even induce superconductivity at certain intercalation levels. A continuous transition from suppression of the CDW state to the onset of superconductivity is visible in transport data. In these intercalated compounds, the Cu or Pd atoms sit between the layers of the $TiSe_2$ lattice, within the van der Waals gap. In the case of Cu intercalation, each Cu atom donates one electron to the conduction band [216]; in the Pd-intercalated compounds, the situation is reported to be more complex, with the electronic properties evolving in a non-monotonic fashion as the doping concentration is increased, from an insulating ground state at low doping, to a superconducting ground state for a doping fraction $0.11 \leq x \leq 0.12$, to a normal metal. [215]

As an alternative to doping with transition metals, we consider whether intercalation of hydrogen in layered materials may have useful benefits. Upon doping a TMD compound with hydrogen, a crude assumption would be that each hydrogen atom donates one electron to the conduction band, while causing minimal structural distortion to the crystal lattice. This should mean that the resistivity of the doped compound becomes progressively lower as the hydrogen concentration x increases. On the other hand, Takabatake *et al.* report that in the high-T_C copper oxide superconductors YBCO, BSCCO, and BPSCCO, intercalation of hydrogen can instead have the opposite effect of diminishing superconductivity [218], though these are hole-doped conductors prior to hydrogen exposure. In these materials, the conduction electrons donated by intercalated hydrogen atoms effectively remove carriers from the hole conduction band that is responsible for superconductivity, resulting in a deterioration of superconductivity. Clearly, the successful realization of carrier doping through hydrogen intercalation requires materials with favorable electronic and structural characteristics. This technique has previously been shown to stabilize the metallic phase in single crystal VO_2 nanobeams at room temperature, in which case the hydrogenation procedure is reversible [7], which could prove technologically useful if it also holds for TMDs.

8.2 Methods

Single crystals of $1T$-$TiSe_2$ were grown by Justin Chen under the supervision of Prof. Emilia Morosan, using iodine vapor transport in a sealed quartz tube. The resulting crystals, reddish brown in color and with typical lateral dimensions of a few mm, were mechanically exfoliated into thin layers using the scotch tape method and deposited onto an oxidized silicon wafer. Metal contacts were defined by e-beam lithography, e-beam evaporation of 5 nm Ti and 50 nm Au or Pd, and liftoff. Sample thicknesses were determined by atomic force microscopy (AFM). Very thin crystals (less than about 10 nm thick) were found not to be air-stable, exhibiting noticeable color changes over time, presumably due to oxidation.

The metal contacts also serve as catalysts, allowing for hydrogenation by the spillover method (wherein H_2 is catalytically split into atomic hydrogen by the metal, and can then intercalate into the $TiSe_2$ lattice) [219, 7]. In addition to relying on the metal contacts, one sample was also coated with a very thin (0.5 nm average thickness), discontinuous layer of Pd (nano)particles by e-beam evaporation, in an attempt to increase the surface area of $TiSe_2$ in contact with the metal catalyst without shorting all the contacts together. The doping protocol consisted of annealing the sample in an environment of flowing forming gas (20% hydrogen in nitrogen) at ambient pressure and constant temperature in a quartz tube furnace, for a specified amount of time (conditions varied for each instance of doping; details are recorded below). Qualitatively, Pd was found to be more efficient than Au as a catalyst in this spillover process, as inferred from the relative change of transport properties after similar hydrogenation procedures (comparison between one sample with Au contacts and one with Pd contacts).

8.3 Results

Transport measurements were performed in a Quantum Design PPMS. Temperature-dependent resistivity data were collected by a four-probe, low-frequency lock-in method, and the resistivity data for a $\sim$ 27 nm thick sample with Pd contacts are shown in Fig. 8.2. A remarkable evolution of the CDW peak is observed with increasing hydrogenation. The four hydrogenation steps were carried out sequentially as follows (with transport measurements performed between steps): (1) 22 hours at T = 150 °C; (2) 50 hours at T = 150 °C; (3) 74 hours at T = 150 °C after e-beam deposition of 0.5 nm Pd to increase the surface area of the Pd catalyst material in contact with $TiSe_2$; (4) 95 hours at T = 175 °C (with Pd particles still in place). Note that moderate annealing temperatures are chosen to avoid loss of Se. After the fourth hydrogen treatment and subsequent resistivity vs. temperature measurement, one of the Pd contacts failed due to peeling off (likely due to expansion of Pd under hydrogen exposure; see Fig.

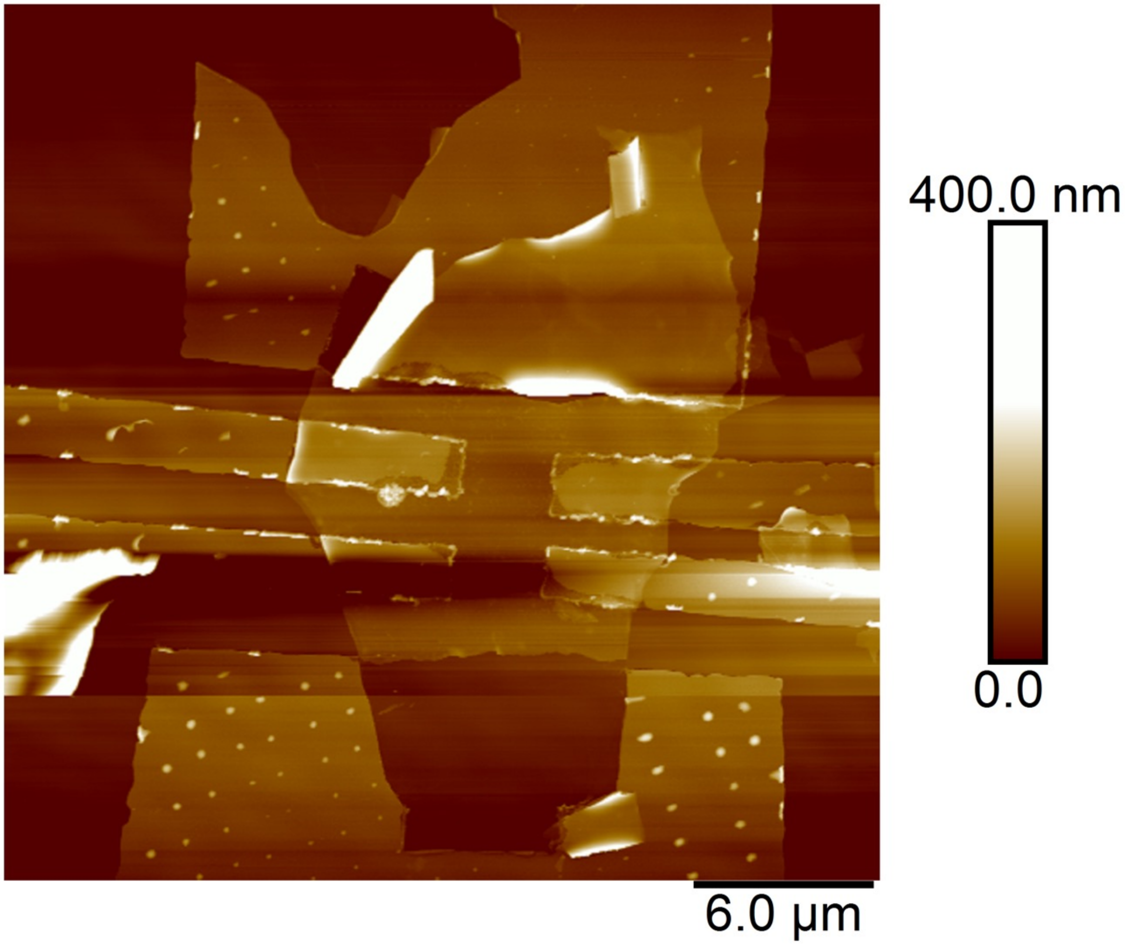

Figure 8.1: **AFM image of Pd-contacted $TiSe_2$ flake (t ≈ 27 nm) after several hydrogenation cycles.** The Pd contacts peeled off more with each successive hydrogenation step, until the device was no longer measurable.

8.1), and so no further measurements were possible.

The temperature dependent resistivity curve $\rho(T)$ measured before hydrogenation (the uppermost curve of Fig. 8.2) is consistent with bulk measurements, showing a clear CDW peak near T = 156 K, with negative slope at higher temperatures, and positive slope below the CDW peak down to low temperatures. After each of four successive hydrogenation steps, the CDW peak was gradually suppressed, until it was no longer visible except as a slight “knee” in the resistivity curve. Concurrently, the slope of $\rho(T)$ becomes positive above the CDW peak with increasing hydrogenation, and the resistivity magnitude is systematically reduced throughout the measured temperature range of 4.2 – 300 K. This is similar to what was observed in Cu_xTiSe_2 [216] at low Cu concentrations. Here, although the low-temperature resistivity is significantly reduced after hydrogenation, superconductivity is not observed down to the lowest measurement temperature, $T = 4.2$ K. Extending the measurement temperature range lower would be desirable.

Measurement of the Hall resistivity at various temperatures above and below the CDW transition after each hydrogenation step provides a way to monitor changes in carrier density with increasing hydrogen concentration. After three hydrogenation cycles, the carrier density n, calculated from the slope of the Hall resistivity data, increased by more than one order of magnitude in the temperature range 5 – 180 K. The negative slope of the Hall resistivity indicates that the majority carriers are electron-like, both in the pristine sample and all throughout the several steps of hydrogenation. Fig. 8.3(a) shows the Hall resistivity data with increasing hydrogenation at T = 5, 25, 125, and 180 K, and Fig. 8.3(b) shows the calculated carrier density as a function of temperature and hydrogenation.

We note that magnetoresistance (MR) measurements were attempted in both the pristine and hydrogenated states, but essentially no MR signal could be observed above the background noise level.

8.4 Discussion and conclusions

The presented data seem to indicate that hydrogen doping of $TiSe_2$ through the catalytic spillover process is possible, and can cause significant alterations of the material's electronic properties. These include an essentially complete suppression of the CDW state, signaled by the disappearance of the resistivity peak, along with an inferred increase in n-type carrier density of more than one order of magnitude. No checks have been done yet to verify that hydrogen really does become incorporated

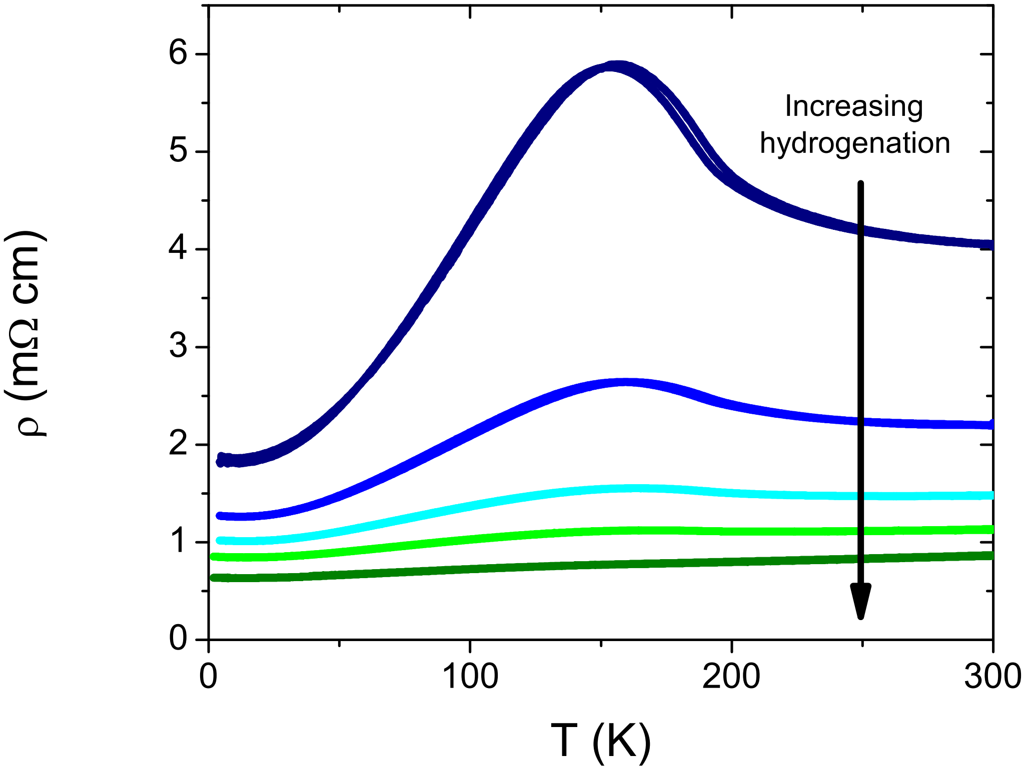

Figure 8.2: **Temperature-dependent resistivity of $TiSe_2$ after several hydrogenation cycles.** The uppermost (dark blue) curve was measured before hydrogenation and shows a clear CDW peak near $T = 156$ K. Increasing hydrogenation systematically lowers the resistance throughout the temperature range 4.2 – 300 K, progressively suppressing the CDW peak until only a "knee," rather than a peak, remains in the lowermost curve. The high-temperature slope of resistivity also changes sign, indicating that hydrogenation results in metallic conduction at room temperature.

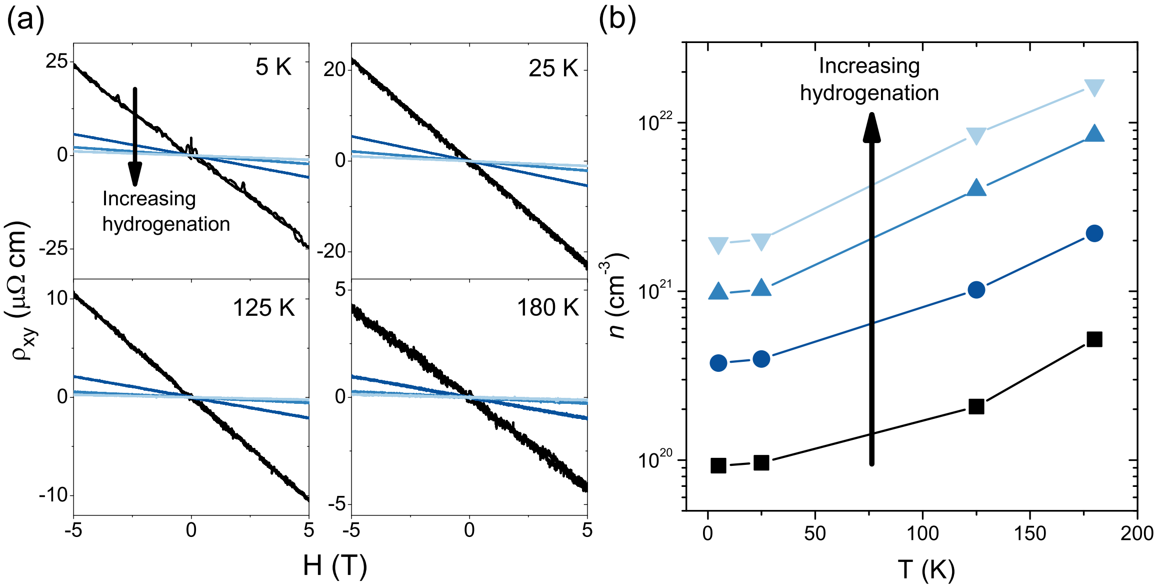

Figure 8.3: **Hall measurements and carrier density** a) Hall resistivity as a function of magnetic field at selected temperatures. The black curve (largest absolute slope) in each panel was measured prior to hydrogenation. Data collected after three subsequent hydrogenation steps show progressively lower slope, consistent with increasing n-type carrier density. b) Carrier density (extracted from Hall data) as a function of temperature, showing an increase of more than one order of magnitude with increasing hydrogenation, throughout the temperature range 5 – 180 K.

into the crystal, so we can only conjecture that this is true based on the transport evidence. As we have learned in the case of VO_2, direct measurement of hydrogen concentration in such small samples is extremely challenging, though perhaps the hydrogen concentration in $TiSe_2$ could be estimated through computational techniques.

Regrettably, a preliminary control experiment consisting of annealing the pristine sample in Ar gas (rather than forming gas) was not performed before hydrogenation of the Pd-contacted sample. Annealing in inert gas could be imagined to improve contact resistance or drive off surface impurities, resulting in a measured improvement of conductivity and apparent increase in carrier density without any modification of the material itself (just the contact properties). Such a control experiment was performed for the Au-contacted sample, using the same temperature and duration conditions as were later repeated for hydrogenation, without any obvious effect. We note that the resistivity properties of the pristine Pd-contacted sample (before doping) show the expected curve shape and CDW peak that are well-characterized for $TiSe_2$, so we believe the contacts were indeed initially of good quality. Furthermore, the carrier density measured using the pristine sample was already of the approximate expected magnitude, and after the several steps of hydrogen annealing, the carrier density appears to increase by over an order of magnitude, inconsistent with the idea of a simple contact improvement.

Additional experiments are in order to complete this work. Specifically, the measurements should be repeated on more samples to verify reproducible results with Pd contacts. Measurements down to lower temperatures, precluded here by a period of sub-optimal PPMS functionality, should also be made. Another procedure worth trying would be treatment of $TiSe_2$ with atomic hydrogen generated from a hot filament, as discussed in Chapter 3. Since Pd swells dimensionally upon hydrogen uptake, and the catalytic performance of the contacts should not play a role in atomic hydrogenation, Au contacts would likely be a more robust choice in that situation. One might conjecture that the most favorable direction for hydrogen intercalation would be from the edges (with hydrogen atoms eventually residing between the Van der Waals bonded layers), so maximizing the exposed perimeter would be preferred for quickest hydrogenation, *e.g.*, by choosing long narrow exfoliated flakes if possible. Finally, hydrogenation of other TMD materials could be attempted as well. Some preliminary attempts were made with $\mathrm{MoS_2}$ but without any noticeable effect (beyond improvement of contacts during the moderate temperature annealing, with essentially the same result obtained in control experiments using Ar or forming gas annealing environments), though the measurements were not rigorous enough to rule out the possibility entirely. It is worth noting that bulk single crystals of $\mathrm{TiSe_2}$ (and many other TMD materials) are now commercially available for purchase, leaving many options open if the desired materials are not available from synthesis groups at Rice or other collaborators.

Chapter 9

Appendix B: Useful Vendor Information

This Appendix contains a list of useful lab equipment vendors we have purchased from in the past, and commentary about what they sell. Many common items not covered on this list are available at Rice's Chemistry Stockroom. The following is intended to be a useful starting point for sourcing lab supplies, and is not an endorsement of any vendor or product.

9.1 Local Houston-Area Vendors

Home Depot, Lowes: general tools and hardware supplies

Houston Center Valve and Fitting: Swagelok fittings, specialty tubing

American Vacuum Technology: Vacuum pump repair with pickup and delivery. http://www.americanvacuum.biz

Allied Electronics

Mouser Electronics: Huge selection. They're in the Dallas area, but order before 6pm and choose UPS ground for effective 1-day shipping.

9.2 General Scientific Supply Vendors

ThermoFisher

VWR

Sigma Aldrich: general chemicals

9.3 Microscopy supplies

Ted Pella: moderately priced good tweezers; TEM grids

SPI: moderately priced good tweezers, SEM gold standards, silver paint

Electron Microscopy Sciences: Carbon tape, SEM stubs (sold in Chem Stockroom)

NanoAndMore: moderately priced AFM tips

9.4 Lab tools

Erem: expensive tweezers and fine coaxial cable stripper

Techni Tool: expensive tweezers and pliers

California Fine Wire: Au and copper wire

TEQCOM: nitrogen blower

9.5 Vacuum Supplies

Kurt Lesker: lots of vacuum parts ; excellent website

Ideal Vacuum: expensive but good; excellent website

Duniway: pumps and parts

AJVS: often cheaper if they have what you want

MDC: fittings and flanges; website difficult to navigate

Capitol Vacuum: cheaper pump rebuild kits

Edwards, Pfeiffer, Alcatel, Leybold, etc. vacuum pumps

Santovac 5: best diffusion pump fluid (polyphenyl ether)

MKS: mass-flow controllers, gauges

9.6 Hand and power tools, raw materials

McMaster-Carr: Carries one of everything

Grainger more expensive; several Houston locations as well as mail-order

Goodfellow metals: small quantities

9.7 Deposition materials

Kurt Lesker: quartz crystals for thickness monitor; reasonable prices on non-precious deposition materials

Materion: Formerly Cerac; best price on Au at this time

International Advanced Materials: Edwards-style 3cc crucible liners

Kamis

American Elements

ESPI

Alfa Aesar

9.8 Cryogenics

Quantum Design: PPMS, MPMS

Lakeshore Cryo: Probe station items (ours is Desert Cryo, which was bought by Lakeshore), temperature sensors and cryogenic accessories

Cryo Mech: helium recovery system

Cryo Fab: helium dewars

Cryo Industries: cryostats

Taylor Wharton: nitrogen dewars

Tempshield: blue cryogen-handling gloves

9.9 Lithography Supplies

FrontRange Photomask: fast turnaround, good photomasks, reasonable prices

Photo Etch Technologies: good shadowmasks, sometimes slow service

References

---

[1] E. Morosan, H. W. Zandbergen, L. Li, M. Lee, J. G. Checkelsky, M. Heinrich, T. Siegrist, N. P. Ong, and R. J. Cava, “Sharp switching of the magnetization in $Fe_{1/4}TaS_2$,” *Phys. Rev. B*, vol. 75, p. 104401, Mar 2007. [Online]. Available: http://link.aps.org/doi/10.1103/PhysRevB.75.104401 (document), 1.1, 5.1, 5.2, 5.3, 5.3, 5.3

[2] S. Sze and K. Ng, *Physics of Semiconductor Devices*, 3rd ed. John Wiley and Sons, 2007. (document), 1.2

[3] J. H. Park, J. M. Coy, T. S. Kasirga, C. Huang, Z. Fei, S. Hunter, and D. H. Cobden, “Measurement of a solid-state triple point at the metal-insulator transition in VO_2,” *Nature*, vol. 500, no. 7463, pp. 431–434, Aug. 2013. [Online]. Available: http://dx.doi.org/10.1038/nature12425 (document), 1.3

[4] C. Varma, “High-temperature superconductivity: Mind the pseudogap,” *Nature*, vol. 468, no. 7321, pp. 184–185, Nov. 2010. [Online]. Available: http://dx.doi.org/10.1038/468184a (document), 1.4

[5] *Physical Property Measurement System: Hardware Manual*, 6th ed., Quantum Design, San Diego, CA, 2008. (document), 2.2

[6] H.-T. Zhang, L. Zhang, D. Mukherjee, Y.-X. Zheng, R. C. Haislmaier, N. Alem, and R. Engel-Herbert, “Wafer-scale growth of VO_2 thin films using a combinatorial approach,” *Nature Communications*, vol. 6, p. 8475, Oct. 2015. [Online]. Available: http://dx.doi.org/10.1038/ncomms9475 (document), 3.1

[7] J. Wei, H. Ji, W. Guo, A. H. Nevidomskyy, and D. Natelson, “Hydrogen stabilization of metallic vanadium dioxide in single-crystal nanobeams,” *Nat Nano*, vol. 7, no. 6, pp. 357–362, Jun. 2012. [Online]. Available: http://dx.doi.org/10.1038/nnano.2012.70 (document), 3, 3.2, 3.1, 3.2, 3.2, 8.1, 8.2

[8] W. J. Hardy, H. Ji, H. Paik, D. Schlom, and D. Natelson, "Mesoscopic quantum effects in a bad metal, hydrogen-doped vanadium dioxide," *Submitted, J. Phys.: Cond. Matter*, 2017. (document), 3, 3.3, 3.4, 3.5, 3.6, 3.7, 3.8, 3.9

[9] N. Nakagawa, H. Y. Hwang, and D. A. Muller, "Why some interfaces cannot be sharp," *Nat. Mater.*, vol. 5, no. 3, pp. 204–209, Mar. 2006. [Online]. Available: http://dx.doi.org/10.1038/nmat1569 (document), 4.1

[10] H. Y. Hwang, Y. Iwasa, M. Kawasaki, B. Keimer, N. Nagaosa, and Y. Tokura, "Emergent phenomena at oxide interfaces," *Nature Materials*, vol. 11, no. 2, pp. 103–113, Feb. 2012. [Online]. Available: http://dx.doi.org/10.1038/nmat3223 (document), 4.1, 4.2

[11] C. A. Jackson, J. Y. Zhang, C. R. Freeze, and S. Stemmer, "Quantum critical behaviour in confined $SrTiO_3$ quantum wells embedded in antiferromagnetic $SmTiO_3$," *Nat Commun*, vol. 5, Jul. 2014. [Online]. Available: http://dx.doi.org/10.1038/ncomms5258 (document), 4.1, 4.3, 4.2, 4.4

[12] W. J. Hardy, B. Isaac, P. B. Marshall, E. Mikheev, P. Zhou, S. Stemmer, and D. Natelson, "Potential fluctuations at low temperatures in mesoscopic-scale $SmTiO_3/SrTiO_3/SmTiO_3$ quantum well structures," *ACS Nano*, Mar. 2016. [Online]. Available: http://dx.doi.org/10.1021/acsnano.6b08427 (document), 4, 4.5, 4.6, 4.7, 4.8, 4.9, 4.10, 4.11, 4.12, 4.13, 4.14, 4.15, 4.16, 4.17, 4.18

[13] T. A. Cain, E. Mikheev, C. A. Jackson, and S. Stemmer, "Dichotomy of the transport coefficients of correlated electron liquids in $SrTiO_3$," *arXiv:1609.04149 [cond-mat.str-el]*, Sep. 2016. [Online]. Available: https://arxiv.org/abs/1609.04149 (document), 4.6, 4.4, 4.4

[14] W. J. Hardy, C.-W. Chen, A. Marcinkova, H. Ji, J. Sinova, D. Natelson, and E. Morosan, "Very large magnetoresistance in $Fe_{0.28}TaS_2$ single crystals," *Phys. Rev. B*, vol. 91, no. 5, p. 054426, Feb. 2015. [Online]. Available: http://link.aps.org/doi/10.1103/PhysRevB.91.054426 (document), 5, 5.1, 5.2, 5.3, 5.4, 5.5, 5.6, 5.7, 5.8

[15] W. J. Hardy, J. Yuan, H. Guo, P. Zhou, J. Lou, and D. Natelson, "Thickness-dependent and magnetic-field-driven suppression of antiferromagnetic order in thin V_5S_8 single crystals," *ACS Nano*, vol. 10, no. 6, pp. 5941–5946, Jun. 2016. [Online]. Available: http://dx.doi.org/10.1021/acsnano.6b01269 (document), 6, 6.1, 6.2, 6.4, 6.5, 6.6, 6.8, 6.9, 6.10, 6.11, 6.12

[16] M. Nakanishi, K. Yoshimura, K. Kosuge, T. Goto, T. Fujii, and J. Takada, "Anomalous field-induced magnetic transitions in V_5X_8 (X=S, Se)," *Journal of Magnetism and Magnetic Materials*, vol. 221, no. 3, pp. 301–306, 2000. [Online]. Available: http://www.sciencedirect.com/science/article/pii/S0304885300005096 (document), 6.1, 6.3, 6.3

[17] J. Stöhr, "Magnetic dichroism specgroscopy and microscopy." [Online]. Available: https://www-ssrl.slac.stanford.edu/stohr/xmcd.htm (document), 6.7

[18] T. Ebihara, N. Harrison, M. Jaime, S. Uji, and J. C. Lashley, "Emergent fluctuation hot spots on the fermi surface of $CeIn_3$ in strong magnetic fields," *Phys. Rev. Lett.*, vol. 93, no. 24, p. 246401, Dec. 2004. [Online]. Available: http://link.aps.org/doi/10.1103/PhysRevLett.93.246401 (document), 6.3, 6.12

[19] T. Ebihara, A. V. Silhanek, M. Jaime, and N. Harrison, "Suppression of antiferromagnetic ordering by magnetic field in $Ce_{0.6}La_{0.4}In_3$," *Journal of Physics: Conference Series*, vol. 592, no. 1, p. 012079, 2015. [Online]. Available: http://stacks.iop.org/1742-6596/592/i=1/a=012079 (document), 6.3, 6.12

[20] P. W. Anderson, "More is different," *Science*, vol. 177, no. 4047, p. 393, Aug. 1972. [Online]. Available: http://science.sciencemag.org/content/177/4047/393.abstract 1

[21] R. B. Laughlin, *A Different Universe: Reinventing Physics from the Bottom Down.* Basic Books, 2006. [Online]. Available: https://books.google.com/books?id=I5kbyB-yfB4C 1

[22] O. Gunnarsson, M. Calandra, and J. E. Han, "Colloquium : Saturation of electrical resistivity," *Rev. Mod. Phys.*, vol. 75, pp. 1085—1099, 2003. [Online]. Available: http://link.aps.org/doi/10.1103/RevModPhys.75.1085 1.1.1, 3.1

[23] N. E. Hussey, K. Takenaka, and H. Takagi, "Universality of the Mott-Ioffe-Regel limit in metals," *Philosophical Magazine*, vol. 84, no. 27, pp. 2847–2864, 2004. [Online]. Available: http://dx.doi.org/10.1080/14786430410001716944 1.1.1, 3.1

[24] A. D. Kent and D. C. Worledge, "A new spin on magnetic memories," *Nat Nano*, vol. 10, no. 3, pp. 187–191, Mar. 2015. [Online]. Available: http://dx.doi.org/10.1038/nnano.2015.24 1.1.2

[25] N. W. Ashcroft and N. D. Mermin, *Solid State Physics.* Belmont, CA: Brooks/Cole, 1976. 1.2

[26] N. F. Mott, "The basis of the electron theory of metals, with special reference to the transition metals," *Proceedings of the Physical Society. Section A*, vol. 62, no. 7, p. 416, 1949. 1.2

[27] A. P. Ramirez, "Colossal magnetoresistance," *Journal of Physics: Condensed Matter*, vol. 9, no. 39, p. 8171, 1997. [Online]. Available: http://stacks.iop.org/0953-8984/9/i=39/a=005 1.2

[28] F. J. Morin, "Oxides which show a metal-to-insulator transition at the Néel temperature," *Phys. Rev. Lett.*, vol. 3, no. 1, pp. 34–36, Jul. 1959. [Online]. Available: http://link.aps.org/doi/10.1103/PhysRevLett.3.34 1.2

[29] N. F. Mott, "Metal-insulator transition," *Rev. Mod. Phys.*, vol. 40, no. 4, pp. 677–683, Oct. 1968. [Online]. Available: http://link.aps.org/doi/10.1103/RevModPhys.40.677 1.2

[30] A. Zylbersztejn and N. F. Mott, "Metal-insulator transition in vanadium dioxide," *Phys. Rev. B*, vol. 11, no. 11, pp. 4383–4395, Jun. 1975. [Online]. Available: http://link.aps.org/doi/10.1103/PhysRevB.11.4383 1.2

[31] E. J. W. Verwey, "Electronic conduction of magnetite (Fe_3O_4) and its transition point at low temperatures," *Nature*, vol. 144, no. 3642, pp. 327–328, 1939. 1.2

[32] F. Walz, "The Verwey transition-a topical review," *Journal of Physics: Condensed Matter*, vol. 14, no. 12, p. R285, 2002. 1.2

[33] M. L. Medarde, "Structural, magnetic and electronic properties of $RNiO_3$ perovskites (R = rare earth)," *Journal of Physics: Condensed Matter*, vol. 9, no. 8, p. 1679, 1997. [Online]. Available: http://stacks.iop.org/0953-8984/9/i=8/a=003 1.2

[34] J. Hubbard, "Electron correlations in narrow energy bands," vol. 276, no. 1365. The Royal Society, 1963, pp. 238–257. 1.2

[35] J. Bardeen, L. N. Cooper, and J. R. Schrieffer, "Microscopic theory of superconductivity," *Phys. Rev.*, vol. 106, no. 1, pp. 162–164, Apr. 1957. [Online]. Available: https://link.aps.org/doi/10.1103/PhysRev.106.162 1.3

[36] B. Keimer, S. A. Kivelson, M. R. Norman, S. Uchida, and J. Zaanen, "From quantum matter to high-temperature superconductivity in copper oxides," *Nature*, vol. 518, no. 7538, pp. 179–186, Feb. 2015. [Online]. Available: http://dx.doi.org/10.1038/nature14165 1.3, 4.1

[37] J. G. Bednorz and K. A. Müller, "Possible high T_C superconductivity in the BaLaCuO system," *Zeitschrift für Physik B Condensed Matter*, vol. 64, no. 2, pp. 189–193, 1986. [Online]. Available: http://dx.doi.org/10.1007/BF01303701 1.3

[38] L. H. Thomas, "The calculation of atomic fields," vol. 23, no. 05. Cambridge Univ Press, 1927, pp. 542–548. 1.3

[39] E. Fermi, "Eine statistische methode zur bestimmung einiger eigenschaften des atoms und ihre anwendung auf die theorie des periodischen systems der elemente," *Zeitschrift fur Physik*, vol. 48, no. 1, pp. 73–79, 1928. [Online]. Available: http://dx.doi.org/10.1007/BF01351576 1.3

[40] W. Kohn, "Nobel lecture: Electronic structure of matter − wave functions and density functionals," *Nobel Media AB 2014*. [Online]. Available: http://www.nobelprize.org/nobel_prizes/chemistry/laureates/1998/kohn-lecture.html 1.3

[41] W. Kohn and L. J. Sham, "Self-consistent equations including exchange and correlation effects," *Phys. Rev.*, vol. 140, no. 4A, pp. A1133–A1138, Nov. 1965. [Online]. Available: http://link.aps.org/doi/10.1103/PhysRev.140.A1133 1.3

[42] V. Loganathan, Private communication, 2017. 1.3

[43] A. Georges, G. Kotliar, W. Krauth, and M. J. Rozenberg, "Dynamical mean-field theory of strongly correlated fermion systems and the limit of infinite dimensions," *Rev. Mod. Phys.*, vol. 68, no. 1, pp. 13–125, Jan. 1996. [Online]. Available: http://link.aps.org/doi/10.1103/RevModPhys.68.13 1.3

[44] G. Kotliar and D. Vollhardt, "Strongly correlated materials: Insights from dynamical mean-field theory," *Physics Today*, vol. 57, no. 3, 2004. [Online]. Available: http://physicstoday.scitation.org/doi/full/10.1063/1.1712502 1.3

[45] C. Weber, D. D. O'Regan, N. D. M. Hine, M. C. Payne, G. Kotliar, and P. B. Littlewood, "Vanadium dioxide: A Peierls-Mott insulator stable against disorder," *Phys. Rev. Lett.*, vol. 108, no. 25, p. 256402, Jun. 2012. [Online]. Available: http://link.aps.org/doi/10.1103/PhysRevLett.108.256402 1.3, 3

[46] R. P. Feynman, "There's plenty of room at the bottom," APS Meeting Lecture, December 1959. [Online]. Available: http://www.its.caltech.edu/~feynman/plenty.html 2

[47] B. Radisavljevic, A. Radenovic, J. Brivio, V. Giacometti, and A. Kis, "Single-layer mos2 transistors," *Nat. Nano*, vol. 6, no. 3, pp. 147–150, Mar. 2011. [Online]. Available: http://dx.doi.org/10.1038/nnano.2010.279 2

[48] S. Frank, P. Poncharal, Z. L. Wang, and W. A. d. Heer, "Carbon nanotube quantum resistors," *Science*, vol. 280, no. 5370, p. 1744, Jun. 1998. [Online]. Available: http://science.sciencemag.org/content/280/5370/1744.abstract 2

[49] A. Yacoby, H. L. Stormer, N. S. Wingreen, L. N. Pfeiffer, K. W. Baldwin, and K. W. West, "Nonuniversal conductance quantization in quantum wires," *Phys. Rev. Lett.*, vol. 77, no. 22, pp. 4612–4615, Nov. 1996. [Online]. Available: https://link.aps.org/doi/10.1103/PhysRevLett.77.4612 2

[50] A. P. Alivisatos, "Semiconductor clusters, nanocrystals, and quantum dots," *Science*, vol. 271, no. 5251, p. 933, 1996. 2

[51] R. A. Webb, S. Washburn, C. P. Umbach, and R. B. Laibowitz, "Observation of $\frac{h}{e}$ Aharonov-Bohm oscillations in normal-metal rings," *Phys. Rev. Lett.*, vol. 54, no. 25, pp. 2696–2699, Jun. 1985. [Online]. Available: http://link.aps.org/doi/10.1103/PhysRevLett.54.2696 2

[52] B. S. Guiton, Q. Gu, A. L. Prieto, M. S. Gudiksen, and H. Park, "Single-crystalline vanadium dioxide nanowires with rectangular cross sections," *Journal of the American Chemical Society*, vol. 127, no. 2, pp. 498–499, 2005, pMID: 15643854. [Online]. Available: http://dx.doi.org/10.1021/ja045976g 2.1

[53] T. S. Kasirga, D. Sun, J. H. Park, J. M. Coy, Z. Fei, X. Xu, and D. H. Cobden, "Photoresponse of a strongly correlated material determined by scanning photocurrent microscopy," *Nat Nano*, vol. 7, no. 11, pp. 723–727, Nov. 2012. [Online]. Available: http://dx.doi.org/10.1038/nnano.2012.176 2.1

[54] H. Ji, "Hydrogen doping and the metal-insulator phase transition in vanadium dioxide," Ph.D. dissertation, Rice University, 2015. 2.1, 3

[55] K. S. Novoselov, A. K. Geim, S. V. Morozov, D. Jiang, Y. Zhang, S. V. Dubonos, I. V. Grigorieva, and A. A. Firsov, "Electric field effect in atomically thin carbon films," *Science*, vol. 306, no. 5696, pp. 666–669, 2004. [Online]. Available: http://www.sciencemag.org/content/306/5696/666.abstract 2.1, 5.2

[56] D. Natelson, *Fabrication of metal nanowires (invited book chapter in Recent Research Developments in Vacuum Science and Technology 4, ed. J. Dabrowski)*. Kerala, India: Research Signpost, 2003. [Online]. Available: http://xxx.lanl.gov/abs/cond-mat/0307600 2.1.1

[57] ——, *Nanostructures and Nanotechnology.* Cambridge UP, 2015. 2.1.1

[58] "Material deposition chart," Kurt J. Lesker Company, Tech. Rep., 2017. [Online]. Available: https://www.lesker.com/newweb/deposition_materials/materialdepositionchart.cfm?pgid=0 2.1.2

[59] T. L. Cocker, L. V. Titova, S. Fourmaux, G. Holloway, H.-C. Bandulet, D. Brassard, J.-C. Kieffer, M. A. El Khakani, and F. A. Hegmann, "Phase diagram of the ultrafast photoinduced insulator-metal transition in vanadium dioxide," *Phys. Rev. B*, vol. 85, p. 155120, Apr 2012. [Online]. Available: http://link.aps.org/doi/10.1103/PhysRevB.85.155120 3

[60] A. X. Gray, J. Jeong, N. P. Aetukuri, P. Granitzka, Z. Chen, R. Kukreja, D. Higley, T. Chase, A. H. Reid, H. Ohldag, M. A. Marcus, A. Scholl, A. T. Young, A. Doran, C. A. Jenkins, P. Shafer, E. Arenholz, M. G. Samant, S. S. P. Parkin, and H. A. Dürr, "Correlation-driven insulator-metal transition in near-ideal vanadium dioxide films," *Phys. Rev. Lett.*, vol. 116, p. 116403, Mar 2016. [Online]. Available: http://link.aps.org/doi/10.1103/PhysRevLett.116.116403 3

[61] J. Wei and D. Natelson, "Nanostructure studies of strongly correlated materials," *Nanoscale*, vol. 3, no. 9, pp. 3509–3521, 2011. [Online]. Available: http://dx.doi.org/10.1039/C1NR10457H 3

[62] E. Morosan, D. Natelson, A. H. Nevidomskyy, and Q. Si, "Strongly correlated materials," *Adv. Mater.*, vol. 24, no. 36, pp. 4896–4923, Sep. 2012. [Online]. Available: http://dx.doi.org/10.1002/adma.201202018 3

[63] H. Ji, J. Wei, and D. Natelson, "Modulation of the electrical properties of VO_2 nanobeams using an ionic liquid as a gating medium," *Nano Lett.*, vol. 12, no. 6, pp. 2988–2992, Jun. 2012. [Online]. Available: http://dx.doi.org/10.1021/nl300741h 3

[64] Y. Filinchuk, N. A. Tumanov, V. Ban, H. Ji, J. Wei, M. W. Swift, A. H. Nevidomskyy, and D. Natelson, "In situ diffraction study of catalytic hydrogenation of VO_2: Stable phases and origins of metallicity," *Journal of the American Chemical Society*, vol. 136, no. 22, pp. 8100–8109, 2014, pMID: 24825186. [Online]. Available: http://dx.doi.org/10.1021/ja503360y 3, 3.1, 3.2, 3.3.1

[65] J. Lin, H. Ji, M. W. Swift, W. J. Hardy, Z. Peng, X. Fan, A. H. Nevidomskyy, J. M. Tour, and D. Natelson, "Hydrogen diffusion and stabilization in single-crystal VO_2 micro/nanobeams by direct atomic hydrogenation," *Nano Letters*, vol. 14, no. 9, pp. 5445–5451, 2014, pMID: 25148601. [Online]. Available: http://dx.doi.org/10.1021/nl5030694 3, 3.1, 3.2

[66] Y. Imry, *Introduction to Mesoscopic Physics*. OUP Oxford, 2008. [Online]. Available: https://books.google.com/books?id=i7yaPwAACAAJ 3.1

[67] G. Bergmann, "Weak localization in thin films: a time-of-flight experiment with conduction electrons," *Physics Reports*, vol. 107, no. 1, pp. 1–58, 1984. [Online]. Available: http://www.sciencedirect.com/science/article/pii/0370157384901030 3.1, 3.3.1, 3.3.2

[68] P. A. Lee and A. D. Stone, "Universal conductance fluctuations in metals," *Physical Review Letters*, vol. 55, no. 15, pp. 1622–1625, Oct. 1985. [Online]. Available: http://link.aps.org/doi/10.1103/PhysRevLett.55.1622 3.1, 3.3.4, 4.3, 4.4

[69] Y. B. Khavin, M. E. Gershenson, and A. L. Bogdanov, "Decoherence and the Thouless crossover in one-dimensional conductors," *Phys. Rev. Lett.*, vol. 81, pp. 1066—1069, 1998. [Online]. Available: http://link.aps.org/doi/10.1103/PhysRevLett.81.1066 3.1

[70] L. A. Ladd and W. Paul, "Optical and transport properties of high quality crystals of V_2O_4 near the metallic transition temperature," *Solid State Communications*, vol. 7, no. 4, pp. 425–428, 1969. [Online]. Available: http://www.sciencedirect.com/science/article/pii/0038109869908886 3.1

[71] M. M. Qazilbash, K. S. Burch, D. Whisler, D. Shrekenhamer, B. G. Chae, H. T. Kim, and D. N. Basov, "Correlated metallic state of vanadium

dioxide," *Phys. Rev. B*, vol. 74, p. 205118, 2006. [Online]. Available: http://link.aps.org/doi/10.1103/PhysRevB.74.205118 3.1, 3.3.1, 3.3.1

[72] H. Yoon, M. Choi, T.-W. Lim, H. Kwon, K. Ihm, J. K. Kim, S.-Y. Choi, and J. Son, "Reversible phase modulation and hydrogen storage in multivalent VO_2 epitaxial thin films," *Nat Mater*, vol. 15, no. 10, pp. 1113–1119, Oct. 2016. [Online]. Available: http://dx.doi.org/10.1038/nmat4692 3.1, 3.2

[73] W. H. Rosevear and W. Paul, "Hall effect in VO_2 near the semiconductor-to-metal transition," *Phys. Rev. B*, vol. 7, pp. 2109—2111, 1973. [Online]. Available: http://link.aps.org/doi/10.1103/PhysRevB.7.2109 3.1, 3.3.1

[74] D. Ruzmetov, D. Heiman, B. B. Claflin, V. Narayanamurti, and S. Ramanathan, "Hall carrier density and magnetoresistance measurements in thin-film vanadium dioxide across the metal-insulator transition," *Phys. Rev. B*, vol. 79, p. 153107, 2009. [Online]. Available: http://link.aps.org/doi/10.1103/PhysRevB.79.153107 3.1, 3.3.1

[75] H. Paik, J. A. Moyer, T. Spila, J. W. Tashman, J. A. Mundy, E. Freeman, N. Shukla, J. M. Lapano, R. Engel-Herbert, W. Zander, J. Schubert, D. A. Muller, S. Datta, P. Schiffer, and D. G. Schlom, "Transport properties of ultra-thin VO_2 films on (001) TiO_2 grown by reactive molecular-beam epitaxy," *Appl. Phys. Lett.*, vol. 107, no. 16, p. 163101, Oct. 2015. [Online]. Available: http://dx.doi.org/10.1063/1.4932123 3.2

[76] J. Wei, Z. Wang, W. Chen, and D. H. Cobden, "New aspects of the metal–insulator transition in single-domain vanadium dioxide nanobeams," *Nature Nano.*, vol. 4, no. 7, pp. 420—424, 2009. [Online]. Available: http://dx.doi.org/10.1038/nnano.2009.141 3.2

[77] An example of a commercial instrument designed for hydrogen analysis in inorganic solids is the Horiba EMGA-921. [Online]. Available: http://www.horiba.com/scientific/products/elemental-analyzers/oxygennitrogenhydrogen/details/emga-921-9403/ 3.2

[78] Y. Muraoka and Z. Hiroi, "Metal-insulator transition of VO_2 thin films grown on TiO_2 (001) and (110) substrates," *Applied Physics Letters*, vol. 80, no. 4, pp. 583—585, 2002. [Online]. Available: http://scitation.aip.org/content/aip/journal/apl/80/4/10.1063/1.1446215 3.3.1, 3.3.2

[79] A. W. Tyler, A. P. Mackenzie, S. Nishizaki, and Y. Maeno, "High-temperature resistivity of Sr_2RuO_4: Bad metallic transport in a good metal," *Phys. Rev. B*, vol. 58, pp. R10 107—R10 110, 1998. [Online]. Available: http://link.aps.org/doi/10.1103/PhysRevB.58.R10107 3.3.1

[80] M. Gurvitch and A. T. Fiory, "Resistivity of $La_{1.825}Sr_{0.175}CuO_4$ and $YBa_2Cu_3O_7$ to 1100 K: Absence of saturation and its implications,"

Phys. Rev. Lett., vol. 59, pp. 1337—1340, 1987. [Online]. Available: http://link.aps.org/doi/10.1103/PhysRevLett.59.1337 3.3.1

[81] T. Valla, P. D. Johnson, Z. Yusof, B. Wells, Q. Li, S. M. Loureiro, R. J. Cava, M. Mikami, Y. Mori, M. Yoshimura *et al.*, "Coherence-incoherence and dimensional crossover in layered strongly correlated metals," *Nature*, vol. 417, no. 6889, pp. 627—630, 2002. [Online]. Available: http://dx.doi.org/10.1038/nature00774 3.3.1

[82] J. Son, P. Moetakef, J. M. LeBeau, D. Ouellette, L. Balents, S. J. Allen, and S. Stemmer, "Low-dimensional Mott material: Transport in ultrathin epitaxial $LaNiO_3$ films," *Applied Physics Letters*, vol. 96, no. 6, p. 062114, 2010. [Online]. Available: http://scitation.aip.org/content/aip/journal/apl/96/6/10.1063/1.3309713 3.3.1

[83] R. Scherwitzl, S. Gariglio, M. Gabay, P. Zubko, M. Gibert, and J.-M. Triscone, "Metal-insulator transition in ultrathin $LaNiO_3$ films," *Phys. Rev. Lett.*, vol. 106, p. 246403, 2011. [Online]. Available: http://link.aps.org/doi/10.1103/PhysRevLett.106.246403 3.3.1, 3.3.1

[84] S. Hikami, A. I. Larkin, and Y. Nagaoka, "Spin-orbit interaction and magnetoresistance in the two dimensional random system," *Progress of Theoretical Physics*, vol. 63, no. 2, pp. 707—710, 1980. [Online]. Available: http://ptp.oxfordjournals.org/content/63/2/707.abstract 3.3.1

[85] D. V. Baxter, R. Richter, M. L. Trudeau, R. W. Cochrane, and J. O. Strom-Olsen, "Fitting to magnetoresistance under weak localization in three dimensions," *J. Phys. France*, vol. 50, no. 13, pp. 1673—1688, 1989. [Online]. Available: http://dx.doi.org/10.1051/jphys:0198900500130167300 3.3.1

[86] C. N. Berglund and H. J. Guggenheim, "Electronic properties of VO_2 near the semiconductor-metal transition," *Phys. Rev.*, vol. 185, pp. 1022—1033, 1969. [Online]. Available: http://link.aps.org/doi/10.1103/PhysRev.185.1022 3.3.1, 3.3.1

[87] K. Okazaki, S. Sugai, Y. Muraoka, and Z. Hiroi, "Role of electron-electron and electron-phonon interaction effects in the optical conductivity of VO_2," *Phys. Rev. B*, vol. 73, p. 165116, 2006. [Online]. Available: http://link.aps.org/doi/10.1103/PhysRevB.73.165116 3.3.1

[88] A. S. Belozerov, A. I. Poteryaev, and V. I. Anisimov, "Evidence for strong coulomb correlations in the metallic phase of vanadium dioxide," *JETP Letters*, vol. 93, no. 2, pp. 70–74, 2011. [Online]. Available: http://dx.doi.org/10.1134/S0021364011020056 3.3.1

[89] K. Saeki, T. Wakita, Y. Muraoka, M. Hirai, T. Yokoya, R. Eguchi, and S. Shin, "Band dispersion near the fermi level for VO_2 thin films grown

on TiO_2 (001) substrates," *Phys. Rev. B*, vol. 80, p. 125406, 2009. [Online]. Available: http://link.aps.org/doi/10.1103/PhysRevB.80.125406 3.3.1

[90] S. Maekawa and H. Fukuyama, "Magnetoresistance in two-dimensional disordered systems: Effects of Zeeman splitting and spin-orbit scattering," *Journal of the Physical Society of Japan*, vol. 50, no. 8, pp. 2516—2524, 1981. 3.3.1

[91] A. K. Nigam and A. K. Majumdar, "Magnetoresistance in canonical spin-glasses," *Phys. Rev. B*, vol. 27, pp. 495—511, 1983. [Online]. Available: http://link.aps.org/doi/10.1103/PhysRevB.27.495 3.3.1

[92] J. Jeong, N. Aetukuri, T. Graf, T. D. Schladt, M. G. Samant, and S. S. P. Parkin, "Suppression of metal-insulator transition in VO_2 by electric field-induced oxygen vacancy formation," *Science*, vol. 339, no. 6126, pp. 1402–1405, 2013. [Online]. Available: http://www.sciencemag.org/content/339/6126/1402.abstract 3.3.1

[93] L. Liu, "Effects of spin-orbit coupling in Si and Ge," *Phys. Rev.*, vol. 126, pp. 1317—1328, 1962. [Online]. Available: http://link.aps.org/doi/10.1103/PhysRev.126.1317 3.3.2

[94] B. Habib, J. Shabani, E. P. De Poortere, M. Shayegan, and R. Winkler, "Tuning of the spin-orbit interaction in two-dimensional GaAs holes *via* strain," *Phys. Rev. B*, vol. 75, p. 153304, 2007. [Online]. Available: http://link.aps.org/doi/10.1103/PhysRevB.75.153304 3.3.2

[95] A. Ohtomo and H. Y. Hwang, "A high-mobility electron gas at the $LaAlO_3/SrTiO_3$ heterointerface," *Nature*, vol. 427, no. 6973, pp. 423–426, Jan. 2004. [Online]. Available: http://dx.doi.org/10.1038/nature02308 4.1

[96] A. D. Caviglia, M. Gabay, S. Gariglio, N. Reyren, C. Cancellieri, and J.-M. Triscone, "Tunable rashba spin-orbit interaction at oxide interfaces," *Physical Review Letters*, vol. 104, no. 12, p. 126803, Mar. 2010. [Online]. Available: http://link.aps.org/doi/10.1103/PhysRevLett.104.126803 4.1

[97] J. A. Bert, B. Kalisky, C. Bell, M. Kim, Y. Hikita, H. Y. Hwang, and K. A. Moler, "Direct imaging of the coexistence of ferromagnetism and superconductivity at the $LaAlO_3/SrTiO_3$ interface," *Nat Phys*, vol. 7, no. 10, pp. 767–771, Oct. 2011. [Online]. Available: http://dx.doi.org/10.1038/nphys2079 4.1

[98] H. J. H. Ma, Z. Huang, W. M. L, A. Annadi, S. W. Zeng, L. M. Wong, S. J. Wang, T. Venkatesan, and Ariando, "Tunable bilayer two-dimensional electron gas in laalo3/srtio3 superlattices," *Applied Physics Letters*, vol. 105, no. 1, p. 011603, 2014. [Online]. Available: http://scitation.aip.org/content/aip/journal/apl/105/1/10.1063/1.4887235 4.1

[99] Y. Kim, R. M. Lutchyn, and C. Nayak, "Origin and transport signatures of spin-orbit interactions in one- and two-dimensional $SrTiO_3$-based heterostructures," *Physical Review B*, vol. 87, no. 24, p. 245121, Jun. 2013. [Online]. Available: http://link.aps.org/doi/10.1103/PhysRevB.87.245121 4.1

[100] X. Li, W. V. Liu, and L. Balents, "Spirals and skyrmions in two dimensional oxide heterostructures," *Physical Review Letters*, vol. 112, no. 6, p. 067202, Feb. 2014. [Online]. Available: http://link.aps.org/doi/10.1103/PhysRevLett.112.067202 4.1

[101] J. Y. Zhang, C. A. Jackson, R. Chen, S. Raghavan, P. Moetakef, L. Balents, and S. Stemmer, "Correlation between metal-insulator transitions and structural distortions in high-electron-density $SrTiO_3$ quantum wells," *Physical Review B*, vol. 89, no. 7, p. 075140, Feb. 2014. [Online]. Available: http://link.aps.org/doi/10.1103/PhysRevB.89.075140 4.1, 4.1, 4.2, 4.4

[102] S. Stemmer and A. J. Millis, "Quantum confinement in oxide quantum wells," *MRS Bulletin*, vol. 38, no. 12, pp. 1032–1039, 2013. 4.1

[103] J. Mannhart and D. G. Schlom, "Oxide interfaces–an opportunity for electronics," *Science*, vol. 327, no. 5973, pp. 1607–1611, Mar. 2010. [Online]. Available: http://science.sciencemag.org/content/327/5973/1607.abstract 4.1

[104] P. Zubko, S. Gariglio, M. Gabay, P. Ghosez, and J.-M. Triscone, "Interface physics in complex oxide heterostructures," *Annual Review of Condensed Matter Physics*, vol. 2, no. 1, pp. 141–165, Feb. 2011. [Online]. Available: http://dx.doi.org/10.1146/annurev-conmatphys-062910-140445 4.1

[105] J. Chakhalian, J. W. Freeland, A. J. Millis, C. Panagopoulos, and J. M. Rondinelli, "*Colloquium* : Emergent properties in plane view: Strong correlations at oxide interfaces," *Reviews of Modern Physics*, vol. 86, no. 4, pp. 1189–1202, Oct. 2014. [Online]. Available: http://link.aps.org/doi/10.1103/RevModPhys.86.1189 4.1

[106] G. Herranz, G. Singh, N. Bergeal, A. Jouan, J. Lesueur, J. Gázquez, M. Varela, M. Scigaj, N. Dix, F. Sánchez, and J. Fontcuberta, "Engineering two-dimensional superconductivity and Rashba spin-orbit coupling in $LaAlO_3/SrTiO_3$ quantum wells by selective orbital occupancy," *Nat Commun*, vol. 6, Jan. 2015. [Online]. Available: http://dx.doi.org/10.1038/ncomms7028 4.1

[107] S. Raghavan, J. Y. Zhang, and S. Stemmer, "Two-dimensional electron liquid at the (111) $SmTiO_3/SrTiO_3$ interface," *Applied Physics Letters*, vol. 106, no. 13, p. 132104, 2015. [Online]. Available: http://scitation.aip.org/content/aip/journal/apl/106/13/10.1063/1.4916963 4.1

[108] E. Mikheev, C. R. Freeze, B. J. Isaac, T. A. Cain, and S. Stemmer, "Separation of transport lifetimes in $SrTiO_3$-based two-dimensional electron liquids," *Physical Review B*, vol. 91, no. 16, p. 165125, Apr. 2015. [Online]. Available: http://link.aps.org/doi/10.1103/PhysRevB.91.165125 4.1, 4.2, 4.3

[109] P. B. Marshall, E. Mikheev, S. Raghavan, and S. Stemmer, "Pseudogaps and emergence of coherence in two-dimensional electron liquids in $SrTiO_3$," *Phys. Rev. Lett.*, vol. 117, no. 4, p. 046402, Jul. 2016. [Online]. Available: http://link.aps.org/doi/10.1103/PhysRevLett.117.046402 4.1, 4.4, 4.4

[110] P. Moetakef, T. A. Cain, D. G. Ouellette, J. Y. Zhang, D. O. Klenov, A. Janotti, C. G. Van de Walle, S. Rajan, S. J. Allen, and S. Stemmer, "Electrostatic carrier doping of $GdTiO_3/SrTiO_3$ interfaces," *Applied Physics Letters*, vol. 99, no. 23, 2011. [Online]. Available: http://scitation.aip.org/content/aip/journal/apl/99/23/10.1063/1.3669402 4.2

[111] P. A. Lee, A. D. Stone, and H. Fukuyama, "Universal conductance fluctuations in metals: Effects of finite temperature, interactions, and magnetic field," *Physical Review B*, vol. 35, no. 3, pp. 1039–1070, Jan. 1987. [Online]. Available: http://link.aps.org/doi/10.1103/PhysRevB.35.1039 4.3, 4.4

[112] S. Feng, A. J. Bray, P. A. Lee, and M. A. Moore, "Universal conductance fluctuations as a probe of chaotic behavior in mesoscopic metallic spin glasses," *Physical Review B*, vol. 36, no. 10, pp. 5624–5627, Oct. 1987. [Online]. Available: http://link.aps.org/doi/10.1103/PhysRevB.36.5624 4.3, 4.4

[113] S. Washburn and R. A. Webb, "Aharonov-bohm effect in normal metal quantum coherence and transport," *Advances in Physics*, vol. 35, no. 4, pp. 375–422, Jan. 1986. [Online]. Available: http://dx.doi.org/10.1080/00018738600101921 4.3, 4.4

[114] N. O. Birge, B. Golding, and W. H. Haemmerle, "Electron quantum interference and $1/f$ noise in bismuth," *Phys. Rev. Lett.*, vol. 62, no. 2, pp. 195–198, Jan. 1989. [Online]. Available: http://link.aps.org/doi/10.1103/PhysRevLett.62.195 4.3, 4.3

[115] ——, "Conductance fluctuations and $1/f$ noise in Bi," *Phys. Rev. B*, vol. 42, no. 5, pp. 2735–2743, Aug. 1990. [Online]. Available: http://link.aps.org/doi/10.1103/PhysRevB.42.2735 4.3, 4.3

[116] A. Trionfi, S. Lee, and D. Natelson, "Electronic coherence in metals: Comparing weak localization and time-dependent conductance fluctuations," *Phys. Rev. B*, vol. 70, no. 4, p. 041304, Jul. 2004. [Online]. Available: http://link.aps.org/doi/10.1103/PhysRevB.70.041304 4.3, 4.3

[117] ——, "Time-dependent universal conductance fluctuations in mesoscopic Au wires: Implications," *Phys. Rev. B*, vol. 75, no. 10, p. 104202, Mar. 2007.

[Online]. Available: http://link.aps.org/doi/10.1103/PhysRevB.75.104202 4.3, 4.3

[118] C. Barone, F. Romeo, S. Pagano, E. Di Gennaro, F. Miletto Granozio, I. Pallecchi, D. Marr, and U. Scotti di Uccio, "Carrier-number fluctuations in the 2-dimensional electron gas at the $LaAlO_3/SrTiO_3$ interface," *Applied Physics Letters*, vol. 103, no. 23, p. 231601, 2013. [Online]. Available: http://scitation.aip.org/content/aip/journal/apl/103/23/10.1063/1.4838637 4.3

[119] A. Trionfi, S. Lee, and D. Natelson, "Time-dependent universal conductance fluctuations and coherence in AuPd and Ag," *Physical Review B*, vol. 72, no. 3, p. 035407, Jul. 2005. [Online]. Available: http://link.aps.org/doi/10.1103/PhysRevB.72.035407 4.3

[120] A. D. Stone, "Reduction of low-frequency noise in metals by a magnetic field: Observability of the transition between random-matrix ensembles," *Phys. Rev. B*, vol. 39, no. 15, pp. 10 736–10 743, May 1989. [Online]. Available: http://link.aps.org/doi/10.1103/PhysRevB.39.10736 4.3

[121] S. Stemmer, Private communication, 2016. 4.4

[122] J. Matthews, F. Battista, D. Sánchez, P. Samuelsson, and H. Linke, "Experimental verification of reciprocity relations in quantum thermoelectric transport," *Phys. Rev. B*, vol. 90, no. 16, p. 165428, Oct. 2014. [Online]. Available: http://link.aps.org/doi/10.1103/PhysRevB.90.165428 4.4

[123] A. V. Anisovich, B. L. Al'Tshuler, A. G. Aronov, and A. Y. Zyuzin, "Mesoscopic fluctuations of thermoelectric coefficients," *Soviet Journal of Experimental and Theoretical Physics Letters*, vol. 45, p. 295, 1987. 4.4

[124] D. Sánchez and L. Serra, "Thermoelectric transport of mesoscopic conductors coupled to voltage and thermal probes," *Phys. Rev. B*, vol. 84, no. 20, p. 201307, Nov. 2011. [Online]. Available: http://link.aps.org/doi/10.1103/PhysRevB.84.201307 4.4

[125] W. A. Phillips, "Two-level states in glasses," *Reports on Progress in Physics*, vol. 50, no. 12, p. 1657, 1987. [Online]. Available: http://stacks.iop.org/0034-4885/50/i=12/a=003 4.4

[126] K. S. Ralls and R. A. Buhrman, "Defect interactions and noise in metallic nanoconstrictions," *Phys. Rev. Lett.*, vol. 60, no. 23, pp. 2434–2437, Jun. 1988. [Online]. Available: http://link.aps.org/doi/10.1103/PhysRevLett.60.2434 4.4

[127] P. A. M. Holweg, J. Caro, A. H. Verbruggen, and S. Radelaar, "Ballistic electron transport and two-level resistance fluctuations in noble-metal nanobridges," *Phys. Rev. B*, vol. 45, no. 16, pp. 9311–9319, Apr. 1992. [Online]. Available: http://link.aps.org/doi/10.1103/PhysRevB.45.9311 4.4

[128] J. J. Brophy, "Seebeck effect fluctuations in germanium," *Phys. Rev.*, vol. 111, no. 4, pp. 1050–1052, Aug. 1958. [Online]. Available: http://link.aps.org/doi/10.1103/PhysRev.111.1050 4.4

[129] S. W. Stanwyck, P. Gallagher, J. R. Williams, and D. Goldhaber-Gordon, "Universal conductance fluctuations in electrolyte-gated $SrTiO_3$ nanostructures," *Applied Physics Letters*, vol. 103, no. 21, p. 213504, 2013. [Online]. Available: http://scitation.aip.org/content/aip/journal/apl/103/21/10.1063/1.4832555 4.4

[130] D. Stornaiuolo, S. Gariglio, N. J. G. Couto, A. Fte, A. D. Caviglia, G. Seyfarth, D. Jaccard, A. F. Morpurgo, and J.-M. Triscone, "In-plane electronic confinement in superconducting $LaAlO_3/SrTiO_3$ nanostructures," *Applied Physics Letters*, vol. 101, no. 22, p. 222601, 2012. [Online]. Available: http://scitation.aip.org/content/aip/journal/apl/101/22/10.1063/1.4768936 4.4

[131] J.-W. Chang, J. Song, J. S. Lee, H. Noh, S. K. Seung, L. Baasandorj, S. G. Lee, Y.-J. Doh, and J. Kim, "Quantum electrical transport in mesoscopic $LaAlO_3$ /$SrTiO_3$ heterostructures," *Applied Physics Express*, vol. 6, no. 8, p. 085201, 2013. [Online]. Available: http://stacks.iop.org/1882-0786/6/i=8/a=085201 4.4

[132] D. Rakhmilevitch, M. Ben Shalom, M. Eshkol, A. Tsukernik, A. Palevski, and Y. Dagan, "Phase coherent transport in $SrTiO_3/LaAlO_3$ interfaces," *Physical Review B*, vol. 82, no. 23, p. 235119, Dec. 2010. [Online]. Available: http://link.aps.org/doi/10.1103/PhysRevB.82.235119 4.4

[133] S. A. Wolf, D. D. Awschalom, R. A. Buhrman, J. M. Daughton, S. von Molnár, M. L. Roukes, A. Y. Chtchelkanova, and D. M. Treger, "Spintronics: A spin-based electronics vision for the future," *Science*, vol. 294, no. 5546, pp. 1488–1495, 2001. [Online]. Available: http://www.sciencemag.org/content/294/5546/1488.abstract 5.1

[134] I. *Žutić*, J. Fabian, and S. Das Sarma, "Spintronics: Fundamentals and applications," *Rev. Mod. Phys.*, vol. 76, no. 2, pp. 323–410, Apr. 2004. [Online]. Available: http://link.aps.org/doi/10.1103/RevModPhys.76.323 5.1

[135] D. D. Awschalom and M. E. Flatte, "Challenges for semiconductor spintronics," *Nat. Phys.*, vol. 3, pp. 153–159, mARCH 2007. [Online]. Available: http://dx.doi.org/10.1038/nphys551 5.1

[136] C. Chappert, A. Fert, and F. N. Van Dau, "The emergence of spin electronics in data storage," *Nat. Mater.*, vol. 6, pp. 813–823, Apr 2007. [Online]. Available: http://dx.doi.org/10.1038/nmat2024 5.1

[137] S. Bader and S. Parkin, “Spintronics,” *Annual Review of Condensed Matter Physics*, vol. 1, no. 1, pp. 71–88, 2010. [Online]. Available: http://www.annualreviews.org/doi/abs/10.1146/annurev-conmatphys-070909-104123 5.1

[138] M. N. Baibich, J. M. Broto, A. Fert, F. N. Van Dau, F. Petroff, P. Etienne, G. Creuzet, A. Friederich, and J. Chazelas, “Giant magnetoresistance of (001)Fe/(001)Cr magnetic superlattices,” *Phys. Rev. Lett.*, vol. 61, pp. 2472–2475, Nov 1988. [Online]. Available: http://link.aps.org/doi/10.1103/PhysRevLett.61.2472 5.1, 5.3

[139] G. Binasch, P. Grünberg, F. Saurenbach, and W. Zinn, “Enhanced magnetoresistance in layered magnetic structures with antiferromagnetic interlayer exchange,” *Phys. Rev. B*, vol. 39, pp. 4828–4830, Mar 1989. [Online]. Available: http://link.aps.org/doi/10.1103/PhysRevB.39.4828 5.1, 5.3

[140] T. Miyazaki and N. Tezuka, “Giant magnetic tunneling effect in Fe/Al_2O_3/Fe junction,” *Journal of Magnetism and Magnetic Materials*, vol. 139, no. 3, pp. L231–L234, 1995. 5.1

[141] J. S. Moodera, L. R. Kinder, T. M. Wong, and R. Meservey, “Large magnetoresistance at room temperature in ferromagnetic thin film tunnel junctions,” *Physical Review Letters*, vol. 74, no. 16, p. 3273, 1995. 5.1

[142] S. Jin, T. H. Tiefel, M. McCormack, R. A. Fastnacht, R. Ramesh, and L. H. Chen, “Thousandfold change in resistivity in magnetoresistive La-Ca-Mn-O films,” *Science*, vol. 264, no. 5157, pp. 413–415, 1994. [Online]. Available: http://www.sciencemag.org/content/264/5157/413.abstract 5.1

[143] C. Gould, C. Rüster, T. Jungwirth, E. Girgis, G. M. Schott, R. Giraud, K. Brunner, G. Schmidt, and L. W. Molenkamp, “Tunneling anisotropic magnetoresistance: A spin-valve-like tunnel magnetoresistance using a single magnetic layer,” *Phys. Rev. Lett.*, vol. 93, p. 117203, Sep 2004. [Online]. Available: http://link.aps.org/doi/10.1103/PhysRevLett.93.117203 5.1

[144] H. Saito, S. Yuasa, and K. Ando, “Origin of the tunnel anisotropic magnetoresistance in $Ga_{1-x}Mn_xAs$/ZnSe/$Ga_{1-x}Mn_xAs$ magnetic tunnel junctions of II-VI/III-V heterostructures,” *Phys. Rev. Lett.*, vol. 95, p. 086604, Aug 2005. [Online]. Available: http://link.aps.org/doi/10.1103/PhysRevLett.95.086604 5.1

[145] H. Toyosaki, T. Fukumura, Y. Yamada, K. Nakajima, T. Chikyow, T. Hasegawa, H. Koinuma, and M. Kawasaki, “Anomalous hall effect governed by electron doping in a room-temperature transparent ferromagnetic semiconductor,” *Nat. Mater.*, vol. 3, pp. 221–224, Apr 2004. [Online]. Available: http://dx.doi.org/10.1038/nmat1099 5.1

[146] R. Kusters, J. Singleton, D. Keen, R. McGreevy, and W. Hayes, "Magnetoresistance measurements on the magnetic semiconductor $Nd_{0.5}Pb_{0.5}MnO_3$," *Physica B: Condensed Matter*, vol. 155, pp. 362 – 365, 1989. [Online]. Available: http://www.sciencedirect.com/science/article/pii/0921452689905309 5.1

[147] Y. Tokura and Y. Tomioka, "Colossal magnetoresistive manganites," *Journal of Magnetism and Magnetic Materials*, vol. 200, pp. 1 – 23, 1999. [Online]. Available: http://www.sciencedirect.com/science/article/pii/S0304885399003522 5.1

[148] M. Uehara, S. Mori, C. H. Chen, and S.-W. Cheong, "Percolative phase separation underlies colossal magnetoresistance in mixed-valent manganites," *Nature*, vol. 399, pp. 560–563, June 1999. [Online]. Available: http://dx.doi.org/10.1038/21142 5.1

[149] E. Dagotto, T. Hotta, and A. Moreo, "Colossal magnetoresistant materials: the key role of phase separation," *Physics Reports*, vol. 344, pp. 1 – 153, 2001. [Online]. Available: http://www.sciencedirect.com/science/article/pii/S0370157300001216 5.1

[150] V. Sechovský, L. Havela, K. Prokeš̃, H. Nakotte, F. R. de Boer, and E. Brück, "Giant magnetoresistance effects in intermetallic compounds (invited)," *Journal of Applied Physics*, vol. 76, no. 10, pp. 6913–6918, 1994. [Online]. Available: http://scitation.aip.org/content/aip/journal/jap/76/10/10.1063/1.358114 5.1

[151] Y. Janssen, H. Fujii, T. Ekino, K. Izawa, T. Suzuki, T. Fujita, and F. R. de Boer, "Giant magnetoresistance in Ce_2Fe_{17}," *Phys. Rev. B*, vol. 56, pp. 13 716–13 719, Dec 1997. [Online]. Available: http://link.aps.org/doi/10.1103/PhysRevB.56.13716 5.1

[152] H. Y. Hwang, S.-W. Cheong, P. G. Radaelli, M. Marezio, and B. Batlogg, "Lattice effects on the magnetoresistance in doped $LaMnO_3$," *Phys. Rev. Lett.*, vol. 75, pp. 914–917, Jul 1995. [Online]. Available: http://link.aps.org/doi/10.1103/PhysRevLett.75.914 5.1

[153] A. J. Millis, R. Mueller, and B. I. Shraiman, "Fermi-liquid-to-polaron crossover. II. Double exchange and the physics of colossal magnetoresistance," *Phys. Rev. B*, vol. 54, pp. 5405–5417, Aug 1996. [Online]. Available: http://link.aps.org/doi/10.1103/PhysRevB.54.5405 5.1

[154] D. Hammer, J. Wu, and C. Leighton, "Metal-insulator transition, giant negative magnetoresistance, and ferromagnetism in $LaCo_{1-y}Ni_yO_3$," *Phys. Rev. B*, vol. 69, p. 134407, Apr 2004. [Online]. Available: http://link.aps.org/doi/10.1103/PhysRevB.69.134407 5.1

[155] F. Nakamura, R. Nakai, T. Takemoto, M. Sakaki, T. Suzuki, P. L. Alireza, S. Nakatsuji, and Y. Maeno, "Anisotropic giant magnetoresistance near the

mott transition in pressurized Ca_2RuO_4," *Phys. Rev. B*, vol. 80, p. 193103, Nov 2009. [Online]. Available: http://link.aps.org/doi/10.1103/PhysRevB.80.193103 5.1

[156] J. Wilson and A. Yoffe, "The transition metal dichalcogenides discussion and interpretation of the observed optical, electrical and structural properties," *Advances in Physics*, vol. 18, no. 73, pp. 193–335, 1969. [Online]. Available: http://dx.doi.org/10.1080/00018736900101307 5.1

[157] J. Wilson, F. Di Salvo, and S. Mahajan, "Charge-density waves and superlattices in the metallic layered transition metal dichalcogenides," *Advances in Physics*, vol. 24, no. 2, pp. 117–201, 1975. [Online]. Available: http://dx.doi.org/10.1080/00018737500101391 5.1

[158] S. S. Parkin and R. H. Friend, "3*d* transition-metal intercalates of the niobium and tantalum dichalcogenides I Magnetic properties," *Philos. Mag. B*, vol. 41, p. 65, 1980. 5.1

[159] ——, "3*d* transition-metal intercalates of the niobium and tantalum dichalcogenides II Transport properties," *Philos. Mag. B*, vol. 41, p. 95, 1980. 5.1

[160] M. Eibschütz, F. J. DiSalvo, G. W. Hull, and S. Mahajan, "Ferromagnetism in metallic Fe_xTaS_2 ($x \approx .28$)," *Applied Physics Letters*, vol. 27, no. 8, pp. 464–466, 1975. [Online]. Available: http://scitation.aip.org/content/aip/journal/apl/27/8/10.1063/1.88529 5.1, 5.3

[161] M. Eibschütz, S. Mahajan, F. J. DiSalvo, G. W. Hull, and J. V. Waszczak, "Ferromagnetism in metallic intercalated compounds Fe_xTaS_2 ($0.20 < x < 0.34$)," *Journal of Applied Physics*, vol. 52, no. 3, pp. 2098–2100, 1981. [Online]. Available: http://scitation.aip.org/content/aip/journal/jap/52/3/10.1063/1.329629 5.1, 5.2, 5.3

[162] J. Dijkstra, P. J. Zijlema, C. F. van Bruggen, C. Haas, and R. A. de Groot, "Band-structure calculations of $Fe_{1/3}TaS_2$ and $Mn_{1/3}TaS_2$, and transport and magnetic properties of $Fe_{0.28}TaS_2$," *Journal of Physics: Condensed Matter*, vol. 1, no. 36, p. 6363, 1989. [Online]. Available: http://stacks.iop.org/0953-8984/1/i=36/a=005 5.1, 5.3, 5.3

[163] H. Narita, H. Ikuta, H. Hinode, T. Uchida, T. Ohtani, and M. Wakihara, "Preparation and physical properties of Fe_xTaS_2 ($0.15 \leq x \leq 0.50$) compounds," *Journal of Solid State Chemistry*, vol. 108, no. 1, pp. 148 – 151, 1994. [Online]. Available: http://www.sciencedirect.com/science/article/pii/S002245968471022X 5.1, 5.3

[164] J. G. Checkelsky, M. Lee, E. Morosan, R. J. Cava, and N. P. Ong, "Anomalous Hall effect and magnetoresistance in the layered ferromagnet $Fe_{1/4}TaS_2$: The

inelastic regime," *Phys. Rev. B*, vol. 77, p. 014433, Jan 2008. [Online]. Available: http://link.aps.org/doi/10.1103/PhysRevB.77.014433 5.1, 5.3

[165] X. Xu, W. Yao, D. Xiao, and T. F. Heinz, "Spin and pseudospins in layered transition metal dichalcogenides," *Nat. Phys.*, vol. 10, pp. 343–350, May 2014. [Online]. Available: http://dx.doi.org/10.1038/nphys2942 5.1

[166] T. McGuire and R. Potter, "Anisotropic magnetoresistance in ferromagnetic 3d alloys," *Magnetics, IEEE Transactions on*, vol. 11, no. 4, pp. 1018–1038, Jul 1975. 5.3

[167] F. Matsukura, H. Ohno, A. Shen, and Y. Sugawara, "Transport properties and origin of ferromagnetism in (Ga,Mn)As," *Phys. Rev. B*, vol. 57, pp. R2037–R2040, Jan 1998. [Online]. Available: http://link.aps.org/doi/10.1103/PhysRevB.57.R2037 5.3

[168] N. Nagaosa, J. Sinova, S. Onoda, A. H. MacDonald, and N. P. Ong, "Anomalous Hall effect," *Rev. Mod. Phys.*, vol. 82, pp. 1539–1592, May 2010. [Online]. Available: http://link.aps.org/doi/10.1103/RevModPhys.82.1539 5.3

[169] J. Q. Xiao, J. S. Jiang, and C. L. Chien, "Giant magnetoresistance in nonmultilayer magnetic systems," *Phys. Rev. Lett.*, vol. 68, pp. 3749–3752, Jun 1992. [Online]. Available: http://link.aps.org/doi/10.1103/PhysRevLett.68.3749 5.3

[170] M. D. Vannette, S. Yeninas, E. Morosan, R. J. Cava, and R. Prozorov, "Local-moment ferromagnetism and unusual magnetic domains in $Fe_{1/4}TaS_2$ crystals," *Phys. Rev. B*, vol. 80, p. 024421, Jul 2009. [Online]. Available: http://link.aps.org/doi/10.1103/PhysRevB.80.024421 5.3

[171] C. Haas, "Spin-disorder scattering and magnetoresistance of magnetic semiconductors," *Phys. Rev.*, vol. 168, pp. 531–538, Apr 1968. [Online]. Available: http://link.aps.org/doi/10.1103/PhysRev.168.531 5.3

[172] M. J. Otto, R. A. M. van Woerden, P. J. van der Valk, J. Wijngaard, C. F. van Bruggen, and C. Haas, "Half-metallic ferromagnets. II. Transport properties of NiMnSb and related inter-metallic compounds," *Journal of Physics: Condensed Matter*, vol. 1, no. 13, p. 2351, 1989. [Online]. Available: http://stacks.iop.org/0953-8984/1/i=13/a=008 5.3

[173] Y. Horibe, J. Yang, Y.-H. Cho, X. Luo, S. B. Kim, Y. S. Oh, F.-T. Huang, T. Asada, M. Tanimura, D. Jeong, and S.-W. Cheong, "Color theorems, chiral domain topology, and magnetic properties of Fe_xTaS_2," *Journal of the American Chemical Society*, vol. 136, no. 23, pp. 8368–8373, 2014. [Online]. Available: http://pubs.acs.org/doi/abs/10.1021/ja5026134 5.3

[174] K.-T. Ko, K. Kim, S. B. Kim, H.-D. Kim, J.-Y. Kim, B. I. Min, J.-H. Park, F.-H. Chang, H.-J. Lin, A. Tanaka, and S.-W. Cheong, "RKKY ferromagnetism with Ising-like spin states in intercalated $Fe_{1/4}TaS_2$," *Physical Review Letters*, vol. 107, no. 24, p. 247201, 2011. 5.3

[175] C.-W. Chen, "Correlations between magneto-transport properties and crystal structure in transition metal pnictides and chalcogenides," Ph.D. dissertation, Rice University, 2016. 5.3, 7.1

[176] K. S. Novoselov, D. Jiang, F. Schedin, T. J. Booth, V. V. Khotkevich, S. V. Morozov, and A. K. Geim, "Two-dimensional atomic crystals," *Proceedings of the National Academy of Sciences*, vol. 102, no. 30, pp. 10 451–10 453, Jul. 2005. [Online]. Available: http://www.pnas.org/cgi/doi/10.1073/pnas.0502848102 6.1

[177] Q. H. Wang, K. Kalantar-Zadeh, A. Kis, J. N. Coleman, and M. S. Strano, "Electronics and optoelectronics of two-dimensional transition metal dichalcogenides," *Nature Nanotechnology*, vol. 7, no. 11, pp. 699–712, Nov. 2012. [Online]. Available: http://www.nature.com/nnano/journal/v7/n11/full/nnano.2012.193.html 6.1

[178] S. Z. Butler, S. M. Hollen, L. Cao, Y. Cui, J. A. Gupta, H. R. Gutirrez, T. F. Heinz, S. S. Hong, J. Huang, A. F. Ismach, E. Johnston-Halperin, M. Kuno, V. V. Plashnitsa, R. D. Robinson, R. S. Ruoff, S. Salahuddin, J. Shan, L. Shi, M. G. Spencer, M. Terrones, W. Windl, and J. E. Goldberger, "Progress, challenges, and opportunities in two-dimensional materials beyond graphene," *ACS Nano*, vol. 7, no. 4, pp. 2898–2926, Apr. 2013. [Online]. Available: http://dx.doi.org/10.1021/nn400280c 6.1

[179] G. R. Bhimanapati, Z. Lin, V. Meunier, Y. Jung, J. Cha, S. Das, D. Xiao, Y. Son, M. S. Strano, V. R. Cooper, L. Liang, S. G. Louie, E. Ringe, W. Zhou, S. S. Kim, R. R. Naik, B. G. Sumpter, H. Terrones, F. Xia, Y. Wang, J. Zhu, D. Akinwande, N. Alem, J. A. Schuller, R. E. Schaak, M. Terrones, and J. A. Robinson, "Recent advances in two-dimensional materials beyond graphene," *ACS Nano*, vol. 9, no. 12, pp. 11 509–11 539, Dec. 2015. [Online]. Available: http://dx.doi.org/10.1021/acsnano.5b05556 6.1

[180] H. Chen, Q. Niu, Z. Zhang, and A. H. MacDonald, "Gate-tunable exchange coupling between cobalt clusters on graphene," *Physical Review B*, vol. 87, no. 14, p. 144410, Apr. 2013. [Online]. Available: http://link.aps.org/doi/10.1103/PhysRevB.87.144410 6.1

[181] K. Zhang, S. Feng, J. Wang, A. Azcatl, N. Lu, R. Addou, N. Wang, C. Zhou, J. Lerach, V. Bojan, M. J. Kim, L.-Q. Chen, R. M. Wallace, M. Terrones, J. Zhu, and J. A. Robinson, "Manganese doping of monolayer MoS_2: The

substrate is critical," *Nano Letters*, vol. 15, no. 10, pp. 6586–6591, Oct. 2015. [Online]. Available: http://dx.doi.org/10.1021/acs.nanolett.5b02315 6.1

[182] T. Cao, Z. Li, and S. G. Louie, "Tunable magnetism and half-metallicity in hole-doped monolayer gase," *Physical Review Letters*, vol. 114, no. 23, p. 236602, Jun. 2015. [Online]. Available: http://link.aps.org/doi/10.1103/PhysRevLett.114.236602 6.1

[183] S. Wu, X. Dai, H. Yu, H. Fan, J. Hu, and W. Yao, "Magnetisms in *p*-type monolayer gallium chalcogenides (GaSe, GaS)," *arXiv:1409.4733 [cond-mat]*, Sep. 2014. [Online]. Available: http://arxiv.org/abs/1409.4733 6.1

[184] L. D. Casto, A. J. Clune, M. O. Yokosuk, J. L. Musfeldt, T. J. Williams, H. L. Zhuang, M.-W. Lin, K. Xiao, R. G. Hennig, B. C. Sales, J.-Q. Yan, and D. Mandrus, "Strong spin-lattice coupling in $CrSiTe_3$," *APL Materials*, vol. 3, no. 4, p. 041515, Apr. 2015. [Online]. Available: http://scitation.aip.org/content/aip/journal/aplmater/3/4/10.1063/1.4914134 6.1

[185] T. J. Williams, A. A. Aczel, M. D. Lumsden, S. E. Nagler, M. B. Stone, J.-Q. Yan, and D. Mandrus, "Magnetic correlations in the quasi-two-dimensional semiconducting ferromagnet $CrSiTe_3$," *Physical Review B*, vol. 92, no. 14, p. 144404, Oct. 2015. [Online]. Available: http://link.aps.org/doi/10.1103/PhysRevB.92.144404 6.1

[186] H. Nozaki, Y. Ishizawa, M. Saeki, and M. Nakahira, "Electrical properties of V_5S_8 single crystals," *Physics Letters A*, vol. 54, no. 1, pp. 29–30, 1975. [Online]. Available: http://www.sciencedirect.com/science/article/pii/0375960175905939 6.1, 6.3

[187] A. B. D. Vries and C. Haas, "Magnetic susceptibility and nuclear magnetic resonance of vanadium sulfides," *Journal of Physics and Chemistry of Solids*, vol. 34, no. 4, pp. 651–659, 1973. [Online]. Available: http://www.sciencedirect.com/science/article/pii/S0022369773801714 6.1

[188] Y. Oka, K. Kosuge, and S. Kachi, "Magnetic properties of V_5S_8," *Physics Letters A*, vol. 50, no. 4, pp. 311–312, 1974. [Online]. Available: http://www.sciencedirect.com/science/article/pii/037596017490766X 6.1

[189] A. Fujimori, M. Saeki, and H. Nozaki, "Electron correlation, ¡i¿d¡/i¿ -band formation, and magnetism in V_5S_8: Photoemission-spectroscopy study," *Phys. Rev. B*, vol. 44, no. 1, pp. 163–169, Jul. 1991. [Online]. Available: http://link.aps.org/doi/10.1103/PhysRevB.44.163 6.1

[190] Y. Kitaoka and H. Yasuoka, "NMR investigations on the spin fluctuations in itinerant antiferromagnets. ii. V_3S_4 and V_5S_8," *Journal of the Physical Society of Japan*, vol. 48, no. 6, pp. 1949–1956, 1980. [Online]. Available: http://dx.doi.org/10.1143/JPSJ.48.1949 6.1

[191] H. Nishihara, H. Yasuoka, Y. Oka, K. Kosuge, and S. Kachi, "NMR of ^{51}V in the antiferromagnetic state of V_5S_8," *Journal of the Physical Society of Japan*, vol. 42, no. 3, pp. 787–790, 1977. [Online]. Available: http://dx.doi.org/10.1143/JPSJ.42.787 6.1

[192] S. Funahashi, H. Nozaki, and I. Kawada, "Magnetic structure of V_5S_8," *Journal of Physics and Chemistry of Solids*, vol. 42, no. 11, pp. 1009–1013, 1981. [Online]. Available: http://www.sciencedirect.com/science/article/pii/0022369781900640 6.1, 6.3

[193] J. B. Forsyth, P. J. Brown, I. Kawada, H. Nozaki, and M. Saeki, "Contributions to the magnetisation in paramagnetic V_5S_8," *Journal of Physics C: Solid State Physics*, vol. 12, no. 20, p. 4261, 1979. [Online]. Available: http://stacks.iop.org/0022-3719/12/i=20/a=020 6.1

[194] H. Nozaki, M. Umehara, Y. Ishizawa, M. Saeki, T. Mizoguchi, and M. Nakahira, "Magnetic properties of V_5S_8 single crystals," *Journal of Physics and Chemistry of Solids*, vol. 39, no. 8, pp. 851–858, Jan. 1978. [Online]. Available: http://www.sciencedirect.com/science/article/pii/0022369778901440 6.1

[195] H. Nozaki and Y. Ishizawa, "An evidence of spin flopping in V_5S_8 by magnetoresistance experiments," *Physics Letters A*, vol. 63, no. 2, pp. 131–132, Oct. 1977. [Online]. Available: http://www.sciencedirect.com/science/article/pii/0375960177902249 6.1

[196] M. Knecht, H. Ebert, and W. Bensch, "Electronic and magnetic properties of V_5S_8," *Journal of Physics: Condensed Matter*, vol. 10, no. 42, p. 9455, 1998. [Online]. Available: http://stacks.iop.org/0953-8984/10/i=42/a=011 6.1, 6.3

[197] K. Usami, "Magnetoresistance in antiferromagnetic metals," *Journal of the Physical Society of Japan*, vol. 45, no. 2, pp. 466–475, Aug. 1978. [Online]. Available: http://journals.jps.jp/doi/abs/10.1143/JPSJ.45.466 6.3

[198] H. Kuwahara, Y. Tomioka, A. Asamitsu, Y. Moritomo, and Y. Tokura, "A first-order phase transition induced by a magnetic field," *Science*, vol. 270, no. 5238, pp. 961–963, 1995. [Online]. Available: http://www.jstor.org/stable/2888104 6.3

[199] W. J. Hu, J. Du, B. Li, Q. Zhang, and Z. D. Zhang, "Giant magnetocaloric effect in the ising antiferromagnet DySb," *Applied Physics Letters*, vol. 92, no. 19, 2008. [Online]. Available: http://scitation.aip.org/content/aip/journal/apl/92/19/10.1063/1.2928233 6.3

[200] J. Chen, B. G. Shen, Q. Y. Dong, and J. R. Sun, "Giant magnetic entropy change in antiferromagnetic DyCuSi compound," *Solid State Communications*, vol. 150, no. 31-32, pp. 1429–1431, 2010. [Online]. Available: http://www.sciencedirect.com/science/article/pii/S0038109810002887 6.3

[201] J. Chen, B. G. Shen, Q. Y. Dong, F. X. Hu, and J. R. Sun, “Giant reversible magnetocaloric effect in metamagnetic HoCuSi compound,” *Applied Physics Letters*, vol. 96, no. 15, 2010. [Online]. Available: http://scitation.aip.org/content/aip/journal/apl/96/15/10.1063/1.3386536 6.3

[202] L. Balicas, S. Nakatsuji, H. Lee, P. Schlottmann, T. P. Murphy, and Z. Fisk, “Magnetic field-tuned quantum critical point in $\mathrm{CeAuSb_2}$,” *Phys. Rev. B*, vol. 72, no. 6, p. 064422, Aug. 2005. [Online]. Available: http://link.aps.org/doi/10.1103/PhysRevB.72.064422 6.3

[203] M. Charilaou and F. Hellman, “Roughness effects in uncompensated antiferromagnets,” *Journal of Applied Physics*, vol. 117, no. 8, p. 083907, 2015. [Online]. Available: http://scitation.aip.org/content/aip/journal/jap/117/8/10.1063/1.4913594 6.3

[204] X. Jehl, M. Sanquer, R. Calemczuk, and D. Mailly, “Detection of doubled shot noise in short normal-metal/ superconductor junctions,” *Nature*, vol. 405, no. 6782, pp. 50–53, May 2000. [Online]. Available: http://dx.doi.org/10.1038/35011012 7.1

[205] P. J. Wheeler, R. Chen, and D. Natelson, “Noise in electromigrated nanojunctions,” *Phys. Rev. B*, vol. 87, p. 155411, Apr 2013. [Online]. Available: http://link.aps.org/doi/10.1103/PhysRevB.87.155411 7.1

[206] R. Chen, P. J. Wheeler, and D. Natelson, “Excess noise in stm-style break junctions at room temperature,” *Phys. Rev. B*, vol. 85, p. 235455, Jun 2012. [Online]. Available: http://link.aps.org/doi/10.1103/PhysRevB.85.235455 7.1

[207] R. Chen, M. Matt, F. Pauly, P. Nielaba, J. C. Cuevas, and D. Natelson, “Shot noise variation within ensembles of gold atomic break junctions at room temperature,” *Journal of Physics: Condensed Matter*, vol. 26, no. 47, p. 474204, 2014. [Online]. Available: http://stacks.iop.org/0953-8984/26/i=47/a=474204 7.1

[208] R. Chen, P. J. Wheeler, M. Di Ventra, and D. Natelson, “Enhanced noise at high bias in atomic-scale au break junctions,” *Scientific Reports*, vol. 4, p. 4221, Feb. 2014. [Online]. Available: http://dx.doi.org/10.1038/srep04221 7.1

[209] L. A. Stevens, P. Zolotavin, R. Chen, and D. Natelson, “Current noise enhancement: channel mixing and possible nonequilibrium phonon backaction in atomic-scale au junctions,” *Journal of Physics: Condensed Matter*, vol. 28, no. 49, p. 495303, 2016. [Online]. Available: http://stacks.iop.org/0953-8984/28/i=49/a=495303 7.1

[210] P. J. Wheeler, J. N. Russom, K. Evans, N. S. King, and D. Natelson, “Shot noise suppression at room temperature in atomic-scale au junctions,”

Nano Letters, vol. 10, no. 4, pp. 1287–1292, Apr. 2010. [Online]. Available: http://dx.doi.org/10.1021/nl904052r 7.1

[211] P. Zhou, W. J. Hardy, K. Watanabe, T. Taniguchi, and D. Natelson, "Shot noise detection in hBN-based tunnel junctions," *Appl. Phys. Lett.*, vol. 110, no. 13, p. 133106, Mar. 2017. [Online]. Available: http://dx.doi.org/10.1063/1.4978693 7.1

[212] F. J. Di Salvo, D. E. Moncton, and J. V. Waszczak, "Electronic properties and superlattice formation in the semimetal $TiSe_2$," *Phys. Rev. B*, vol. 14, no. 10, pp. 4321–4328, Nov. 1976. [Online]. Available: http://link.aps.org/doi/10.1103/PhysRevB.14.4321 8.1

[213] T. E. Kidd, T. Miller, M. Y. Chou, and T.-C. Chiang, "Electron-hole coupling and the charge density wave transition in $TiSe_2$," *Phys. Rev. Lett.*, vol. 88, no. 22, p. 226402, May 2002. [Online]. Available: http://link.aps.org/doi/10.1103/PhysRevLett.88.226402 8.1

[214] S. Y. Li, G. Wu, X. H. Chen, and L. Taillefer, "Single-gap s-wave superconductivity near the charge-density-wave quantum critical point in Cu_xTiSe_2," *Phys. Rev. Lett.*, vol. 99, no. 10, p. 107001, Sep. 2007. [Online]. Available: http://link.aps.org/doi/10.1103/PhysRevLett.99.107001 8.1

[215] E. Morosan, K. E. Wagner, L. L. Zhao, Y. Hor, A. J. Williams, J. Tao, Y. Zhu, and R. J. Cava, "Multiple electronic transitions and superconductivity in Pd_xTiSe_2," *Phys. Rev. B*, vol. 81, no. 9, p. 094524, Mar. 2010. [Online]. Available: http://link.aps.org/doi/10.1103/PhysRevB.81.094524 8.1

[216] E. Morosan, H. W. Zandbergen, B. S. Dennis, J. W. G. Bos, Y. Onose, T. Klimczuk, A. P. Ramirez, N. P. Ong, and R. J. Cava, "Superconductivity in Cu_xTiSe_2," *Nat Phys*, vol. 2, no. 8, pp. 544–550, Aug. 2006. [Online]. Available: http://dx.doi.org/10.1038/nphys360 8.1, 8.3

[217] G. Li, W. Z. Hu, D. Qian, D. Hsieh, M. Z. Hasan, E. Morosan, R. J. Cava, and N. L. Wang, "Semimetal-to-semimetal charge density wave transition in $1T$-$TiSe_2$," *Phys. Rev. Lett.*, vol. 99, no. 2, p. 027404, Jul. 2007. [Online]. Available: http://link.aps.org/doi/10.1103/PhysRevLett.99.027404 8.1

[218] T. Takabatake, W. Ye, S. Orimo, T. Tamegai, and H. Fujii, "Hydrogen intercalation in some superconducting copper oxides," vol. 162, pp. 65–66, Dec. 1989. [Online]. Available: http://www.sciencedirect.com/science/article/pii/0921453489909192 8.1

[219] A. M. Chippindale, P. G. Dickens, and A. V. Powell, "Insertion compounds of transition-metal and uranium oxides," vol. 21, no. 3, pp. 133–198, Jan. 1991. [Online]. Available: http://www.sciencedirect.com/science/article/pii/007967869190003I 8.2